

AD-A163 835

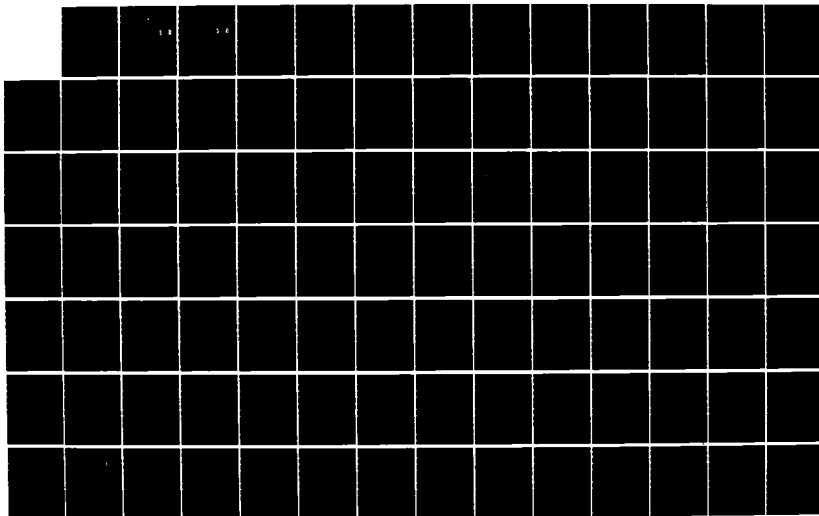
STATISTICAL ANALYSIS OF LOW ENERGY ELECTRONS AND THEIR
RELATIONSHIP TO RA. (U) AIR FORCE INST OF TECH
WRIGHT-PATTERSON AFB OH SCHOOL OF ENGI. . W E OBER
DEC 84 AFIT/GSO/ENP-ENS/84D-3

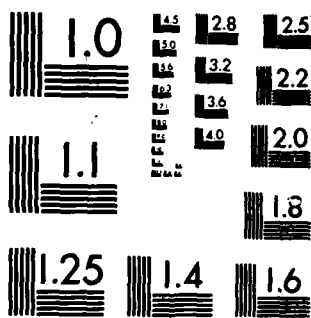
1/2

UNCLASSIFIED

F/G 4/1

NL





MICROCOPY RESOLUTION TEST CHART
NATIONAL BUREAU OF STANDARDS-1963-A

AD-A163 835



DTIC
ELECTE
FEB 10 1988
S D

STATISTICAL ANALYSIS OF LOW ENERGY
ELECTRONS AND THEIR RELATIONSHIP
TO RADIOWAVE SCINTILLATIONS

THESIS

William E. Ober
Captain, USAF

AFIT/GSO/ENP-ENS/84D-3

DISTRIBUTION STATEMENT A

Approved for public release;
Distribution Unlimited

DEPARTMENT OF THE AIR FORCE

AIR UNIVERSITY

AIR FORCE INSTITUTE OF TECHNOLOGY

Wright-Patterson Air Force Base, Ohio

86 2 10 007

FILE COPY

AFIT/GSO/ENP-ENS/84

1

DTIC
ELECTE
FEB 10 1986
S D D

STATISTICAL ANALYSIS OF LOW ENERGY
ELECTRONS AND THEIR RELATIONSHIP
TO RADIOWAVE SCINTILLATIONS

THESIS

William E. Ober
Captain, USAF

AFIT/GSO/ENP-ENS/84D-3

Approved for public release; distribution unlimited

UNCLASSIFIED
SECURITY CLASSIFICATION OF THIS PAGE

AD-A163 835-

REPORT DOCUMENTATION PAGE

1a. REPORT SECURITY CLASSIFICATION UNCLASSIFIED			1b. RESTRICTIVE MARKINGS		
2a. SECURITY CLASSIFICATION AUTHORITY			3. DISTRIBUTION/AVAILABILITY OF REPORT Approved for public release, distribution unlimited		
2b. DECLASSIFICATION/DOWNGRADING SCHEDULE					
4. PERFORMING ORGANIZATION REPORT NUMBER(S) AFIT/GSO/ENP-ENS/84D-3			5. MONITORING ORGANIZATION REPORT NUMBER(S)		
6a. NAME OF PERFORMING ORGANIZATION School of Engineering		6b. OFFICE SYMBOL (If applicable) AFIT/ENA	7a. NAME OF MONITORING ORGANIZATION		
6c. ADDRESS (City, State and ZIP Code) Air Force Institute of Technology Wright-Patterson AFB, OH 45433			7b. ADDRESS (City, State and ZIP Code)		
8a. NAME OF FUNDING/SPONSORING ORGANIZATION Space Physics Division		8b. OFFICE SYMBOL (If applicable) PHP	9. PROCUREMENT INSTRUMENT IDENTIFICATION NUMBER		
8c. ADDRESS (City, State and ZIP Code) Air Force Geophysics Laboratory Hanscom AFB, MA 01731			10. SOURCE OF FUNDING NOS.		
			PROGRAM ELEMENT NO.	PROJECT NO.	TASK NO.
11. TITLE (Include Security Classification) See Box 19					
12. PERSONAL AUTHOR(S) William E. Ober, B.S., Capt, USAF					
13a. TYPE OF REPORT MS Thesis		13b. TIME COVERED FROM _____ TO _____		14. DATE OF REPORT (Yr., Mo., Day) 1984 December	
				15. PAGE COUNT 162	
16. SUPPLEMENTARY NOTATION					
17. COSATI CODES			18. SUBJECT TERMS (Continue on reverse if necessary and identify by block number)		
FIELD	GROUP	SUB. GR.	STATISTICAL ANALYSIS, IONOSPHERE, HILAT IONOSPHERIC PROPAGATION		
20	14				
4	1				
19. ABSTRACT (Continue on reverse if necessary and identify by block number) Title: STATISTICAL ANALYSIS OF LOW ENERGY ELECTRONS AND THEIR RELATIONSHIP TO RADIOWAVE SCINTILLATIONS Thesis Committee: James Lange, Major, USAF Joseph Coleman, Lt Col, USAF <div style="text-align: right;"><i>Approved for public release</i> LAW AFB 1984 <i>Lyn E. Wolaver</i> 16 JAN 86 Dean for Research and Professional Development Air Force Institute of Technology (AFIT) Wright-Patterson AFB OH 45433</div>					
20. DISTRIBUTION/AVAILABILITY OF ABSTRACT UNCLASSIFIED/UNLIMITED <input checked="" type="checkbox"/> SAME AS RPT. <input type="checkbox"/> OTIC USERS <input type="checkbox"/>			21. ABSTRACT SECURITY CLASSIFICATION UNCLASSIFIED		
22a. NAME OF RESPONSIBLE INDIVIDUAL James Lange, Major, USAF			22b. TELEPHONE NUMBER (Include Area Code) (513) 255-2012		22c. OFFICE SYMBOL AFIT/ENP

The relationship between the observed increase in the flux of low energy (500 eV) electrons, at an altitude of 800 km and the corresponding amplitude and frequency scintillations of radio waves passing through ionospheric irregularities at 350 km was studied. This data was measured by the electron spectrometer (J-sensor), the magnetometer, and the radio beacon experiment (137 MHz and 413 MHz) of the HILAT satellite. The data analyzed here was taken from January-March 1984. During that time interval 198 enhancements of electron flux were recorded in the night sectors (magnetic local time), occurring most frequently at 0300 and 2300 MLT.

For 73 of these enhancements, magnetometer data was examined for corresponding geomagnetic disturbances, but only nine had such associated disturbances. The average increase in electron number flux for the 73 enhancements was found to be 9.7×10^8 electrons/cm²-sec-ster with a standard deviation of equivalent magnitude. Enhancements with number fluxes greater than 2×10^9 electrons/cm²-sec-ster were the same ones that had correspondingly large geomagnetic disturbances.

When the values of the phase scintillations for 137 MHz (known as PRMS) were plotted against those for 413 MHz, a linear curve that agreed with theory put forth by Briggs and Parkin resulted. The same was done with the amplitude scintillation data; the distribution was not as linear, but many points fell along linear curves for limiting large and small values of the traverse radii of irregularities as described by Briggs and Parkin.

For the 42 sets of values for PRMS and S4 used in the discriminant analysis, the increase in integrated number flux (PEAK) and the average electron energy (EAVG) were significant indicators in determining S4 at 137 MHz. The size of the enhancement, as indicated by the time necessary to traverse it (TIME) and the time difference between enhancement encounter and scintillation occurrence (DT) were good indicators for determining the rise of PRMS at both frequencies and the rise of PRMS at 413 MHz by itself.

TIME and DT were also indicative of scintillation increases (S4 and PRMS) at 413 MHz. Results for finding indicators for S4 at 413 MHz, and PRMS at 137 MHz were not statistically significant.

STATISTICAL ANALYSIS OF LOW ENERGY ELECTRONS AND
THEIR RELATIONSHIP TO RADIOWAVE SCINTILLATIONS

THESIS

Presented to the Faculty of the School of Engineering
of the Air Force Institute of Technology

Air University

In Partial Fulfillment of the
Requirements for the Degree of
Master of Science in Space Operations

William E. Ober, B.S.
Captain, USAF

December 1984

Accession For	
NTIS CRA&I	<input checked="checked" type="checkbox"/>
DTIC TAB	<input type="checkbox"/>
Unannounced	<input type="checkbox"/>
Justification	
By	
Distribution /	
Availability Codes	
Dist	Avail and/or Special
A-1	

Approved for public release; distribution unlimited



Preface

This effort was possible only because of the good people in the Space Physics branch of the Air Force Geophysics Laboratory. I would like to take this opportunity to thank each and every one of the following: Drs. Santimay and Sunanda Basu, Dr. Robert Burkhart, Dr. Susan Gussenhoven, Dr. David Hardy, Nancy Heinemann, and Dr. Eileen MacKenzie.

Without the help of those mentioned above, it would have been very difficult, if not impossible, to acquire and understand the HILAT data. Since I knew very little about scintillations when I first started this project, I am particularly appreciative of the help Dr. Sunanda Basu and Dr. MacKenzie gave to me. Dr. Hardy was the one who originally came up with this thesis topic, and he was quite helpful with comments and explanations that made some of the more subtle concepts easier to understand. I cannot thank Nancy Heinemann enough, for it was through her tireless efforts that I was able to get the data that I needed.

I wish all the people in the Space Physics branch continued success with the HILAT satellite, which in my view is a credit to its designers. Hopefully more discoveries will be a result of this fascinating program.

Closer to home, I thank Maj James Lange, my physics thesis advisor at AFIT, for his bottomless patience and kindness which made this seemingly impossible task a rewarding learning

experience. Lt Col Joseph Coleman, my statistics advisor, was an invaluable help in assisting with the interpretation of discriminant analysis results and statistics in general.

Last, but certainly not least, I thank my fiance Anne for making the dark days a whole lot brighter.

Table of Contents

	Page
Preface	ii
List of Figures	vi
List of Tables	viii
Abstract	ix
I. Introduction	1
Background	1
Problem Statement	5
Objectives of the Research	5
Scope	6
II. Methodology and HILAT Data	7
Methodology	7
Data	8
Spacecraft Description and Orbit	8
Multifrequency Radio Beacon	9
J-Sensor	10
Magnetometer	12
III. Literature Review	14
Radio Frequency Scintillation	14
Sources of Plasma Structure	24
TID	25
Sporadic E	25
Spread F	26
Polar Cap VHF Scintillation	27
IV. Electron Data Analysis	28
Processing Equipment and Software	28
Graphical Distribution of Electron Enhancements	28
V. Magnetometer Plots	42
VI. Graphical Distribution of Peak Intensities and Descriptive Statistics	49
VII. Discriminant Analysis of Electron Enhancements and Their Relationship to Scintillations	52

	Page
VIII. Conclusions and Recommendations	97
Conclusions	97
Recommendations	99
Appendix A: Individual Distribution Spectra of 21 January 1984 Pass	A-1
Appendix B: Distribution Spectra for Selected Passes	B-1
Appendix C: Discriminant Analysis Results (42 cases) . .	C-1
Appendix D: Discriminant Analysis Results (T=1, 30-38 cases)	D-1
Bibliography	BIB-1
VITA	V-1

List of Figures

Figure	Page
1. The Geometry of the Problem, When the Source is a Satellite	18
2. Diagram of an Irregularity	18
3. S as a Function of $\lambda z/r_e^2$	21
4. $F=S/\sqrt{2}$ PRMS as a Function of $\lambda z/r_e^2$	21
5. J-Sensor Plot: 01:48-01:51 U.T. 17 January 1984	30
6. J-Sensor Plot: 06:50-06:53 U.T. 21 January 1984	32
7A. Distribution Spectra: 24737 sec-24743 sec U.T. 21 January 1984	33
7B. Distribution Spectra: 24745 sec-24749 sec U.T. 21 January 1984	34
7C. Distribution Spectra: 24752 sec-24756 sec U.T. 21 January 1984	35
7D. Distribution Spectra: 24775 sec-24779 sec U.T. 21 January 1984	36
8. Distribution Spectrum: 24739 sec U.T. 21 January 1984	37
9. Histogram of 198 Electron Enhancements	41
10. Magnetometer Plot: 6595 sec-6625 sec U.T. 17 January 1984	43
11. $J_{ }$ Plotted Against PEAK (9 cases)	48
12. Expanded J-Sensor Plot: 6520 sec-6700 sec U.T. 17 January 1984	50
13. Histogram of PEAK Values (73 cases)	51
14. Geometry of Satellite Positions and Line of Site	56
15. Plot of S4 for 17 January 1984 Pass	60

Figure	Page
16. Plot of PRMS for 17 January 1984 Pass	61
17. Geometry of T=1 Situation	63
18. Euclidean Distance	70
19. Euclidean Distance of an Observation From the Centroid	70
20A. Histogram of DS1 (42 cases)	75
20B. Histogram of DS2 (42 cases)	76
20C. Histogram of DP1 (42 cases)	77
20D. Histogram of DP2 (42 cases)	78
21. Plot of DS1 versus DS2	79
22. Plot of DP1 versus DP2	80
23. Theoretical Prediction of Equation 10 Plotted as a Function of r_c	82

List of Tables

Table	Page
1. MLT Distribution Data	40
2. Magnetometer Results	46
3A. Satellite Location Printout	53
3B. Scintillation Data Printout	55
3C. F-Region Penetration Data	58
4A. Data Used in Discrimination Analysis	65
4B. Data Used in Discrimination Analysis (cont)	66
5. Pearson Correlation Coefficient Printout	86
6. Classification Based on CAT, w/PTIME	87
7. Classification Based on CPRMS w/o PTIME	90
8. Discriminant Analysis Results For All Cases (both T=0 and T=1)	92
9. Discriminant Analysis Results For Only T=1 Cases	93
10. Comparison of Discriminant Analysis Results	94

Abstract

The relationship between the observed increase in the flux of low energy (<500 ev) electrons, at an altitude of 800 km and the corresponding amplitude and frequency scintillations of radio waves passing through ionospheric irregularities at 350 km was studied. This data was measured by the electron spectrometer (J-sensor), the magnetometer, and the radio beacon experiment (137 MHz and 413 MHz) of the HILAT satellite. The data analyzed here was taken from January-March 1984. During that time interval, 198 enhancements of electron flux were recorded in the night sectors (magnetic local time), occurring most frequently at 0300 and 2300 MLT.

For 73 of these enhancements, magnetometer data was examined for corresponding geomagnetic disturbances (dB_y/dt), but only nine had such associated disturbances. The average increase in electron number flux for the 73 enhancements was found to be 9.7×10^8 electrons/cm²-sec-ster with a standard deviation of 9.6×10^8 electrons/cm²-sec-ster. Enhancements with number fluxes greater than 2×10^9 electrons/cm²-sec-ster were the same ones that had correspondingly large dB_y/dt values.

When the values of the phase scintillations for 137 MHz (known as PRMS) were plotted against those for 413 MHz, a linear curve that agreed with the theory put forth by Briggs and Parkin resulted. The same was done with the amplitude

scintillation data; the distribution was not as linear, but many points fell along linear curves for limiting large and small values of the traverse radii of irregularities as described by Briggs and Parkin.

For the 42 sets of values for PRMS and S4 used in the discriminant analysis, the increase in integrated number flux (PEAK) and the average electron energy (EAVG) were significant indicators in determining S4 at 137 MHz. The size of the enhancement, as indicated by the time necessary to traverse it (TIME) and the time difference between enhancement encounter and scintillation occurrence (DT) were good indicators for determining the rise of PRMS at both frequencies and the rise of PRMS at 413 MHz by itself.

TIME and DT were also indicative of scintillation increases (S4 and PRMS) at 413 MHz. Results for finding indicators for S4 at 413 MHz, and PRMS at 137 MHz were not statistically significant.

STATISTICAL ANALYSIS OF LOW ENERGY ELECTRONS
AND THEIR RELATIONSHIP TO RADIOWAVE
SCINTILLATIONS

I. Introduction

Background

In order to deter a nuclear attack against the United States it is essential to have a credible capacity to retaliate against such an attack from any potential enemy. One necessary ingredient for maintaining such a force are command, control, and communications (C3) systems that can reliably function during such a conflict and its aftermath (Fremouw, 1983:3).

A major source of degradation of our C3 systems would be radio scintillations associated with high altitude ionospheric plasma irregularities created by nuclear bursts. Since the Defense Nuclear Agency (DNA) is charged with investigating such adverse nuclear effects, the development of these plasma irregularities are of major interest (Fremouw, 1983:5).

Since atmospheric nuclear explosions are forbidden by the Nuclear Test Ban Treaty, it is indeed fortuitous that such irregularities occur naturally under solar produced disturbed geophysical conditions. Although much active experimentation and observation has been done on these irregularities, much

remains to be learned about how these plasma structures develop, evolve, and decay. In fact, these processes are especially more complicated at the higher latitudes than at the equatorial or middle latitudes. This is mainly due to coupling that occurs between the ionosphere and the magnetosphere. For instance, it is believed that precipitating electrons lead to the establishment of the scintillation-producing irregularities, yet the magnetospheric processes responsible for this precipitation are poorly understood (Rino, 1983:1179).

Since the Air Force Geophysics Laboratory (AFGL) is tasked with the study of geophysical phenomena and how such phenomena affect Air Force systems, it would seem then that a joint investigation of radio scintillations produced by enhanced plasma structures would be a well-suited endeavor for both AFGL and DNA.

The DNA Wideband Satellite Experiment launched in 1976 transmitted several phase-coherent radio signals which provided useful three-dimensional information on the configuration of these irregularities. However, in order to perform the previously mentioned study, an orbiting radio propagation experiment, along with other on-board instrumentation, is needed to explore the plasma and free energy sources that are associated with ionospheric irregularities (Fremouw, 1983:4).

The response to this requirement is the DNA-sponsored satellite known as HILAT (High Latitude). HILAT's complement of experiments consists of a multifrequency radio beacon, an

energetic particle detector, a magnetometer, a plasma probe, a driftmeter, and an ultraviolet imager. Hopefully this will provide data for a more complete description and understanding of high latitude plasma structures than before possible.

The characterization of the complex radio signal (amplitude and phase) scintillations would allow one to design methods to compensate for them. A possible long-range goal would be the ability to predict when and under what physical conditions that scintillations occur. Evidently this is being done now, but only very roughly (Fremouw and Wittwer, 1984:100). The study of ionospheric scintillations is of interest to the civilian community as well. Applications include communications with remote sensing, scientific, and commercial satellites in high inclination, i.e., polar, orbits; this includes the recently activated search-and-rescue satellites. For this and other reasons, the National Research Council of Canada has agreed to the collection and sharing of HILAT data with the United States (Fremouw, 1983:6).

As was earlier mentioned, it has been proposed that low-energy electron precipitation in the auroral oval is the primary source of plasma structure in the ionosphere (the F region, to be more specific). Basu et al. performed a case study of the formation of one of these so called "blobs" by low-energy (less than 500 ev) electron precipitation near the equatorward edge of the auroral oval during an auroral substorm. The precipitation event, monitored by a DMSP satellite, caused an

increase in the background ion density by a factor of 2-3 at an altitude of 820 km, bounded by regions of sharp density gradients. Coordinated magnetometer and total electron count measurements showed that the event lasted approximately ten minutes. It was also noted that the number of medium scale (1 km or larger) irregularities responsible for phase and amplitude scintillations increased as well. In this study, scintillation data was obtained from 244 MHz transmissions from a Fleetsatcom satellite in geostationary orbit (Basu et al., 1983:1151-1152).

Since no electric field (or field-aligned current) measurements were available, it was difficult to ascertain the generation mechanisms of the scintillation-producing irregularities. However, since the density enhancement was embedded in the diffuse aurora region with known field-aligned Birkeland currents, there remains the possibility that these same Birkeland currents are destabilizing elements leading to irregularity formation (Basu et al., 1983:1163).

Also, the data indicated the possibility of a fluctuating zonal electric field with alternating eastward and westward components. Since the medium scale irregularities have sufficiently long lifetimes, a fluctuating electric field could introduce instability as well. There is also the possibility that irregularities may grow out of structured low-energy particle precipitation and irregular field-aligned currents (Basu et al., 1983:1163).

With the advent of HILAT, with its driftmeter, magnetometer, and higher spatial resolution of particle measurements, hopefully more can be learned about scintillation-producing irregularities associated with F region density enhancements (Basu et al., 1983:1163).

Problem Statement

The main thrust of this thesis effort is an extension of the study done at AFGL. An important question to be answered is, "How much of a contribution do low-energy electron precipitation events make to the observed scintillation levels occurring in the auroral zone?" By performing a survey of HILAT passes at different magnetic local times, one could determine how often these enhancements occur, whether or not there is any local time dependence, and how often their observation is accompanied by scintillations. In addition, magnetic field characteristics associated with these enhancements could be examined.

Objectives of the Research

The first objective is to investigate the above mentioned possibility of magnetic local time dependence of enhancement occurrence. Second, any magnetic field characteristics associated with these enhancements will be studied.

Third, the electron peak number densities associated with the observed enhancements will be established. Once this is done, the distribution of these number densities could be

plotted, and an average peak number density value might then be available.

As the fourth objective, an attempt to correlate amplitude and phase scintillations described by measured values of the S4 and PRMS indices with the position and magnitude of the particle enhancement will be made.

Scope

This analysis of the relationship between electron enhancements and scintillations is limited to electron energies and number densities measured by the HILAT electron spectrometer (20ev-20kev). Radio scintillation S4 and PRMS data is from the HILAT multifrequency radio beacon; the frequencies to be used are 138 MHz and 413 MHz. Magnetometer data will also be from the HILAT vehicle as well. The time interval of interest in this effort covers approximately the period beginning in early January 1984 up to and including mid-March 1984.

II. Methodology and HILAT Data

Methodology

By using expanded electron spectrometer (herein known as the J-sensor) plots, the number and location in terms of magnetic local time (MLT) of the enhancements can be determined. Using 24 one-hour "bins", the distribution of the number of enhancements versus MLT can be obtained.

The remaining analysis will use only a selected number of representative enhancements. For each of these enhancements, any corresponding changes in the magnetic field (derived from expanded magnetometer data) will be noted. Using printouts from an interactive computer program from AFGL, the peak intensity of the enhancements should be easily available. With this information, a distribution of peak number densities can be plotted. Measuring the width of the enhancements in terms of time (from J-sensor plots) will give the physical size of these "blobs", since the satellite's orbital velocity is known.

The AFGL interactive program can render individual number density distribution spectra continuously over the lifetime of the enhancement; from this some possible insight on enhancement formation and termination might be gained.

Lastly, computer printouts from AFGL containing S4 and PRMS data will be used to attempt correlation of these two parameters with enhancement locations in MLT using available statistical software packages.

The data preparation, analysis, and results for each sub-objective can be found in Chapter IV (Graphical Distribution of Enhancements), Chapter V (Magnetometer Plots), Chapter VI (Graphical Distribution of Peak Intensities and Descriptive Statistics), and Chapter VII (Discriminant Analysis of Enhancements and Their Relationship to Scintillations).

Data

Spacecraft Description and Orbit. The HILAT satellite, also known as P83-1, is a modified Navy Transit satellite modified by the John Hopkins Applied Physics Laboratory in order to perform scientific work. The spacecraft was launched on 27 June 1983 from Vandenberg Air Force Base by a Scout rocket; the mission orbit has a perigee of 800 km and an apogee of 807 km (Potocki, 1984:107).

It was necessary to have an inclination that would result in a high precession rate (in order to sample all possible local times) and good coverage of the magnetic polar region. Consequently the satellite was placed in orbit with an 82 degree inclination. This inclination also allows for direct comparison of data obtained from the DMSP spacecraft as well, since the two vehicles would travel in coplanar orbits during certain parts of the year (Fremouw, 1983:19). HILAT's orbit has a period of 101.95 minutes with the orbital plane precessing at a rate of -7.5 minutes per day, or 24 hours in a period of six months. The orbital velocity is 7.436 km/sec,

with an overhead pass requiring 15.7 minutes to travel from horizon to horizon (Fremouw, 1983:19).

HILAT has no on-board data storage capability; all science and telemetry data is transmitted to receiving stations in real time. Three of the stations (Tromso, Norway, and Ft. Churchill, Canada, both of which are in the auroral zone, and Sondre Stromfjord, Greenland, which is near the polar cusp) are fixed, and the third, located near Seattle, Washington, is transportable (Fremouw, 1983:20).

Multifrequency Radio Beacon. This HILAT experiment is in actuality the modified spare payload from the Wideband mission mentioned in the "Background" section. Its transmission frequencies are 137.676 MHz, 378.609 MHz, 413.028 MHz, 447.447 MHz, and 1239.084 MHz (L-band) (Fremouw, 1983:12).

The first frequency lies in the very high frequency range (VHF) and the next three lie in the ultrahigh frequency (UHF) range. All four are used for complex-signal scintillation measurements, whereas the L-band frequency is used only for amplitude scintillation measurements. The L-band frequency also serves as a phase reference for the VHF and UHF signals, as well as the telemetering signal to the ground stations (Fremouw, 1983:12).

Although not explicitly used in this analysis, the three UHF signals are also used to obtain total electron count (TEC). The change in TEC is proportional to the measured difference in phase; the phase difference is in turn proportional to

frequency and changes in the phase path. The changes in phase path can be due to either a change in the real path (where the change in phase would be proportional to frequency) or small changes in the refractive index (where the change in phase is inversely proportional to frequency). By making measurements on adjacent UHF frequencies, it will be possible to tell if the phenomenon is due to changes in height or a change in TEC (Davies, 1969:229-230).

The L-band and the UHF transmissions have left circular polarization. This is done to minimize interaction between the UHF and L-band antennas, which are nested together on the earthward surface of the vehicle. The VHF antenna on the other hand is mounted on the end of one of the solar panels. The effective radiated power levels near the center of the antenna beams are given as 26 dBm at VHF, 21 dBm for each of the UHF signals, and 30 dBm at L-band (referenced to 1 milliwatt) (Fremouw, 1983:14).

J-Sensor. The J-sensor represents a means to analyze a plasma irregularity in terms of measured electron flux. This instrument employs six cylindrical curved plate electrostatic analyzers arranged in three pairs. Each analyzer consists of three components: an aperture entrance, a set of two concentric cylindrically curved plates, and a set of channeltron detectors. A channeltron is an electron multiplier consisting of a hollow lead glass tube with a large potential difference between the two ends; electrons impacting on the front

end eject secondary electrons which, after acceleration by the applied electric field, strike the walls of the tube, thereby ejecting even more secondary electrons. This cascade of electrons renders a measurable pulse at the channeltron output which is then counted by the detector's electronics (Hardy et al., 1984:125,130).

The cylindrically curved plates of the analyzer selects only those electrons with a given energy corresponding to an applied voltage across them. If the velocity of the incoming electron and the applied electric field force are matched, the electron will follow a trajectory that causes it to impact the front end of the channeltron (Hardy et al., 1984:125).

For each analyzer, one set of cylindrical plates has a 60 degree radius of curvature, and the other set has a 127 degree radius of curvature. The latter detector measures electrons in eight semilogarithmically spaced channels between 20 and 632 ev with an acceptance angle of 4 by 6 degrees. The former measures electrons in a likewise manner, but with an energy range of 632 to 20,000 ev and an acceptance angle of 2 by 9 degrees (Hardy et al., 1984:125).

The high-energy detector has a geometric factor at the peak of its response curve of .001 square cm-steradian with a fractional energy-spectral channel width of 9 percent. For the low-energy detector, the geometric factor is .0004 square cm-steradian with a corresponding channel width of 13 percent

(Hardy et al., 1984:126).

The three analyzer pairs are oriented so that one pair measures electrons incident from the satellite's local zenith (parallel with the magnetic field lines at high latitudes). The second pair is angled 40 degrees from local zenith, and the third pair measures electrons from the local nadir (upwelling energetic electrons) (Fremouw, 1983:16).

The J-sensor was also designed to work in three different modes. In mode 1, only the low-energy zenith analyzers are used. Twenty-four 8-point spectra over the low energy range are gathered in one second; this results in a spatial resolution of 300 meters (that is, the satellite travels 300 m in the time necessary for one spectrum). In mode 2, all channels of both zenith sensors are sampled, giving 12 16-point spectra per second, and a spatial resolution of 600 meters. Mode 3 operation uses all channels in all three pairs; this gives four 16-point spectra per second in all three directions, and a spatial resolution of 1.8 km (Hardy et al., 1984:126).

Magnetometer. The three-axis fluxgate magnetometer was originally part of the attitude determination system of the Transit spacecraft. By adding a microprocessor, improved resolution and sampling rates became possible (Potemra et al., 1984:120).

The three magnetometer sensors are arranged so that two are on two different solar panels, with the remaining sensor affixed to the spacecraft body. If we define a right-handed

satellite centered coordinate system with positive x in the direction of the velocity vector and positive z pointing downward, the solar panel sensors are in the positive x and y directions. At the polar regions, the resulting x-y plane is almost perpendicular to the magnetic field lines; consequently, these sensors will detect magnetic disturbances caused by field-aligned currents. The x and y sensors, when aligned in this fashion, also minimize the effect of magnetic fields associated with currents flowing in the solar panels. The z sensor will essentially measure the strength of the total magnetic field when over the pole, since the satellite's z direction will be almost parallel to the field lines (Potemra et al., 1984:120).

The HILAT magnetometer provides a magnetic field resolution of 13.4 nanoteslas. The magnetometer processor can provide 20 magnetic field samples per second; as a result, field-aligned currents can be detected with a spatial resolution of 400 meters (Potemra et al., 1984:121).

III. Literature Review

Radio Frequency Scintillation

One publication discovered early in the literature review was a compilation of papers edited by Aarons; although many of these papers discussed scintillations as they relate to distant radio stars, many of the concepts and techniques were easily applicable to radio transmitting satellites. Except for the paper by Briggs and Parkin, all works referenced in this section are from Aarons' book.

A paper by Harrower was concerned with the theoretical interpretation of radio star scintillations. The general characteristics of scintillations and the associated ionospheric irregularities were discussed, along with methods in which the size, shape, orientation, and drift velocity of the irregularities causing them could be found (Aarons, 1963:38-64).

Aarons himself presented results done with low elevation angle scintillations obtained through observations made at the Sagamore Hill Radio Observatory. One of the discoveries indicated that scintillations are produced both in the troposphere and the ionosphere (Aarons, 1963:68-75).

Scintillations of tropospheric origin were observed to have long periods (20 sec-2 min) with good correlation of individual fluctuations measured at different frequencies. Since the radio source (Cygnus), observed in the 50 to 400 MHz range, rose in the sky with its line of sight in the F region

passing through auroral irregularities, scintillations were always evident (Aarons, 1963:75-79).

The correlation of scintillations with geomagnetic activity was investigated as well. On quiet days, scintillations associated with the rising of Cygnus had the same power density spectra (a semilogarithmic plot of received power versus time) among the observing frequencies, but the recorded peaks and valleys were not always correlated in time. Differential refraction in the 50-200 MHz range was believed responsible for this effect. A single scattering process (thin layer of irregularities) was thought to be a possibility as well (Aarons, 1963:79).

On geomagnetically active days, multiple scattering (diffraction process) caused the power spectra for the different observing frequencies to differ. Here the scale of the ground projection of the observed irregularities was such that a low scintillation index at 54 MHz and a high index at 244 MHz resulted, an example of the inversion effect (Aarons, 1963:79-81).

This effect, which was discussed by Aarons et al. in another publication, manifests itself when the correlation distance on the ground under multiple scattering conditions is smaller than the antenna diameter. Several peaks and nulls exist across the antenna dish, and due to a lack of coherence, scintillation peaks and nulls combine to produce a composite low index. As the index of refraction is inversely proportional

to frequency squared, higher frequencies experience less scattering; therefore, the correlation distances on the ground are almost equal to the actual size of the irregularities. As a result, the scintillation index appears to increase with frequency, which, as will soon be shown, is usually not the case (Aarons, 1963:81-83).

In another paper by Mass where various satellite techniques for studying propagation in the ionosphere were surveyed, scintillations were considered as one of the major disruptive effects. According to Mass, amplitude scintillations are the most detrimental with respect to communications. It was also pointed out that good correlation exists between the occurrence of satellite amplitude scintillations and amplitude scintillations associated with radio stars (Aarons, 1963:283).

Frihagen presented findings on the altitude of the scintillation producing irregularities; his results indicated that this region was between 300 and 550 km. The size and the orientation were also determined, with the irregularities in this case being at least 1.3 km long and no more than 3.6 km wide. They were also anisotropic, i.e., they were aligned with the magnetic field lines (Aarons, 1963:342).

The final paper reviewed from Aarons' book was by Lizka. His results taken from various satellite studies of the auroral zone indicated that auroral sporadic-E regions produced scintillations. Also, observations from Explorer 7 showed that the frequency of scintillation occurrence decreased as distance

from the auroral zone increased (Aarons, 1963:345-346).

After reviewing the previously cited works, it became apparent that no common scintillation index was in use (at least in the early 1960s, when most of the papers were written). Since the S4 amplitude index and the PRMS are the scintillation parameters of interest in this thesis effort, it was necessary to find some source in the literature that would explain just what exactly is being measured by these parameters.

A study on the variation of radio star and satellite scintillations with zenith angle by Briggs and Parkin provided actual mathematical expressions for both PRMS and the S4 index. They start by considering fluctuations on a wave as it passes through an irregular medium; in this instance, the medium is considered as a thin diffracting screen. Since the frequencies most likely to be used will suffer little ionospheric absorption, the screen will produce across the emerging wavefront phase variations only and no amplitude variations. Only when the wave propagates beyond the screen do amplitude fluctuations develop (Briggs and Parkin, 1963: 339-340).

After discussing the geometry of the problem (Fig. 1) and the propagation of a wave through the medium (see Fig. 2 for a schematic representation of an irregularity), the general equation for the root mean square fluctuation of phase produced in a wave traveling along the z-direction is (Briggs and Parkin, 1963:345)

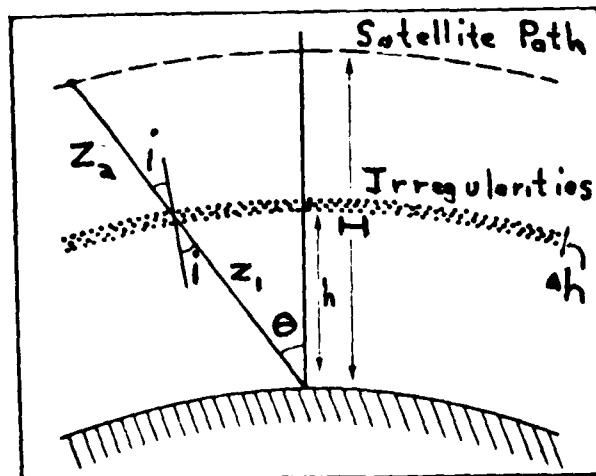


FIG 1. The Geometry of the Problem,
When the Source is a Satellite
(Briggs and Parkin, 1963:341)

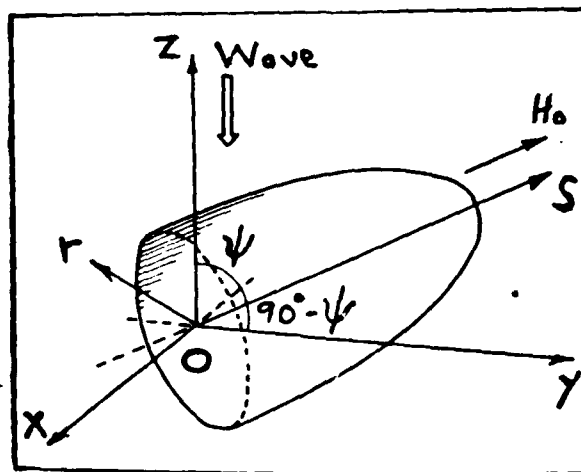


FIG 2. Diagram of an Irregularity
(Briggs and Parkin, 1963: 343)

$$PRMS = \pi^{1/4} r_e \lambda (4 \bar{N}^2 \Delta h \alpha \sec i)^{1/2} (\alpha^2 \sin^2 \psi + \cos^2 \psi)^{-1/4} \quad (1)$$

where

r_e = classical electron radius

λ = wavelength of signal

ΔN = mean excess electron density

r_0 = traverse radius of irregularity

α = ratio of irregularity length to width

The variable Δh is the thickness of the irregularity, and the angle i is the angle of incidence that the radio beam makes with respect to the irregularity's surface (Fig. 1). The angle ψ appears in Fig. 2; it is the angle between the magnetic field vector H_0 and the direction of wave propagation.

The only factors that vary with zenith angle Θ are i and ψ . The expression is simplified by assuming that N^2 , Δh , and r_0 are independent of Θ :

$$PRMS = K \lambda (\sec i)^{1/2} (\alpha^2 \sin^2 \psi + \cos^2 \psi)^{-1/4} \quad (2)$$

where K is a constant of proportionality. For isotropic (non-aligned with the magnetic field) irregularities, further simplification shows $PRMS$ varying as $\lambda (\sec i)^{1/2}$ (Briggs and Parkin, 1963:345).

Briggs and Parkin then reference a paper by Mercier to explain how the amplitude scintillation index S^2 behaves. S^2 is used to measure scintillation depth, and it is expressed as

$$S^2 = \langle R^2 \rangle^{-2} (\langle R^4 \rangle - \langle R^2 \rangle^2) \quad (3)$$

where R is wave amplitude. The quantity S also varies as a function of $\lambda z/r_o^2$ (Fig. 3); note that near the origin S is proportional to z . Briggs and Parkin refer to this region as the "near zone". Further away from the screen S approaches a limiting value, and S becomes independent of z ; this is the "far zone". The limiting value of S far from the screen is

$$S = \{1 - \exp(-2(\text{PRMS})^2)\}^{1/2} \quad (4)$$

as determined by Mercier (Briggs and Parkin, 1963:346).

For small values of PRMS, S can be expressed as

$$S = \sqrt{2} (\text{PRMS}) (1 + \pi^2 r_o^4 / 4 \lambda^2 z^2)^{-1/2} \quad (5)$$

where the limiting value far from the screen is $\sqrt{2} (\text{PRMS})$ (Briggs and Parkin, 1963:346-347).

Mercier's paper applied to isotropic irregularities. For the more general anisotropic case, James put forth the following relationship

$$S = \sqrt{2} (\text{PRMS}) \{1 - (\cos u_1 \cos u_2)^{1/2} \cos(1/2)(u_1 + u_2)\}^{1/2} \quad (6)$$

where $\tan u_1 = 2\lambda z / \pi r_o^2$ and $\tan u_2 = 2\lambda z / \pi \beta^2 r_o^2$. The parameter β is an axial ratio of the phase pattern expressed as (Briggs and Parkin, 1963:344,347)

$$(\alpha^2 \sin^2 \psi + \cos^2 \psi)^{1/2} \quad (7)$$

For the case of scintillations of satellite transmissions caused by anisotropic irregularities, the PRMS value can be

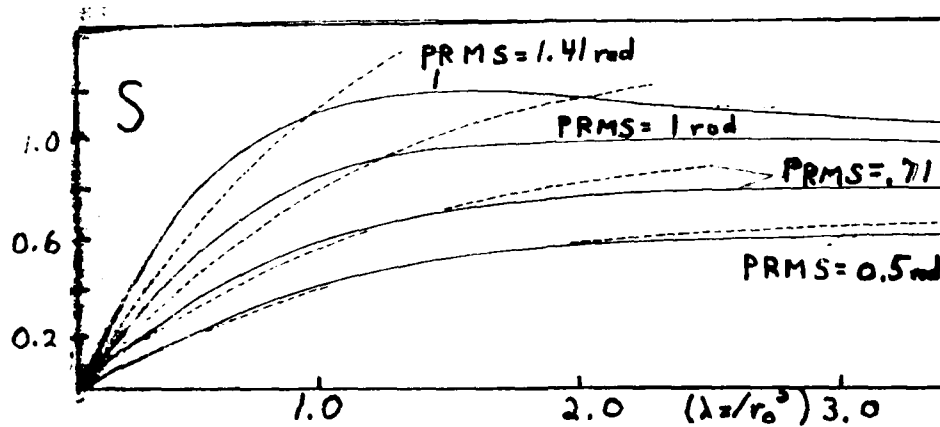


FIG 3. S as a Function of $\lambda z/r_0^2$
(Briggs and Parkin, 1963: 347)

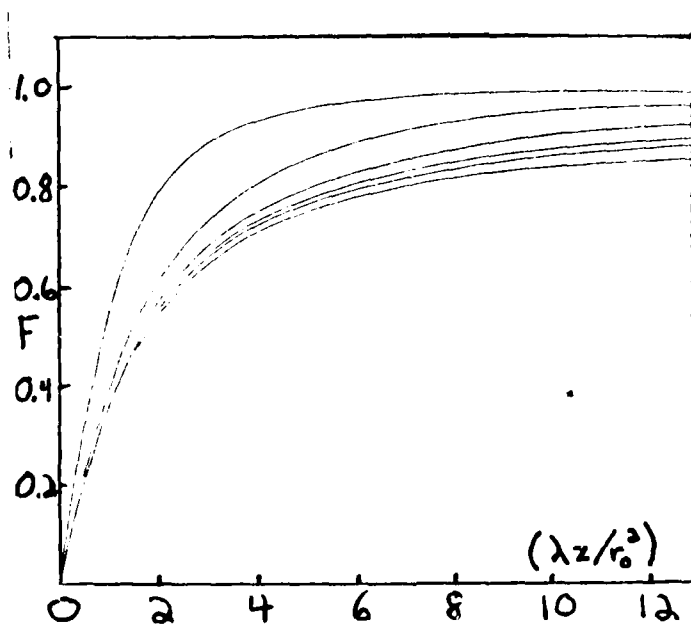


FIG 4. $F = S/\sqrt{2} \text{ PRMS}$ as a Function
of $\lambda z/r_0^2$
(Briggs and Parkin, 1963:348)

found with Eq (2), and β can be determined from Eq (7). The scintillation depth can be determined from either Eq (6) or Fig. 4; however, z in Eq (6) must be replaced by $z_1 z_2 / (z_1 + z_2)$. The values of z_1 and z_2 (Fig. 1) are determined by (Briggs and Parkin, 1963:358)

$$z_1 = (R_0^2 \cos^2 \theta + 2 R_0 h + h^2)^{1/2} \quad (8)$$

$$z_2 = (R_0^2 \cos^2 \theta + 2 R_0 h + H^2)^{1/2} - z_1 \quad (9)$$

In the case where two frequencies are being used by the satellite, the ratio of the scintillation depth is independent of PRMS. This ratio is given as

$$S(\lambda_1)/S(\lambda_2) = \lambda_1/\lambda_2 (1 + \pi^2 r_0^4 / 4 \lambda_1^2 Z^2)^{-1/2} (1 + \pi^2 r_0^4 / 4 \lambda_2^2 Z^2)^{1/2} \quad (10)$$

where $Z = z_1 z_2 / (z_1 + z_2)$ (Briggs and Parkin, 1963:360).

The authors go on to say that for small values of r_0 in the far zone, the limiting case of Eq (10) is (Briggs and Parkin, 1963:355)

$$S(\lambda_1)/S(\lambda_2) = \lambda_1/\lambda_2 \quad (11)$$

If r_0 is large (observations made in the near zone), we have

$$S(\lambda_1)/S(\lambda_2) = (\lambda_1/\lambda_2)^2 \quad (12)$$

As was mentioned previously, when this paper was written, different measures of scintillation depth were in use.

Briggs and Parkin felt that their theoretical calculations

would not be comparable to experimental data unless some relationship between the two were specified (Briggs and Parkin, 1963:362).

When radio waves are received from a satellite, recorder deflection is proportional to the signal amplitude. Two measurements, the mean deviation (S1) and the root-mean-square deviation (S2) are possible. S1 and S2 can be expressed as (Briggs and Parkin, 1963:362)

$$S1 = \langle R \rangle^{-1} (\langle R - \langle R \rangle \rangle) \quad (13)$$

$$S2 = \langle R \rangle^{-1} \{ \langle R - \langle R \rangle \rangle^2 \}^{1/2} \quad (14)$$

When observing radio star scintillations, recorder deflection is proportional to R^2 , or received power. The two measurements, S3 and S4, are expressed as (Briggs and Parkin, 1963:363)

$$S3 = \langle R^2 \rangle^{-1} (\langle R^2 - \langle R^2 \rangle \rangle) \quad (15)$$

$$S4 = \langle R^2 \rangle^{-1} \{ \langle R^2 - \langle R^2 \rangle \rangle^2 \}^{1/2} \quad (16)$$

Although not readily apparent, Eq (16) and Eq (3) give similar results, i.e., $S=S4$. The authors were then able to develop empirical relationships that relate S1, S2, and S3 to S4 (Briggs and Parkin, 1963:364-365)

$$S1 = 0.42 S4 \quad (17)$$

$$S2 = 0.52 S4 \quad (18)$$

$$S3 = 0.73 S4 \quad (19)$$

Based on private communications with Dr. Sunanda Basu, PRMS is inversely proportional to frequency for all frequencies, in agreement with Eq (1). This is not at all the case with S4, as can be seen in either Eq (5) or (6). A good rule of thumb according to Dr. Basu is that S4 is inversely proportional to frequency to the three-halves power, and only for S4 values less than approximately .5 or .6 (Basu, 1984: personal interview).

Sources of Plasma Structure

There are many mechanisms believed responsible for the creation of plasma irregularities; in addition to precipitating electrons what follows is a sample of some of the studies done and some of the resulting theories concerning irregularity formation.

One of the earlier explanations was offered by Dagg concerning current flow from an induced electromagnetic force. At the height of the D region, ions and electrons move with neutral particles transversely to the geomagnetic field lines. This motion is transferred along the field lines to the higher ionospheric layers, which is between 100 to 125 km high. Pressure variations in the lower atmosphere effect electrons and ions in the E layer. The conductivity of the ionosphere at this altitude is the same both parallel and transverse to the field lines; consequently, the resulting charged particle motion mimics a moving conductor in a reciprocating dynamo.

The resulting current flow manifests itself as a change in the magnetic elements (Aarons, 1963:40).

TID. Many researchers have investigated traveling ionospheric disturbances (TID), which are essentially large electron density waves (more than 1500 km wide) propagating in the F region. The origin of these waves may be linked to acoustic gravity waves propagating in the thermosphere (200 to 500 km). Internal gravity waves are atmospheric disturbances with periods ranging from 10 minutes to several hours. A wave duct may result between a reflecting region and the surface where these gravity waves are reflected in a thermally structured atmosphere. In cases where reflection is not quite total but still strong, some wave energy can "leak" into the higher ionosphere (Stevens, 1973:(6-1)-(6-3)). Friedman, Elkins and Slack, and Yeh have contributed papers concerning the TID phenomenon and its relationship to plasma structures (Friedman, 1966:1033-1054; Elkins and Slack, 1969:421-439; Yeh, 1972:709-719).

Sporadic E. Under certain conditions, irregularities are aligned with the geomagnetic field which occur in the E region near the magnetic equator. A mechanism put forth by Farley responsible for these irregularities is the two-stream, or plasma ion wave instability. A plasma with two or more interconnecting streams of charged particles will be unstable if the mean velocity of the particles of one stream is much greater than the mean velocity of the particles of the other

(Stevens, 1973:(6-9)).

Farley put forth the arguemnt that irregularities should occur in the equatorial electrojet because of two-stream instabilities. Farley also argued that similar irregularities appearing in the polar regions are caused by auroral electrojets (Farley, 1963:6083-6097). Others that have conducted sporadic E research are Ireland, Preddey (Ireland and Preddey, 1967:137-148) and Goodman (Goodman, 1967:607-612).

Another instability in the equatorial electrojet is the gradient drift, or $E \times B$ instability. Here E is the ambient background electric field and B is the geomagnetic field. Farley and Balsey studied the dependency of electrojet irregularities on magnetic field and an associated critical value (Farley and Balsey, 1973:227-239). Sudan et al. have studied this instability's effect as well on small scale irregularities as observed by radar (Sudan, 1973:240-248).

Spread F. This phenomenon of the F region is characterized as an apparent thickening found in the reflecting regions believed to be caused by vertical electron density inhomogenieties. Although by definition spread F is observed below the critical frequency of the F region, many feel these irregularities are responsible for scintillations observed at VHF and UHF frequencies (Stevens, 1973:(6-15)).

A proposal by Liu and Yeh employs the Rayleigh-Taylor instability as the mechanism which causes spread F. This instability is due to the separation between a heavy upper

fluid and a lighter lower fluid, which is unstable in a gravitational field. An analogous situation occurs in the ionosphere, where the density gradient increases with altitude. After the application of a perturbation, the system will be stable at the lowest possible potential energy, with extra energy transformed into the kinetic energy of instability (Liu and Yeh, 1966:1407-1416). Liu and Yeh developed a dispersion relation showing that when the height gradient of electron density is positive and deep, instabilities may result. Both felt experimental data supported their theory (Liu and Yeh, 1966:1283-1291). Both Farley and Reid have independently studied the spread F phenomenon in both the polar and non-polar regions as well (Farley, 1960:869-877; Reid, 1968:1627-1640).

Polar Cap VHF Scintillation. After studying 40 MHz scintillation observations taken via satellite over the polar regions, Frihagen deduced that scintillation depth was independent of geomagnetic activity, time of day, or satellite position. He went on to develop a model where particle precipitation from the interplanetary medium resulted in F region irregularities. To produce the observed irregularities, Frihagen calculated a spatial variation value of $10^{11} \text{ m}^{-2} \text{ sec}^{-1}$ at one Kev as being a required value necessary to sustain "blob" production (Frihagen, 1969:81-92).

IV. Electron Data Analysis

Processing Equipment and Software

The computer used to perform the necessary data analysis was the Control Data Corporation Cyber 6000, which is primarily used by the Aeronautical Systems Division but is also available for student use as well. The primary reason why the Cyber was selected is because the required statistical analysis program resides in the Cyber system.

This statistical analysis software is the Statistical Package for the Social Sciences (SPSS), designed by Nie et al. originally at Stanford University in 1965. This package was selected because it is quite user-friendly and it is well documented. In this effort the two subprograms FREQUENCIES and DISCRIMINANT were the primary SPSS routines used.

Also, enlarged J-sensor plots and distribution spectra that are products of an interactive program were used in this research effort. This program was designed by Dr. Robert Burkhart of Emmanuel College, which is closely affiliated with AFGL.

Graphical Distribution of Electron Enhancements

The first subobjective of the research is to see how the low-energy electron enhancements are distributed in magnetic local time (MLT). Since this and the remaining subobjectives all study some aspect of these enhancements, it would be prudent at this point to define just what constitutes an

enhancement and show an example.

Before doing that, we need to define the three measurements EAVG, JETOT, and JTOT that appear on a J-sensor plot. If one considers the differential number flux $J_n(E_i)$ (electrons/cm²-sec-ster-keV) where i runs from 1 to 16 (16 channels) and E_i is the central energy of each channel in keV, then the integral number flux JTOT is expressed as

$$JTOT = J_n(E_1)(E_2 - E_1) + \sum_{i=2}^{15} J_n(E_i)((E_{i+1} - E_{i-1})/2) + J_n(E_{16})(E_{16} - E_{15}) \quad (20)$$

Similarly, the differential energy flux is $J_E(E_i)$ (keV/cm²-ster-keV); the expression for the integrated energy flux is

$$JETOT = J_E(E_1)(E_2 - E_1) + \sum_{i=2}^{15} J_E(E_i)((E_{i+1} - E_{i-1})/2) + J_E(E_{16})(E_{16} - E_{15}) \quad (21)$$

Finally, the expression for the average energy is just the integrated energy flux divided by the integrated number flux (JETOT/JTOT). On the J-sensor plots EAVG is expressed in keV (Hardy, undated:8-9).

Fig. 5 is an example of the J-sensor plots mentioned in the "Methodology" section in Chapter 1. This data is from the Tromso site, taken from 1:43:47 to 1:53:45 U.T. on 17 January 1984. Fig. 5 is actually an expanded portion of the total pass; the time of interest is 1:48:40 to 1:51:40. Notice the two peaks appearing in the bottom JTOT (integrated number flux) panel at approximately 1:50:01 and 1:50:16. Notice also that both peaks are superimposed on what is known as the diffuse

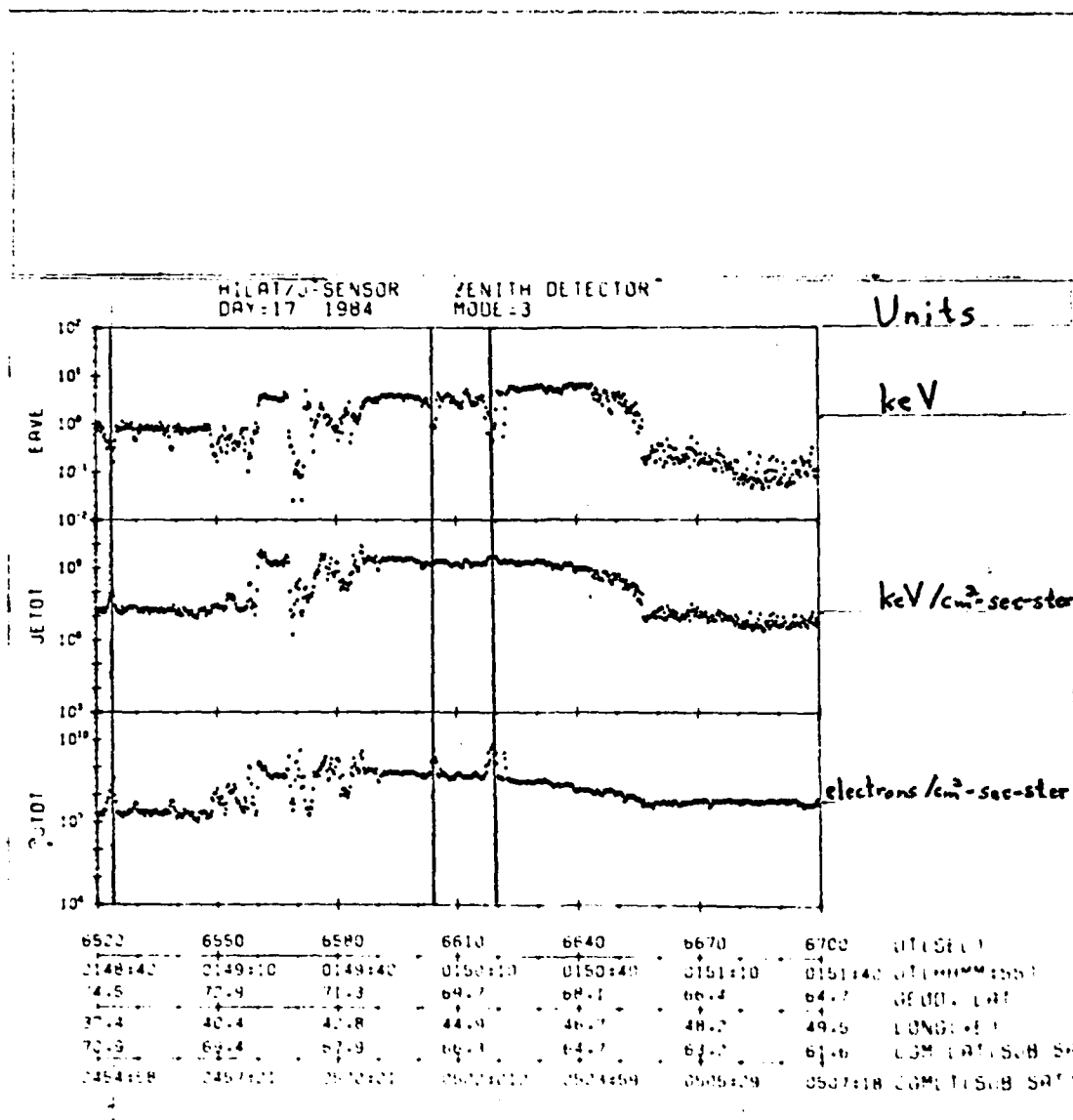


FIGURE 5. J-Sensor Plot: 01:48-01:51 U.T. 17 Jan. 1984

aurora, which runs from approximately 1:49:50 to about 1:50:55. The region immediately preceding this (1:49:10 to 1:49:50) is the so-called discrete aurora, and any such peaks found in this region are not considered enhancements as defined here.

The two peaks have corresponding troughs, or 'cutouts' in EAVG (average energy in Kev, top panel) which are approximately an order of magnitude less than the ambient background energy. In summary, a low-energy electron enhancement has a JTOT peak in the diffuse aurora and a corresponding drop in EAVG.

Distribution spectra (Fig. 7) are more quantitative indicators of what constitutes an enhancement. In Fig. 6 we have an enhancement recorded at Sondrestrom on 21 January 1984 at 6:52:20. Fig. 7 shows the distribution spectra for the entire pass (24731 sec to 24803 sec after midnight U.T.), or converting into the more familiar hour, minutes, seconds format, 6:52:11 to 6:53:23. We have a three-dimensional plot of the logarithm of the energy in ev versus the logarithm of the differential number flux $J_n(E)$ (electrons/square cm/sec/ster/ev) versus time. Note the increase in the flux value at the lower end of the energy axis shortly after 24738 seconds, corresponding with the observed enhancement. This is far more evident if we examine the individual distribution spectra, which appears in Fig. 8 and Appendix A.

Since we are working with Mode 3 data, we have four individual distribution spectra per second. Looking at the very

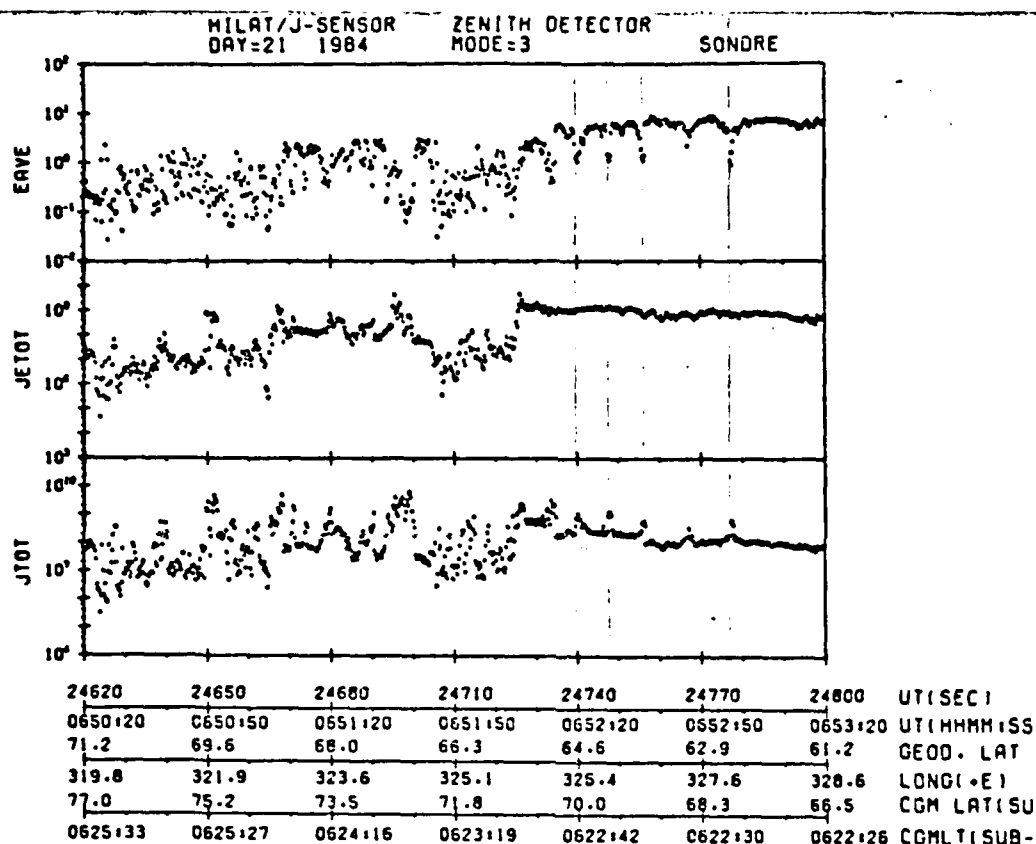


FIGURE 6. J-Sensor Plot: 06:50-06:53 E.L. 21 Jan. 1984

MODE = 3 1984 DAY 21 KP = 0

ZENITH

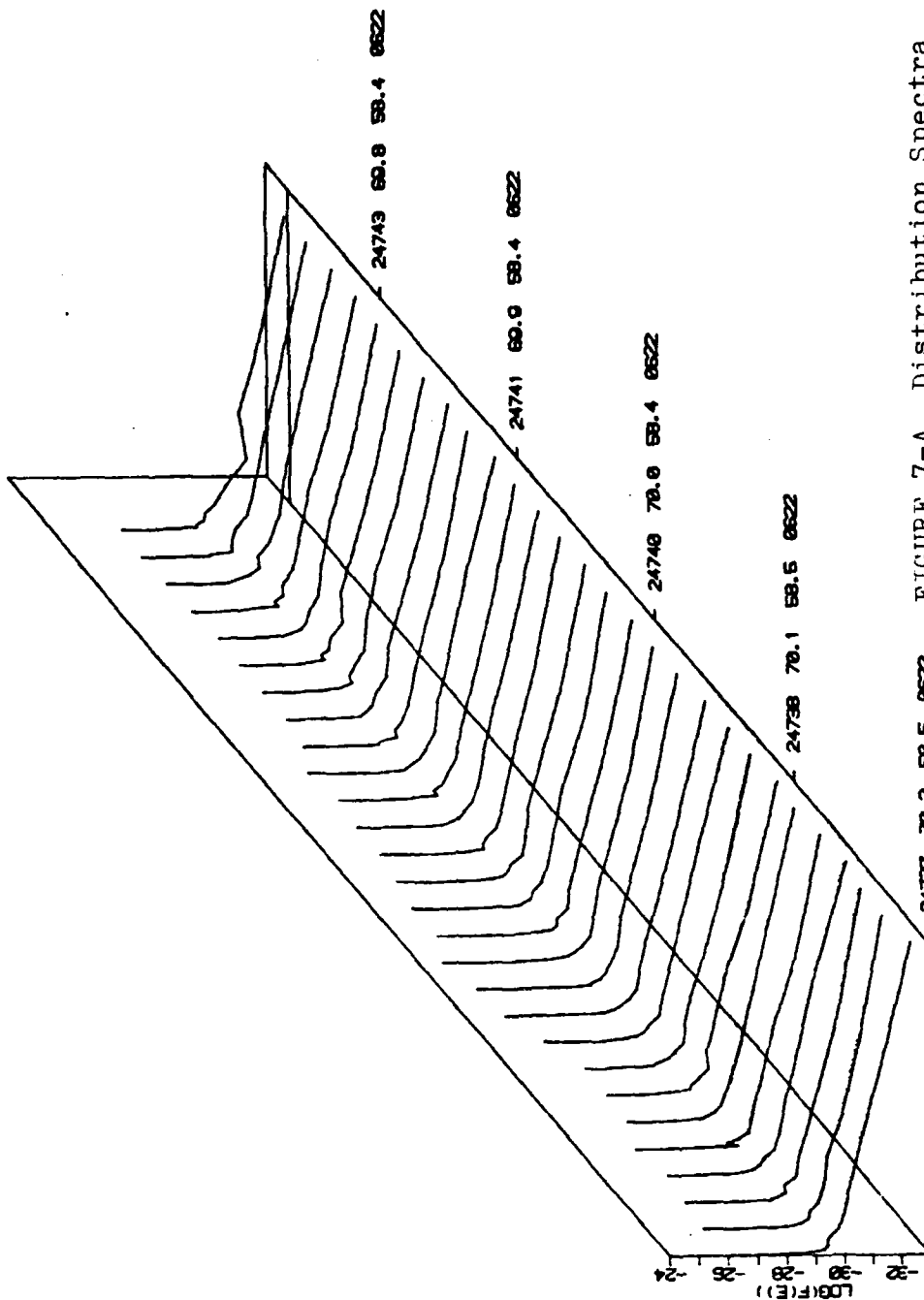


FIGURE 7-A. Distribution Spectra
24737 sec-24743 sec U.T.
21 January 1984

24737 70.2 59.5 0622
UT MLAT MLON O3MLT

MODE = 3 1984 DAY 21 KP = 0

ZENITH

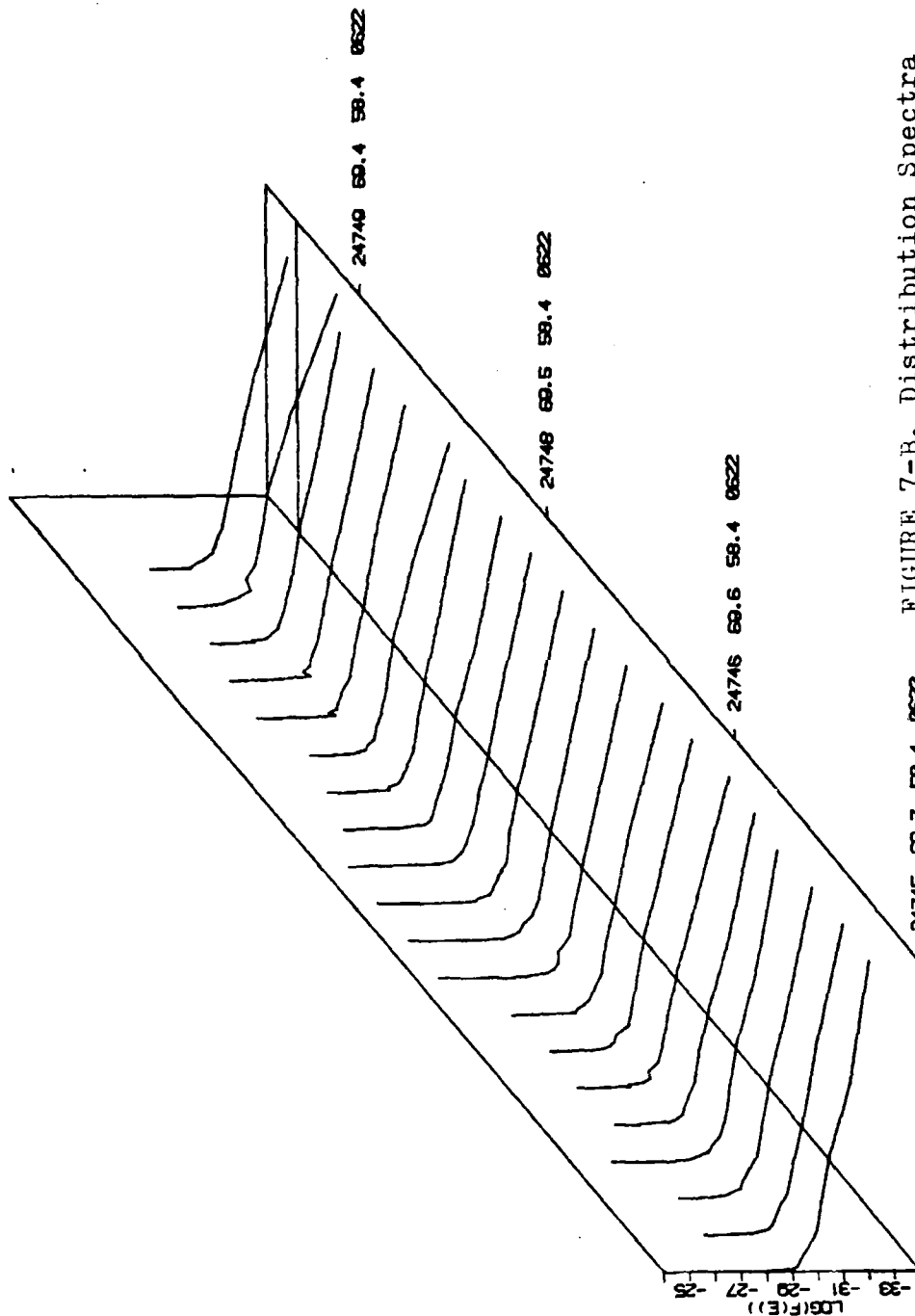


FIGURE 7-B. Distribution Spectra

24745 sec-24749 sec U.T.

21 January 1984

MODE = 3 1984 DAY 21 KP = 0
ZENITH

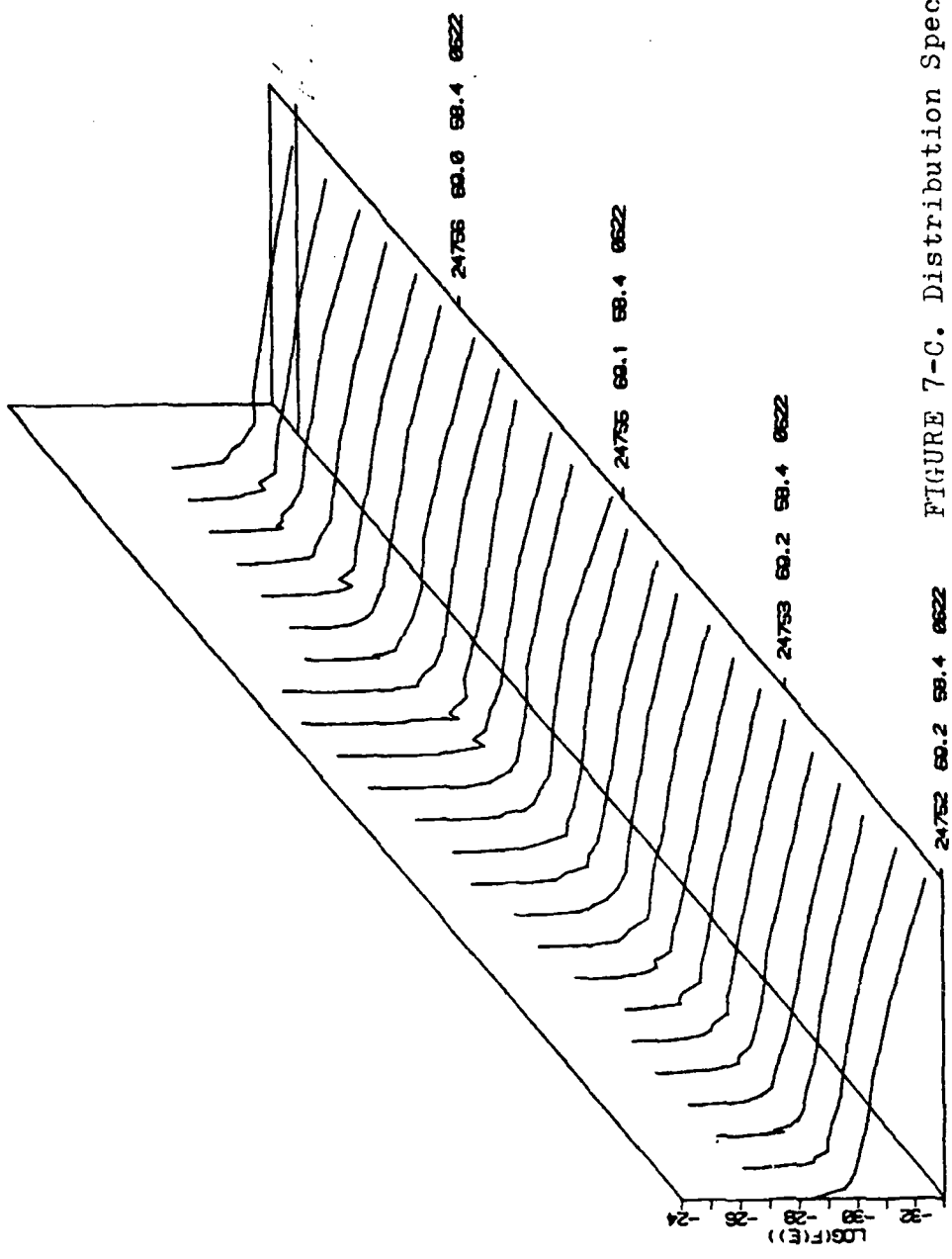


FIGURE 7-C. Distribution Spectra
24752 sec-24756 sec U.T.
21 January 1984

MODE = 3 1984 DAY 21 KP = 0
ZENITH

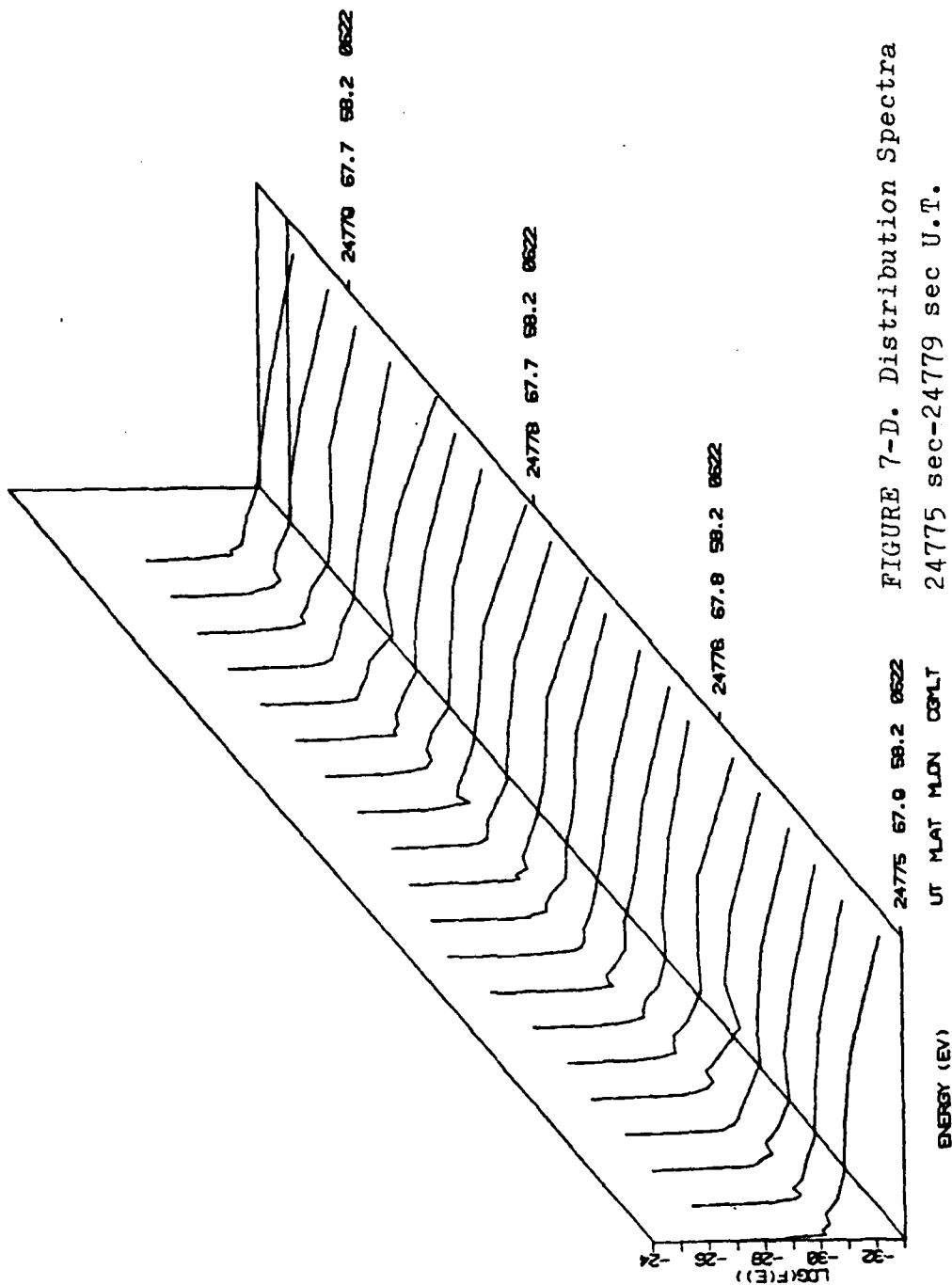


FIGURE 7-D. Distribution Spectra
24775 sec-24779 sec U.T.
21 January 1984

MODE = 3 1984 DAY 21 KP = 0
ZENITH

UT M4T M4ON C4PLT
24739 70.0 59.5 8622

N = .61 1 = .3510E+08
N = 1.81 1 = .7034E+06

CHANNEL	RAW COUNTS	DSPC	FSPC
1	527.0	7.23	-24.86
2	115.0	6.36	-25.04
3	20.0	5.38	-27.15
4	5.0	4.56	-28.17
5	0.0	4.56	-28.43
6	0.0	4.37	-28.82
7	0.0	4.26	-28.11
8	11.0	4.21	-28.38
9	33.0	4.27	-28.54
10	51.0	4.10	-28.82
11	103.0	4.24	-28.90
12	135.0	4.21	-30.24
13	135.0	4.06	-30.68
14	60.0	3.64	-31.24
15	12.0	2.76	-32.33

AEGY 2.43
LOG EFLX 0.01
LOG IFLX 8.63
E1= 28
E2= 632
E3= 20000

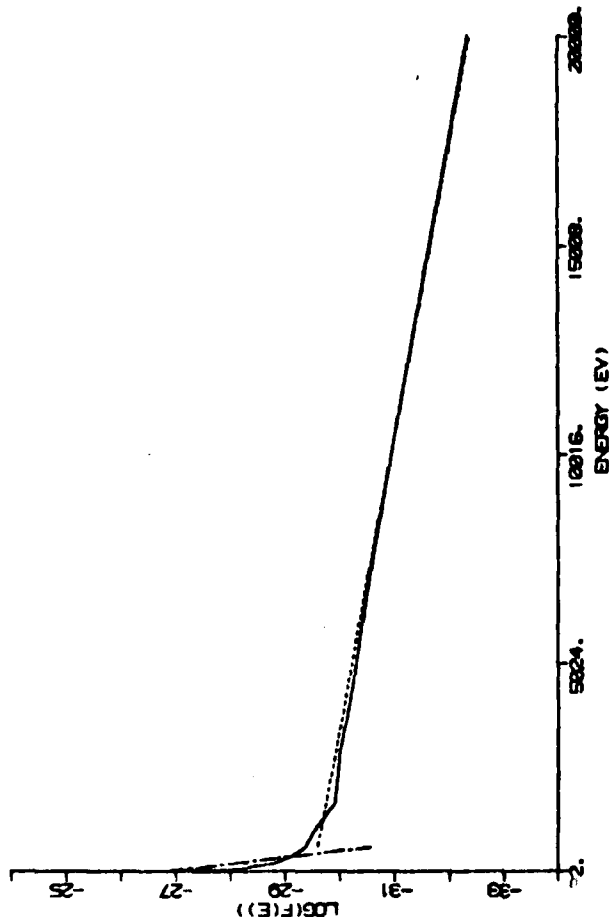


FIGURE 8. Distribution Spectrum: 24739 sec U.T.
21 January 1984

CURRENT END POINTS ARE E1= 1 E2= 0 E3= 15
DO YOU WANT TO CHANGE THEM (Y) OR NOT (N) ?
CONTINUE (Y) OR RETURN TO MAIN MENU (N) ?
SAME ONE AGAIN (Y) OR NEXT ONE (N) ?

first one (Fig. 8) starting at 24739 seconds we have a bi-Maxwellian distribution curve (actually the logarithm of this distribution $F(E)$ versus energy in ev). In the upper left-hand corner we have the parameters, electron density n and temperature T , that characterize both the low energy and high energy curve. Immediately below that we have for each J-sensor channel the number of raw counts registered; the information in the other two columns were not used.

The quantity AEGY appearing below the raw counts table is the average energy EAVG in Kev. The endpoints for the two curves are specified by channel; in this case E1 is the 20 ev channel, E2 (the "breakpoint") is the 632 ev channel, and E3 is the 20 Kev channel. By inspecting the graph we see that both curves are fairly Maxwellian in nature.

Note that as we look at subsequent individual spectra, we see a significant increase in low energy counts and a consequent lowering of average energy EAVG. At the enhancement's peak we have the maximum count in the low energy channels (20-385 ev), with a minimum value of EAVG (1.04 Kev). As we approach the end of the enhancement we get a substantial lowering of the low energy counts and an increasing EAVG value. It was not possible to get distribution spectra for every individual enhancement, so only a few selected cases appear in Appendix B.

In order to establish the MLT distribution of the enhancements, passes from 9 January 1984 to 13 March 1984 were

examined (not on consecutive days; see Table 1). A total of 198 enhancements were obtained, and the corresponding hour of corrected magnetic local time (also obtained from the J-sensor plots) were noted. This data was entered into the Cyber and an SPSS program (FREQUENCIES) was executed.

Basically, FREQUENCIES determines frequency distribution tables and descriptive statistics. In this first subobjective we are interested in how the enhancements are distributed over 24 one-hour "buckets", i.e., a histogram. (For example, the 1100 MLT "bucket" means the time interval from 1100 MLT to 1159 MLT inclusive). This is also easily obtained from FREQUENCIES by specifying the necessary option.

A histogram depicting the results of this first subobjective appear in Fig. 9. Note the large clustering in the 0300 MLT sector (post-midnight); there is also a secondary peak appearing in the 2300 sector (pre-midnight).

Notice that from 0700 to 1400 MLT there is only one enhancement (0800). The results indicate that at least for the time period of this research, where all MLT's are being uniformly sampled, enhancements appear in the nighttime sectors, with a sharp dropoff at magnetic dawn and a sharp increase shortly before magnetic dusk.

Table 1. MLT Distribution Data

8	}	9 January	4	18	}	8 February	22	}	3 March
4			4	29 January	18	}	8 February	23	
5		17 January	4		2			23	3 March
5			4		2	8 February	23		
5			4		2		23	5 March	
5		17 January	4	29 January	3		23		
4			4		3	10 February	23		
4			4		3		23		
4			3		3	10 February	23	7 March	
4		19 January	3		3		23		
4			3	31 January	3		22		
4			3		2		22		
4			3		2		22	9 March	
4		19 January	4		2	12 February	22		
20			4		2		22		
20		19 January	4	31 January	2		22	9 March	
4			4		2		22		
4		21 January	4		1		23		
4			18		1		23		
6			18	31 January	1	16 February	23		
6			17	31 January	1		23		
6			3		1		23	9 March	
6		21 January	3	2 February	1		23		
6			3	2 February	1		23		
6			4		1		23		
5			4	2 February	1	18 February	23		
5		23 January	4		1		22		
5			3		1		22	11 March	
5			3	4 February	1		22		
5		23 January	3		1		22	13 March	
19			17		1	20 February	22		
19		23 January	17	4 February	1		21		
4	}	25 January	17		1	20 February	21	17 March	
5			18		1	22 February	21		
5			18		1	24 February	21	21 March	
5		25 January	18	4 February	1	24 February	21		
5			18		1	24 February			
5			3		0				
19	}	25 January	3	6 February	0	28 February			
3			3		0				
3		27 January	3	6 February	0	28 February			
4	}	27 January	18		0				
3			18	6 February	0				
3			2		0	3 March			
3			2	6 February	0				
3		27 January	2		0	3 March			
3			3		23	3 March			
3			3	8 February	23				
3			3		23				
3			3		23				
3			3		23	3 March			
3		29 January	3	8 February	23				
3			3		23, 23				

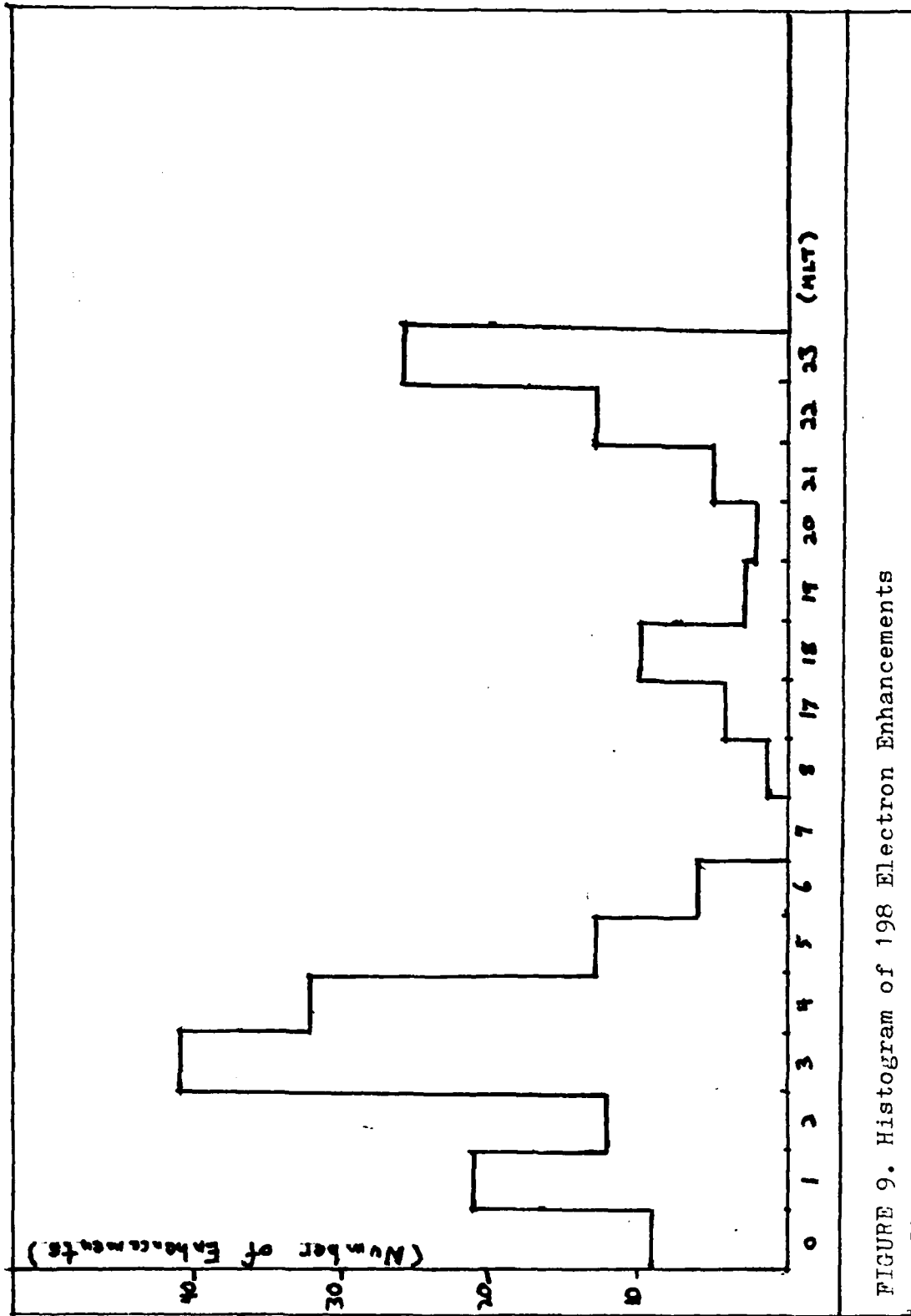


FIGURE 9. Histogram of 198 Electron Enhancements

V. Magnetometer Plots

The second subobjective of this research effort is to see if the appearance of an electron enhancement causes a change in the geomagnetic field (or, equivalently, is there an associated Birkeland current). Time did not permit analysis of all 198 enhancements, so seventeen passes consisting of 73 enhancements were selected for this aspect of the thesis. These particular passes were selected in such a way to get as even a contribution as possible from each month. The selected passes also had two or more enhancements; due to time limitations it was important to use as many as possible from the few passes available for analysis.

An example of a magnetometer plot appears in Fig. 10; what one would expect to see is a sharp change in the slope of the curve, which is the y-component (east-west) of the magnetic field plotted against time, that is coincident with an enhancement. The change in the B_y component is associated with a Birkeland (magnetic field-aligned) current by the following reasoning borrowed from Potemra, et al.

The Birkeland current \vec{J} produces a magnetic field in accordance with Ampere's law,

$$\vec{J} = (\mu_0)^{-1} [\text{curl } \vec{B}] \quad (22)$$

where $\mu_0 = 4\pi \times 10^{-7}$ henry/meter and \vec{B} is the geomagnetic field. Since magnetic disturbances associated with the

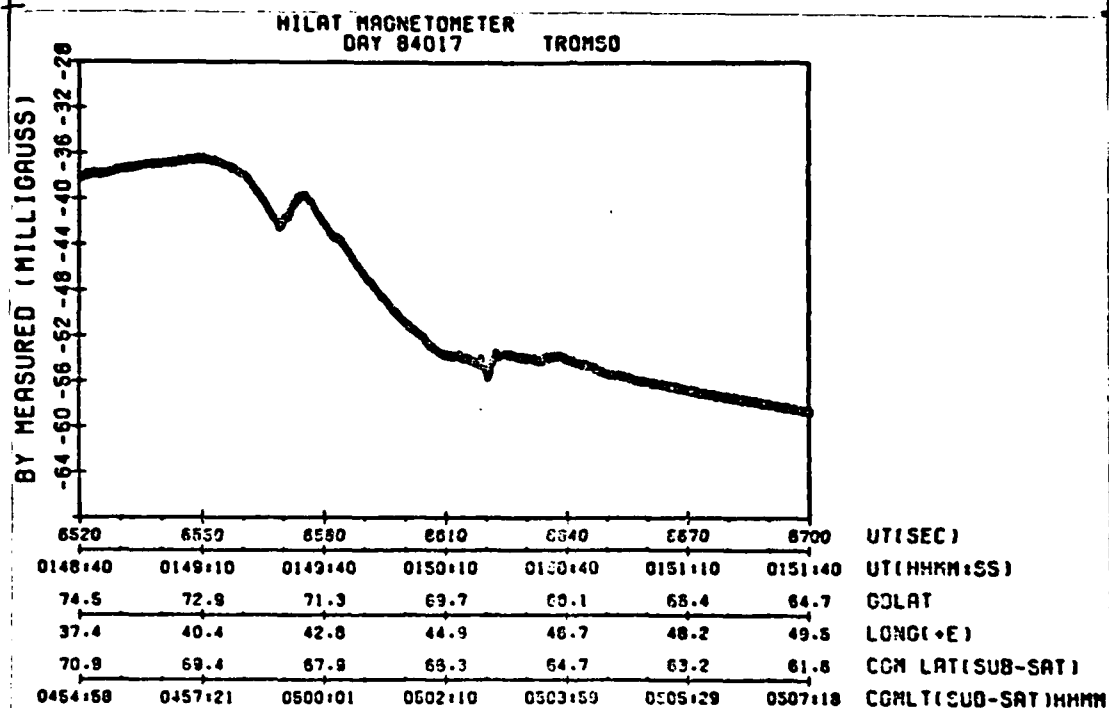


FIGURE 10. Magnetometer Plot: 6520sec-6700 sec U.T.
17 JANUARY 1964

Birkeland currents are in the B_y direction as previously stated, we have

$$J_z = J_{||} = (\mu_0)^{-1} [dB_y/dx] \quad (23)$$

where x is to the north, y to the east, and positive z is down toward the earth and parallel to the field lines.

Since μ_0 is known, and since the HILAT orbital velocity $dx/dt = 8$ km/sec, J can be written as

$$J_{||} = (\mu_0)^{-1} (dx/dt)^{-1} dB_y/dt \quad (24)$$

$$= 0.1 \text{ dB}_y/dt \text{ } \mu\text{A/square meter} \quad (25)$$

where dB_y/dt is in nanoteslas per second. The magnetometer plot shown has B_y in milligauss, which is easily convertible into nanoteslas, where one gauss equals 10^{-4} teslas (Potemra, 1984:121-122).

There is one problem that one must be aware of in working with HILAT magnetometer data; the spacecraft is oscillating slowly about its roll axis (less than a degree to either side), so it is difficult to tell if the slope of the line is a spacecraft-induced effect or if it is a genuine magnetic disturbance. Since we are looking for 'cutouts' in the curve that correspond to an enhancement occurrence, we measure the slope of the cutout with respect to the ambient slope. Fig. 10 shows an example of what we seek (Hardy, 1984:personal interview).

This data belongs to the same pass measured in the enhancement distribution section (17 January 1984, 1:43:47 to 1:53:45 U.T.). Notice the V-shaped structure (cutout) appearing between 6619 seconds and 6622 seconds. The third enhancement of this pass starts at 6616 seconds and lasts until approximately 6621 seconds. In this case the ambient slope is essentially zero (from 6610 to 6625 seconds), so after taking the slope of the negative, or left half of the V (which indicates a downward current, or upward flowing electrons; Potemra, 1984:124), we get a current density of $13.3\mu\text{A}/\text{square meter}$. The right half of the V is essentially the mirror image of the left half; the current density has the same magnitude but opposite direction (upward current, downward flowing electrons; Potemra, 1984:124).

In the example pass given, the first two enhancements have no corresponding disturbance. We would then like to see how many enhancements are associated with magnetic disturbances, and, if possible, is enhancement size proportional to the size of the disturbance.

Of the 73 enhancements studied in this particular subobjective, only nine had corresponding changes in B_y with respect to time (dB_y/dt). The results appear in Table 2; here "Time" is the beginning time of the enhancement, and "Time Duration" is the measured duration. There appears to be some credence to a possible relationship between the peak number flux of the low-energy electrons and the current density J_u .

Table 2. Magnetometer Results

Site (T/S)	Date	Time(U.T.) (HH:MM:SS)	Time Duration (sec)	PEAK	dB_y/dt (nT/sec)	J (A/m^2)
T	17-1	01:50:16	5	58.4	133	13.3
T	19-1	17:38:24	4	1.97	16.7	1.67
T	21-1	01:46:12	3	1.75	20.0	2.00
S	23-1	06:0026	3	14.8	12.9	1.29
T	25-1	20:04:34	2	38.8	100	10.0
T	9-3	21:30:53	5	46.2	68.2	6.82
T	9-3	21:31:47	3	3.6	16.7	1.67
T	9-3	21:31:55	2	9.0	32.5	3.25
T	9-3	21:32:20	4	4.4	5.3	0.53

(Date is in "Day-Month" format, and PEAK is in units of $10^8/cm^2$ -sec-ster)

T = Tromso

S = Sondre

However, with such limited statistics, any attempted linear regression would yield results of dubious value. The nine points appear in Fig. 11, which is a plot of PEAK versus J_{μ} .

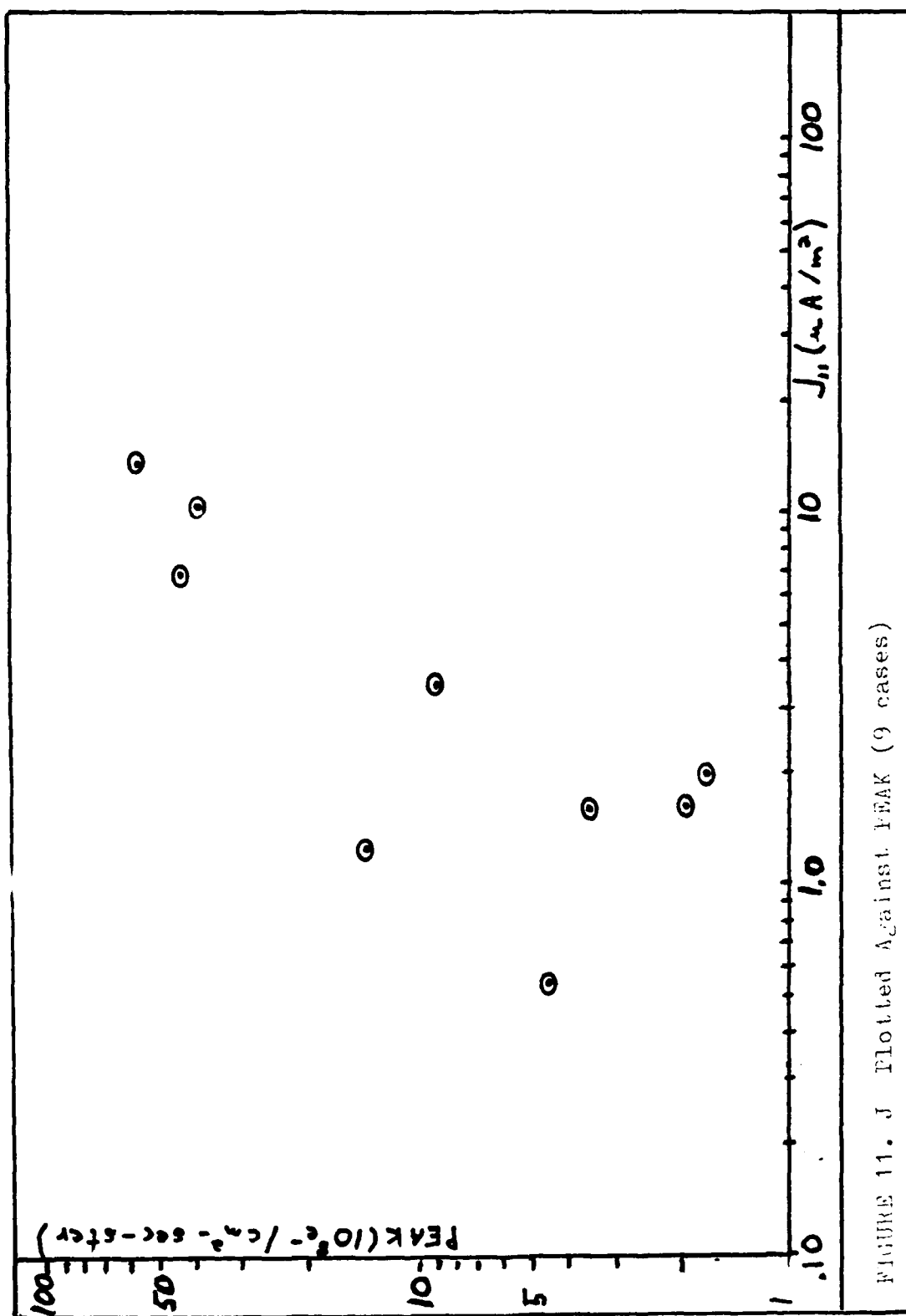


FIGURE 11. J Plotted Against PEAK (9 cases)

VI. Graphical Distribution of Peak Intensities and Descriptive Statistics

In this third subobjective, we are interested in measuring the peak number flux (JTOT) of the enhancements, and then studying how these peak values are distributed along with some descriptive statistics.

For this subobjective, the same seventeen passes with their 73 enhancements were used. Enlarged J-sensor plots were used to measure the peak intensities (Fig. 12).

Again, the SPSS program FREQUENCIES was used to obtain a histogram and the following descriptive statistics: mean, variance, standard error, standard deviation, minimum value, maximum value, and range.

In Fig. 13 we have a histogram representing the distribution of peak number flux intensities. The average value of PEAK as determined by FREQUENCIES is 9.7×10^8 electrons/cm²-sec-ster, with a standard deviation of 9.6×10^8 electrons/cm²-sec-ster. The outliers (enhancements with PEAK values greater than 2×10^9 electrons/cm²-sec-ster) are the same enhancements that are associated with the larger magnetic disturbances mentioned in the previous chapter. Fig. 13 also presents some additional descriptive statistics as determined by FREQUENCIES.

MODE = 3 1984 DAY 17 KP = 0

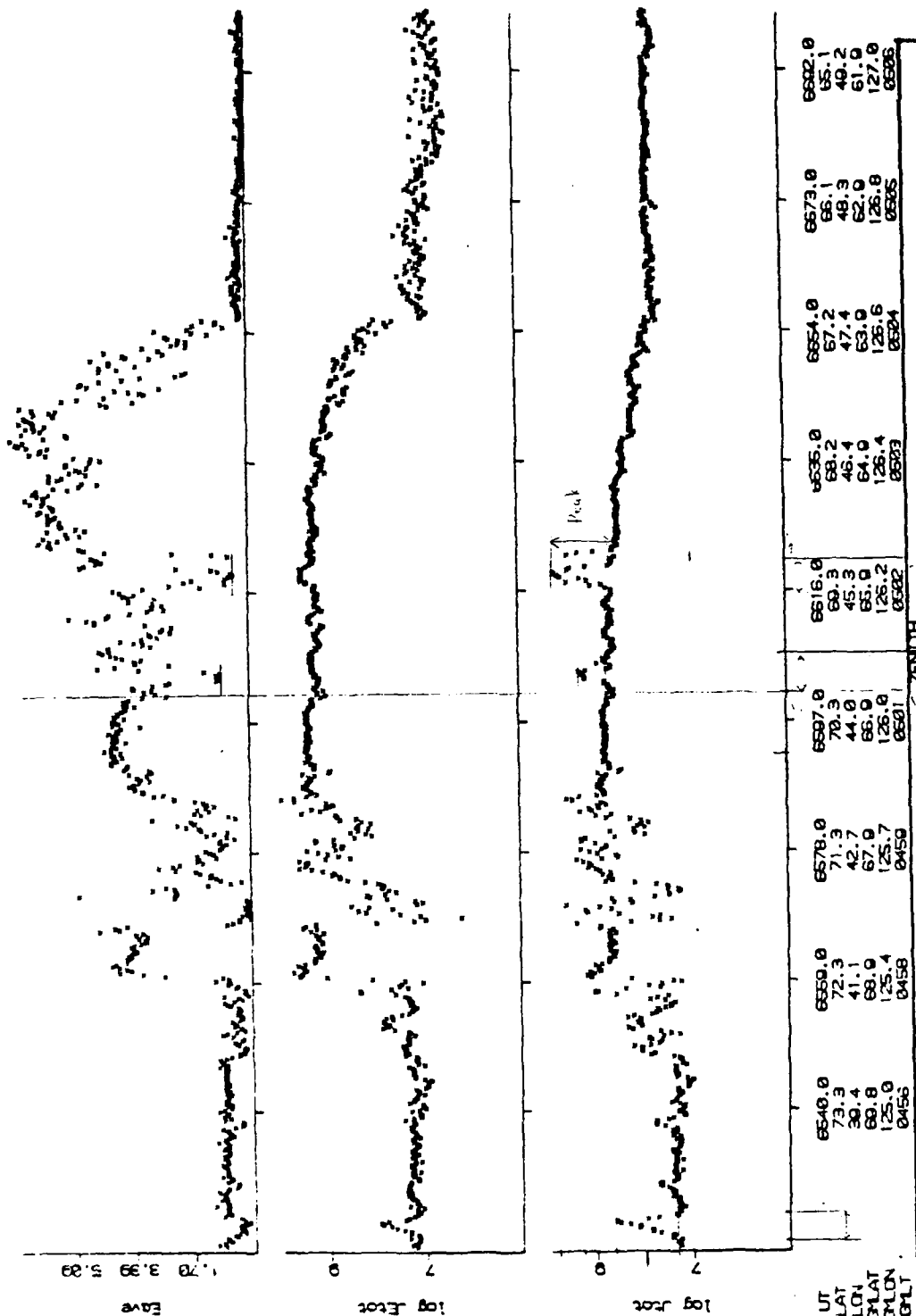
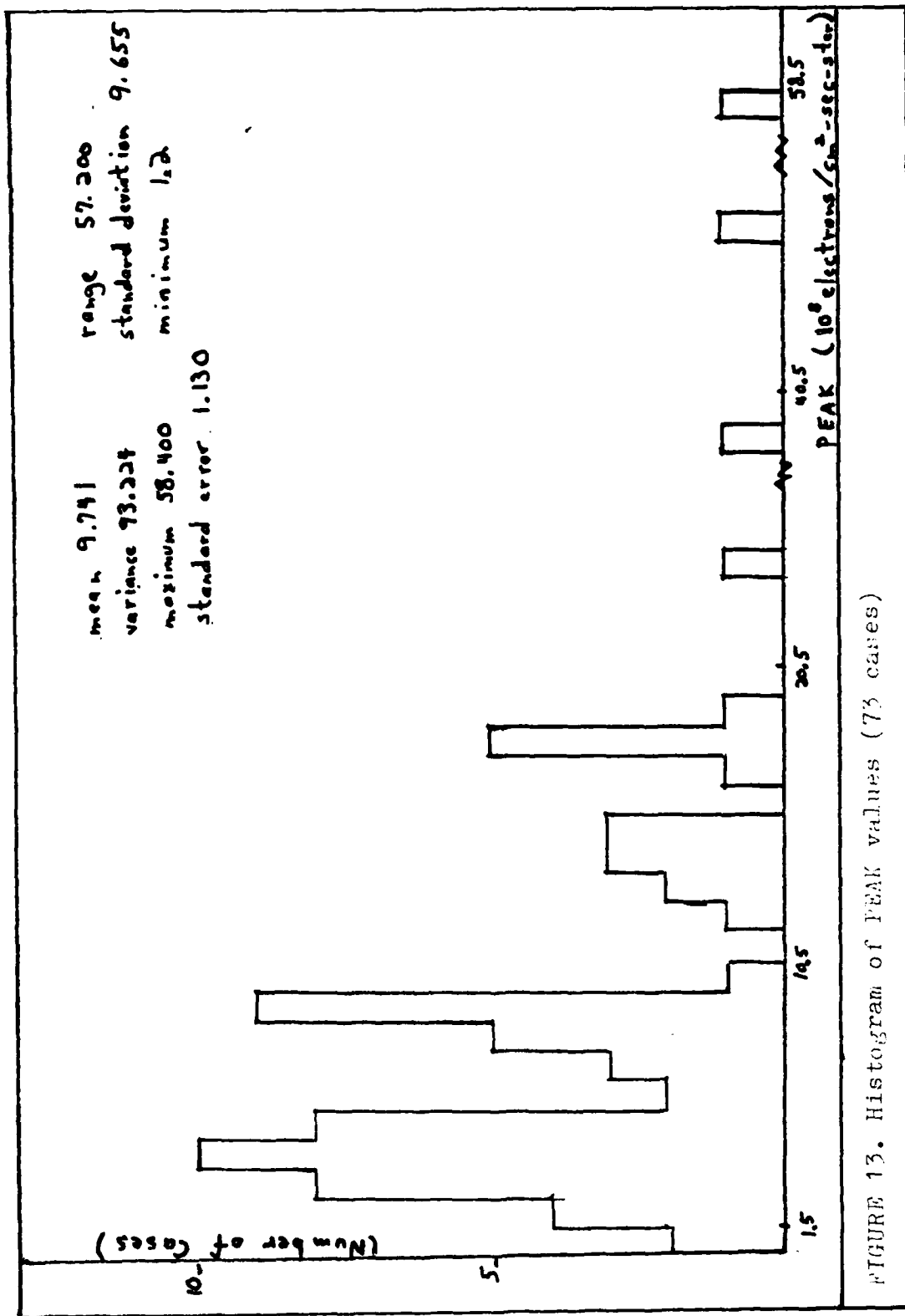


FIGURE 12. Expanded J-Sensor Plot: 6520 sec-6700 sec U.T. 17 Jan. 1984



VII. Discriminant Analysis of Electron Enhancements and Their Relationship to Scintillations

The fourth and last subobjective is an attempt to understand the relationship between electron enhancement occurrence and radio scintillations (amplitude and phase). This is the primary objective of the thesis, and there are many subtleties that one must understand in order to interpret the results.

The following procedures must be used if one wishes to correlate enhancements with scintillations. Recall that the HILAT vehicle is measuring electrons in situ at 800 km, but the scintillation producing irregularities are down in the F region at 350 km. Consequently, enhancements must be spatially, not temporally correlated with their respective scintillation values (S4 and PRMS, with the two frequencies of interest being 137 MHz and 413 MHz).

Using the 17 January pass again as an example, and using the second enhancement, the method for determining the corresponding S4 and PRMS values is as follows. An enlarged J-sensor plot shows the second enhancement starting at 1:50:01 U.T. (Fig. 12). One then tries to find the closest corresponding time on the satellite location printout (Table 3A) which in this case is 1:49:54. This printout gives the satellite's geographic subpoint at this time, which is 70.5 degrees north latitude and 43.9 degrees east longitude. The station at Tromso is at 69.7 degrees north latitude and 18.9 degrees

TABLE 3-A. Satellite Location Printout

	UT	SATELLITE					FLD 350 KM		
		SLAT	SLON	ILAT	ALT	DIP	DECL	FLAT	FLON
1	14354	81.3	314.4	84.3	3.29	85.5	-53.2	81.5	312.8
2	14409	81.6	319.9	83.7	3.67	85.3	-49.6	81.8	318.2
3	14424	81.9	325.9	83.0	3.98	85.1	-45.4	82.1	324.2
4	14439	82.0	332.1	82.3	0.23	84.9	-40.9	82.3	330.5
5	14454	82.1	338.4	81.6	4.44	84.6	-36.0	82.4	336.9
6	14509	82.0	344.8	80.8	4.82	84.4	-31.1	82.3	343.4
7	14524	81.9	351.1	80.1	4.77	84.2	-26.1	82.2	349.9
8	14539	81.6	357.0	79.3	4.89	83.9	-21.5	82.0	356.0
9	14554	81.3	002.5	78.5	5.00	83.7	-17.1	81.7	001.7
10	14609	80.9	007.6	77.7	5.10	83.4	-13.2	81.3	007.0
11	14624	80.4	012.2	76.9	5.18	83.2	-09.6	80.9	011.8
12	14639	79.9	016.4	76.1	5.26	82.9	-06.5	80.4	016.1
13	14654	79.3	020.1	75.3	5.32	82.7	-03.8	79.8	020.0
14	14709	78.7	023.5	74.4	5.38	82.4	-01.4	79.2	023.6
15	14742	78.1	026.4	73.6	5.44	82.1	00.6	-8.6	026.5
16	14739	77.4	029.1	72.8	5.43	81.8	02.3	77.9	029.3
17	14754	76.7	031.5	72.0	5.53	81.5	03.8	77.3	031.7
18	14809	76.0	033.6	71.1	5.57	81.2	05.0	76.5	033.9
19	14824	75.2	035.6	70.3	5.60	80.9	06.0	75.8	035.9
20	14839	74.5	037.3	69.5	5.64	80.6	06.9	-5.1	037.7
21	14854	73.7	038.9	68.7	5.67	80.3	07.6	74.3	039.2
22	14909	72.9	040.3	67.8	5.70	80.0	08.1	73.6	040.7
23	14924	72.1	041.6	67.0	5.72	79.6	08.6	72.8	042.0
24	14939	71.4	042.8	66.2	5.75	79.3	08.9	72.0	043.2
25	14954	70.5	043.9	65.3	5.77	78.9	09.2	71.3	044.3
26	15009	69.7	044.9	64.5	5.79	78.5	09.3	70.5	045.3
27	15024	68.9	045.8	63.7	5.81	78.1	09.5	69.7	046.2
28	15039	68.1	046.7	62.8	5.83	77.8	09.5	68.9	047.1

east longitude, so at this time the satellite is east of the station.

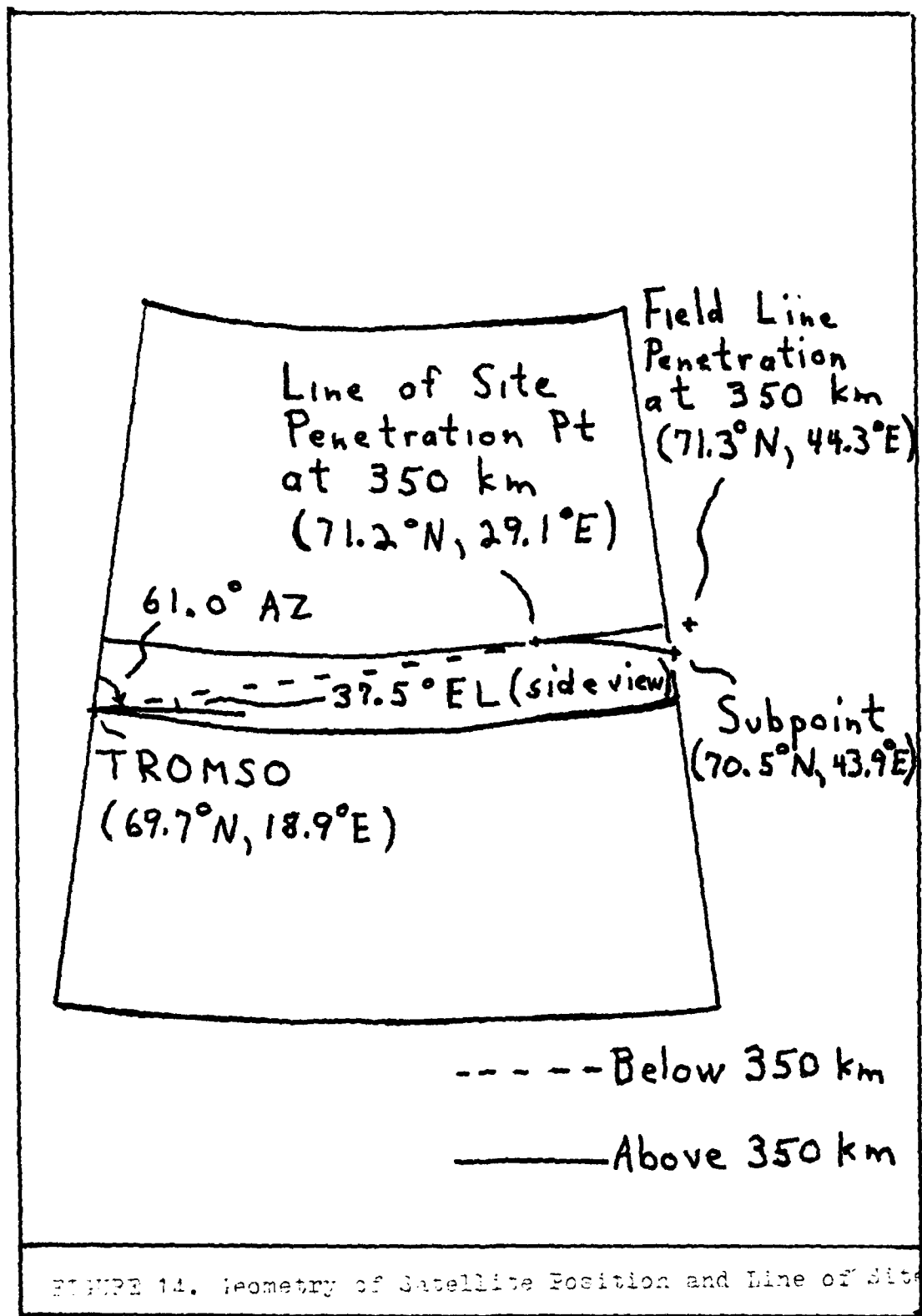
As we are investigating the null hypothesis that enhancements cause scintillations, the low-energy electrons must somehow travel down to the F region at 350 km. Obviously they would have to spiral about the magnetic field lines; consequently, we need to find the latitude where the field lines intersect 350 km. This value appears under the column headed FLAT (Table 3A), which is in turn under the heading FLD 350 KM. For this example, FLAT is at 71.3 degrees latitude.

We then look under the PLAT (penetration latitude) column of the scintillation data printout, Table 3B, to find 71.3 degrees; 71.2 (line 27) is what will be used. This penetration latitude is also the latitude at which the line of sight of the radio beacon penetrates 350 km. Note the two columns preceding this value along line 27 are values of the topocentric elevation and azimuth of the 350 km penetration point. For this example, the penetration point is at 37.5 degrees elevation and 61.0 degrees azimuth. (See Fig. 14). Note that we are assuming that electron enhancements are both at the same latitude as the irregularity but that they span several degrees of longitude.

According to Basu and Eileen MacKenzie, any penetration point with elevations less than 20 degrees are suspect and hence corresponding scintillation values should not be used.

TABLE 3-B. Scintillation Data Printout

	'EL	AZ	PLAT	PLON	S4	PRMS	S4	PRMS
1	14354	11.0	-25.8	78.2	-3.8	0.00	0.00	0.0
2	14409	12.2	-24.5	78.6	-1.9	.44	.39	.5
3	14424	13.5	-23.1	77.7	1.7	.52	.42	1.3
4	14439	14.9	-21.6	77.4	4.2	.40	.38	.9
5	14454	16.3	-20.0	77.1	6.4	.35	.16	1.6
6	14509	17.8	-18.2	76.7	8.5	.31	.17	.6
7	14524	19.4	-16.3	76.4	10.4	.28	.21	.4
8	14539	21.1	-14.1	76.1	12.2	.29	.21	.7
9	14554	22.8	-11.7	75.7	13.8	.32	.17	.3
10	14609	24.6	-9.0	75.4	15.3	.29	.18	1.0
11	14624	26.4	-5.9	75.1	16.8	.19	.16	1.0
12	14639	28.3	-2.5	74.3	18.1	.22	.16	.9
13	14654	30.2	1.3	74.4	19.3	.26	.16	8.3
14	14709	32.0	5.6	74.1	20.5	.29	.10	0.2
15	14724	33.8	10.3	73.8	21.6	.23	.12	2.5
16	14739	35.5	15.6	73.5	22.7	.23	.11	2.1
17	14754	36.9	21.3	73.1	23.7	.22	.18	1.5
18	14809	38.0	27.6	72.8	24.7	.26	.15	1.0
19	14824	38.8	34.2	72.5	25.6	.22	.12	1.7
20	14839	39.1	41.0	72.2	26.5	.23	.11	1.4
21	14854	39.0	47.8	71.9	27.4	.20	.09	1.6
22	14909	38.4	54.6	71.5	28.2	.25	.11	1.5
23	14924	37.5	61.0	71.2	29.1	.28	.11	1.6
24	14939	36.2	66.9	70.9	29.9	.35	.12	1.1
25	14954	34.7	72.4	70.5	30.7	.37	.14	2.0
26	15009	33.0	77.4	70.2	31.5	.34	.17	1.6
27	15024	31.2	81.9	69.8	32.3	.29	.15	1.6
28	15039	29.4	85.8	69.5	33.0	.32	.18	1.5



It would be prudent also at this point to say that Dr. Basu was the originator of this procedure.

At this point, we can now read off the S4 and PRMS values for the two frequencies of interest, which are 0.28 and 5.5 respectively for 137 MHz, and 0.11 and 1.6 for 413 MHz. The S4 values are unitless and the PRMS values are in radians. Note that the time of 1:49:24 appears in the first column (U.T.) as the time of the previously mentioned scintillation values. Due to an error in formatting the data, one must add 7.5 seconds to this time to get the actual time of these scintillation values.

On Table 3C we must perform another check on the reliability of the data by looking at the parameter LZEN, or the zenith angle. This particular zenith angle is the angle between the radio propagation direction and the magnetic field line. Typically, any angle less than approximately 10 degrees will result in a geometric enhancement, i.e., since the irregularities are aligned along the field lines, the propagation path is entering edge on and large scintillation can result because of the geometry. Again, for this example, we cross-index our PLAT value (71.2 degrees) with the LZEN value, which is 27.1 degrees.

The resulting S4 and PRMS values are evaluated with respect to values that precede and follow them, as we are interested in seeing if a rise in low-energy electron number flux gives a corresponding increase in S4 and PRMS. This is

TABLE 3-C. F-Region Penetration Data

UT	F REGION PENETRATION (350 KM)									
	PLAT	PLON	PALT	PINV	PMLT	PDIP	PDECL	LZEN		
1	14354	78.2	-3.8	350.	76.5	4.03	82.0	-16.7	57.2	
2	14409	78.2	-1.0	350.	75.9	4.12	81.8	-14.3	58.6	
3	14424	77.7	1.7	350.	75.4	4.20	81.6	-12.2	59.9	
4	14439	77.4	4.2	350.	74.8	4.27	81.5	-10.3	61.2	
5	14454	77.1	6.4	350.	74.3	4.34	81.3	-8.5	62.5	
6	14509	76.7	8.5	350.	73.8	4.40	81.1	-6.9	63.7	
7	14524	76.4	10.4	350.	73.3	4.46	81.0	-5.4	64.8	
8	14539	76.1	12.2	350.	72.8	4.51	80.8	-4.1	65.8	
9	14554	75.7	13.8	350.	72.3	4.55	80.6	-2.9	66.5	
10	14609	75.4	15.3	350.	71.9	4.60	80.5	-1.8	66.8	
11	14624	75.1	16.8	350.	71.4	4.64	80.3	-0.8	66.8	
12	14639	74.8	18.1	350.	71.0	4.68	80.2	0.2	66.2	
13	14654	74.4	19.3	350.	70.6	4.71	80.0	1.0	65.0	
14	14709	74.1	20.5	350.	70.1	4.75	79.9	1.8	63.1	
15	14724	73.8	21.6	350.	69.7	4.78	79.8	2.5	60.7	
16	14739	73.5	22.7	350.	69.3	4.81	79.6	3.2	57.7	
17	14754	73.1	23.7	350.	68.9	4.84	79.5	3.8	54.1	
18	14809	72.8	24.7	350.	68.5	4.87	79.4	4.4	50.1	
19	14824	72.5	25.6	350.	68.1	4.90	79.2	4.9	45.8	
20	14839	72.2	26.5	350.	67.7	4.93	79.1	5.4	41.2	
21	14854	71.9	27.4	350.	67.3	4.96	78.9	5.9	36.5	
22	14909	71.5	28.2	350.	66.9	4.99	78.8	6.3	31.8	
23	14924	71.2	29.1	350.	66.5	5.01	78.7	6.7	27.1	
24	14939	70.9	29.9	350.	66.1	5.04	78.5	7.1	22.5	
25	14954	70.5	30.7	350.	65.7	5.07	78.4	7.5	18.2	
26	15009	70.2	31.5	350.	65.3	5.09	78.2	7.8	13.9	
27	15024	69.8	32.3	350.	64.9	5.12	78.1	8.2	10.0	
28	15039	69.5	33.0	350.	64.5	5.15	77.9	8.5	6.3	

similar to the study of enhancements and the accompanying changes in magnetic field. Consequently, we are interested in the rise of S4 and PRMS above background scintillation values. Figs. 15 and 16 are plots of the S4 and PRMS values for both frequencies of this pass, with the two scintillation cases of interest marked as 1 and 2. There are three enhancements appearing in this pass; however, the LZEN value corresponding with the third one is 10 degrees and hence was not used in this analysis.

For the purposes of this research, we assume that the observed enhancements are long-lived (on the order of 10 minutes) and they are not moving. This appears to be a reasonable assumption, according to Dr. Hardy (private communication).

One should also expect that the observation time of an enhancement should precede that of the observed scintillation in order to be consistent with our "cause and effect" hypothesis. However, approximately half of the cases of interest exhibited the exact opposite order, i.e., the scintillation came before the enhancement. This is easily interpreted as follows. The satellite's radio beacon has penetrated the distorting region at 350 km before it has encountered the enhancement (the source of the irregularity) at the satellite's orbital altitude of 800 km. Further, it is assumed that the electron enhancement has been going for some time (at the point in space of the satellite encounter) before the actual

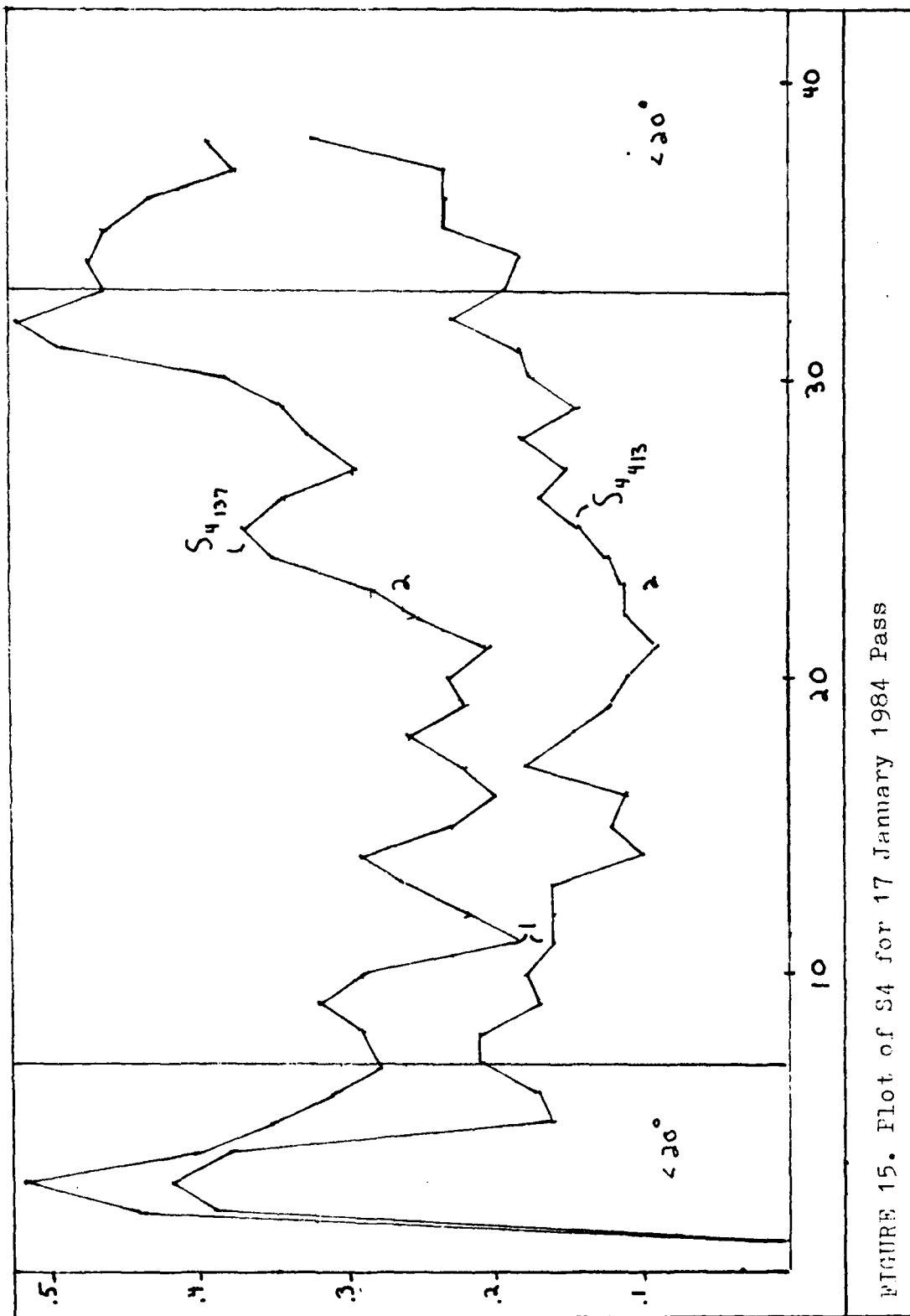
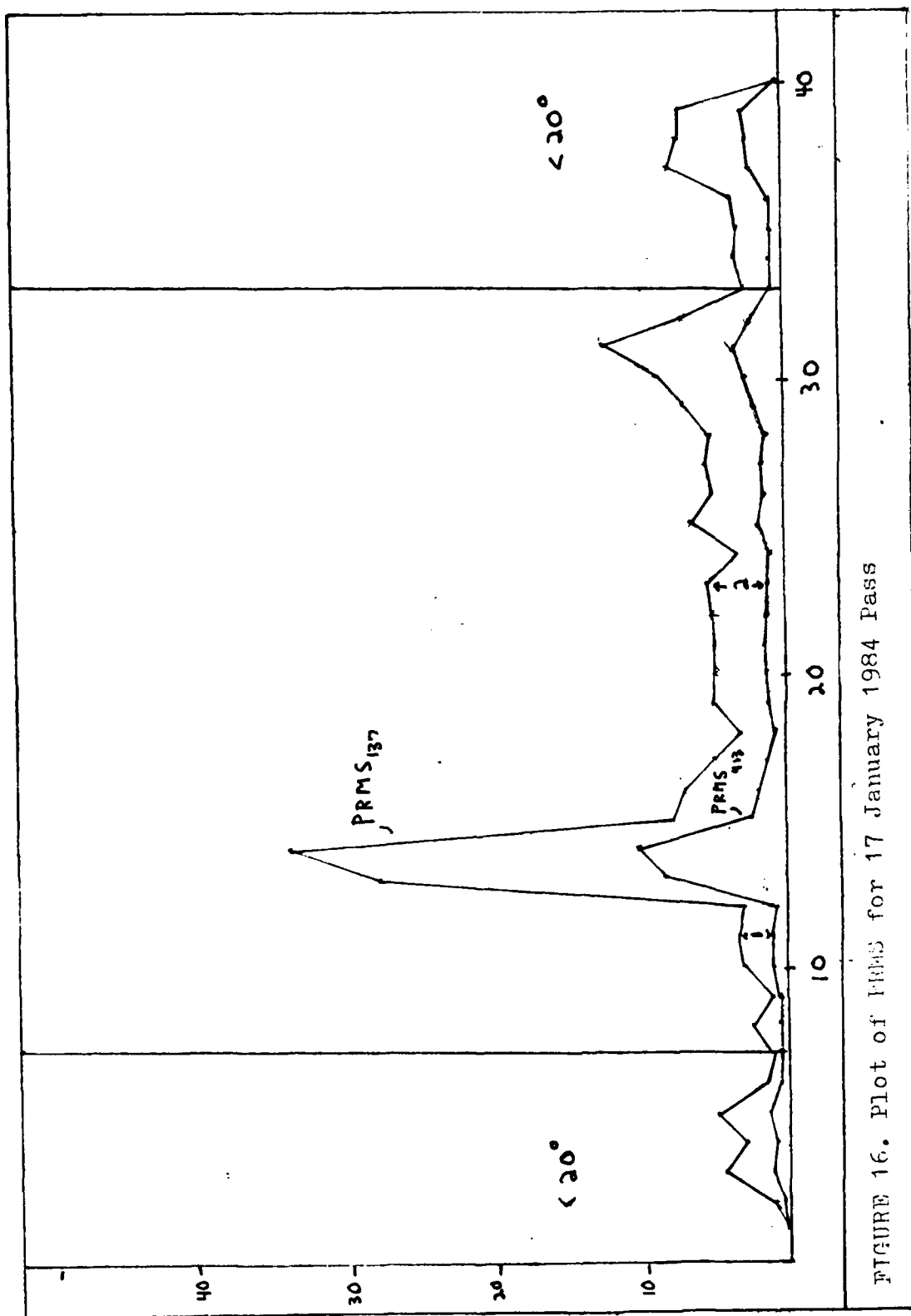


FIGURE 15. Plot of S4 for 17 January 1984 Pass

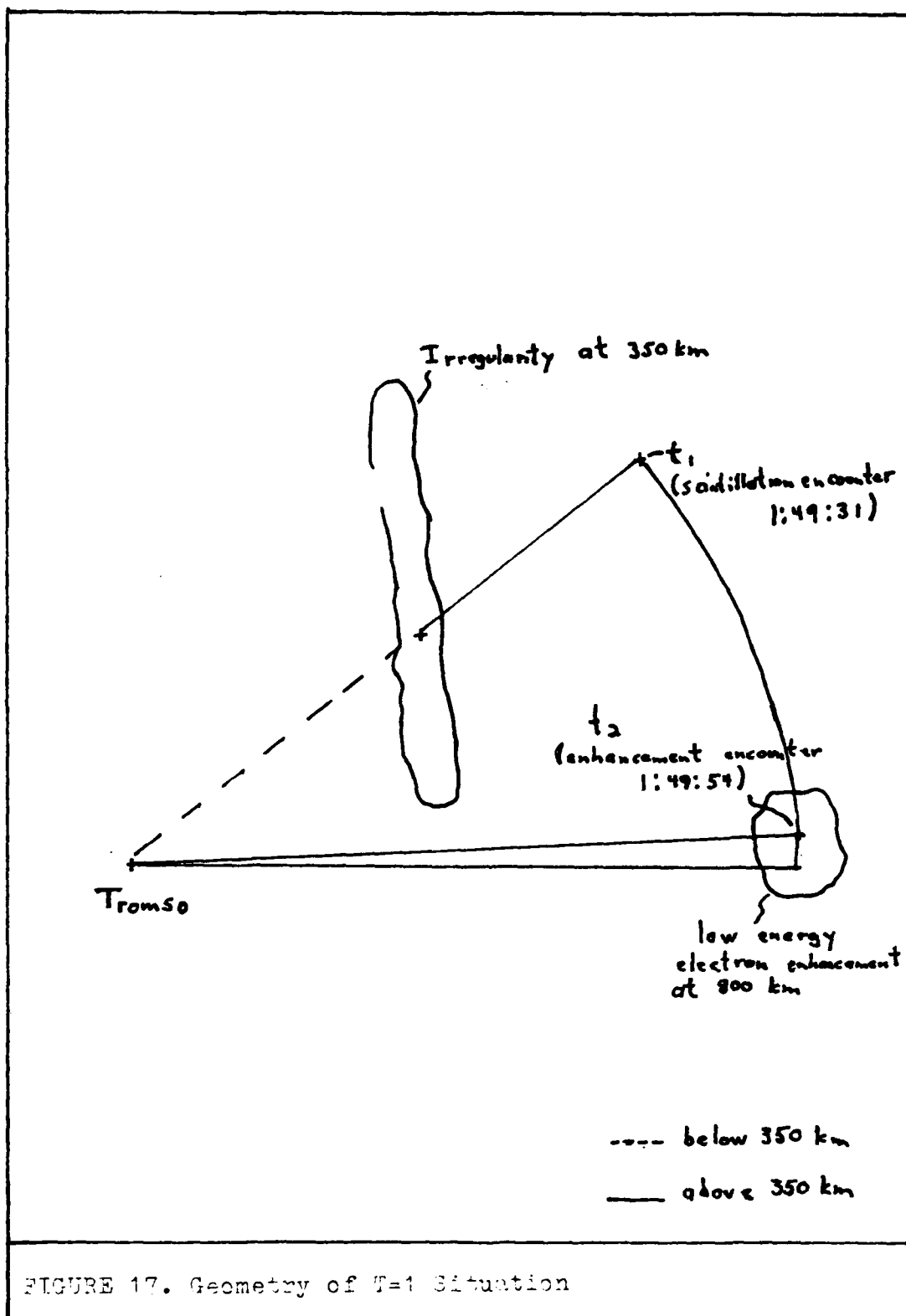


satellite encounter. In Fig. 17 this situation is pictured for the second enhancement of the 17 January pass.

There should (we emphasize should) be no difference between cases where either the scintillation time comes before or after the time of enhancement; however, as a precaution, a "flag" known as "T" has been assigned in every case. The variable T is either "0" or "1"; if "1", the scintillation is observed before the electron enhancement. If T is zero, the opposite situation exists.

Note also the difference in time between the scintillation and the enhancement; in our example the time between events is 23 seconds. We would expect that for a small time difference we would best be able to determine whether the enhancement's presence at 800 km affects irregularity development at 350 km. Therefore, another variable to be included in the analysis is DT, the difference in time between the two events in seconds.

As was previously discussed, we anticipate that for a rise in electron number flux a commensurate rise in S4 and PRMS should result. If a noticeable rise is evident in S4 and PRMS, we consider that a "hit", and use the variable "H" where it is "1" if it is a "hit". A "miss" (no noticeable increase) has an H value of "0". This particular task is somewhat easier said than done, however, for the following reason. Each scintillation data point is an average value over 15 seconds; the satellite traverses an enhancement in considerably less time (on the order of three seconds). Consequently, any



small amplitude or short time duration variation in S4 and PRMS is mostly "buried" in the averaging process. (The situation is analogous to photographic resolution; physical features smaller than the camera's resolution will not be easily detected unless very bright).

The data format is shown in Table 4, where we have a total of 42 enhancements with their associated scintillation values. Some enhancements here were not the same ones used in the previous subobjectives (2-4), as it was discovered that for a few passes the corresponding scintillations were either unreliable (low elevation and/or low LZEN) or defective. The key below the figure explains the variable names used.

The remaining portion of this chapter will be devoted to explaining discriminant analysis and the results obtained by using this technique. Basically, discriminant analysis is a method that allows one to statistically distinguish between two or more groups of cases. In this research, we will look at groups of scintillations based on their increase in S4 and PRMS (three groups; low, medium, high).

In order to distinguish between the groups, a collection of discriminating variables that measures characteristics on which the groups may differ must be selected (Klecka et al., 1975:435). Since we hypothesize that electron enhancements may cause scintillations, we have four variables that characterize electron enhancement characteristics. They are the peak electron number flux (PEAK), the time duration (TIME),

TABLE 4-A. Data Used in Discriminant Analysis

4.4	4.1	9.1	0.18	0.19	0.16	3.6	1.0
13.8	5.4	74.5	0.72	0.28	0.11	5.5	1.6
8.1	1.8	7.3	0.18	0.23	0.26	4.9	1.5
6.9	1.3	9.0	0.18	0.15	0.14	1.9	0.6
2.9	3.0	5.7	0.48	0.12	0.08	1.0	0.4
2.0	2.6	3.4	1.26	0.16	0.12	0.7	0.3
1.7	2.8	5.0	0.14	0.24	0.13	1.7	0.5
3.2	3.8	8.6	0.54	0.25	0.13	26.9	8.4
9.5	3.1	21.6	0.27	0.18	0.16	1.3	0.4
5.8	1.6	4.7	0.02	0.27	0.14	1.2	0.8
2.9	1.8	5.3	0.22	0.27	0.13	2.2	0.6
8.1	1.6	13.0	0.02	0.24	0.12	1.8	0.6
2.9	2.1	3.1	0.22	0.39	0.17	8.0	2.3
14.5	1.4	20.3	0.06	0.26	0.21	1.6	0.5
14.5	2.7	39.1	0.08	0.26	0.22	5.2	1.6
9.0	2.0	18.0	0.25	0.19	0.26	2.0	0.9
18.3	10.9	199.0	0.15	0.16	0.18	2.7	0.9
18.3	4.8	87.8	0.40	0.17	0.13	2.9	0.9
4.8	2.7	12.9	0.70	0.23	0.08	2.4	0.7
6.6	1.1	7.3	0.35	0.12	0.13	1.7	0.5
17.7	3.3	38.7	0.18	0.12	0.13	1.2	0.4
7.8	4.2	26.0	0.45	0.13	0.09	1.8	0.5
5.5	5.3	18.2	0.25	0.25	0.07	2.1	0.6
5.5	4.4	26.6	0.20	0.12	0.14	0.9	0.3
11.9	5.4	32.1	0.20	0.27	0.10	0.9	0.3
3.1	2.7	4.2	0.40	0.16	0.12	1.6	0.5
5.2	2.0	5.2	0.21	0.22	0.10	2.4	0.7
5.4	2.7	7.3	0.18	0.17	0.06	1.7	0.5
5.4	9.5	51.4	0.36	0.14	0.16	1.8	0.6
9.6	2.7	13.0	0.38	0.14	0.37	1.7	0.3
9.0	5.1	22.5	0.28	0.16	0.13	3.6	1.1
12.6	7.8	59.2	0.26	0.13	0.13	4.5	1.4
12.6	4.9	61.7	0.26	0.17	0.08	5.2	1.6
3.6	2.4	8.7	1.03	0.32	0.15	2.1	2.3
2.4	6.3	15.2	1.94	0.31	0.13	4.4	1.3
15.3	5.4	41.3	0.03	0.30	0.23	4.5	1.3
2.7	4.1	11.2	0.15	0.50	0.11	4.3	1.2
9.0	2.0	16.0	0.60	0.38	0.12	2.3	0.6
4.4	3.4	4.4	0.35	0.11	0.13	3.9	1.1
4.4	6.8	7.5	0.50	0.14	0.17	3.2	1.0
4.4	5.4	23.3	0.15	0.27	0.13	1.6	0.5
4.4	1.4	3.1	0.21	0.35	0.18	2.4	0.6

PEAK TIME: PDMT LMS SI SI PI PA
 PEAK ($10^5/\text{cm}^2 - \text{sec} - \text{atom}$) SI (0.137 MHz)
 TIME (seconds) SI (0.137 MHz)
 PTIME ($10^5/\text{cm}^2 - \text{atom}$) SI (0.137 MHz) rations
 SI (0.137 MHz)

TABLE 4-B. Data Used in Discriminant Analysis (cont.)

1	0	3	128	0.00	0.06	2.6	0.7
1	0	3	23	0.08	0.02	2.0	0.6
1	1	3	113	0.08	0.13	4.1	1.1
1	0	1	105	0.00	0.03	1.1	0.2
0	0	1	37	0.04	0.01	0.3	0.1
0	0	1	52	0.08	0.05	0.0	0.0
1	0	1	128	0.06	0.02	0.9	0.1
1	1	3	105	0.07	0.02	25.9	8.0
1	0	1	90	0.00	0.05	0.0	0.0
1	0	1	180	0.06	0.03	0.0	0.2
1	0	1	158	0.06	0.02	1.0	0.0
1	0	2	98	0.03	0.01	0.6	0.0
1	1	3	45	0.15	0.06	6.0	1.9
1	0	1	75	0.12	0.00	0.0	0.1
1	1	3	68	0.14	0.01	3.6	1.2
1	0	2	60	0.03	0.12	0.4	0.5
1	0	2	67	0.00	0.10	1.1	0.5
1	1	2	23	0.01	0.04	1.3	0.5
1	0	2	8	0.07	0.09	0.3	0.3
1	0	2	38	0.02	0.04	0.9	0.3
1	0	1	30	0.02	0.04	0.6	0.2
1	0	2	23	0.03	0.00	1.2	0.3
1	1	2	8	0.14	0.00	1.6	0.5
0	0	1	7	0.01	0.04	0.4	0.2
0	1	2	7	0.17	0.04	0.3	0.0
0	0	3	22	0.08	0.06	0.7	0.2
0	1	2	29	0.04	0.04	1.5	0.4
0	0	1	7	0.04	0.00	0.1	0.3
0	0	2	67	0.02	0.08	0.9	0.4
0	0	2	75	0.02	0.29	0.8	0.1
1	0	3	53	0.03	0.05	1.9	0.6
1	0	3	48	0.00	0.05	2.9	0.9
1	0	2	23	0.04	0.00	3.6	1.1
0	1	3	52	0.20	0.07	5.1	1.4
1	1	3	38	0.11	0.03	2.6	0.9
1	1	3	15	0.27	0.11	1.4	0.4
1	0	3	57	0.20	0.00	2.0	0.6
0	0	1	40	0.08	0.01	0.0	0.0
0	0	2	52	0.01	0.01	1.6	0.5
0	1	3	67	0.14	0.00	1.6	0.4
0	0	1	67	0.04	0.04	0.0	0.0
0	0	2	50	0.12	0.07	0.2	0.1

T H 3 DT DS1 DS2 DS3 DS4

T (0 or 1) DS1 (0 or 1) DS2 (0 or 1) DS3 (0 or 1) DS4 (0 or 1)

H (0 or 1) DS1 (0 or 1) DS2 (0 or 1) DS3 (0 or 1) DS4 (0 or 1)

DT (0 or 1) DS1 (0 or 1) DS2 (0 or 1) DS3 (0 or 1) DS4 (0 or 1)

DS1 (0 or 1) DS2 (0 or 1) DS3 (0 or 1) DS4 (0 or 1)

the time integrated number flux (PTIME), and the minimum average electron energy (EAVG). These, plus DT, give a total of five discriminating variables.

The discriminating aspect is accomplished by weighting and then linearly combining the discriminating variables in order to make the groups as distinct as possible. These "discriminant functions" are of the form

$$D_i = d_{i1}Z_1 + d_{i2}Z_2 + \dots + d_{ip}Z_p \quad (26)$$

where D_i is the score of the discriminant function i , the d 's are the weighting coefficients, and the Z 's are the standardized values of the p discriminating variables. The maximum number of derivable functions is either one less than the number of groups or equal to the number of discriminating variables, whichever is smaller. The main idea is to form the functions so that the maximum separation of the groups results. Once obtained, the discriminant functions allow one to both analyze and classify (Klecka et al., 1975:435).

The analysis aspect allows one to determine via available statistical tests how well the discriminating variables differentiate between groups when used in the discriminant functions. One can think of discriminant functions as axes in Euclidean space; the greater the group separation along each axis, the greater the discrimination. In fact, the weighting coefficients can be interpreted as measures of how well a

particular discriminating variable contributes to the differentiation (Klecka et al., 1975:436).

The classification aspect arises after the discriminating functions have been computed. After the necessary discrimination variables have been determined for cases with known group membership, classification functions can be calculated which will allow future classification of cases of unknown membership. The equation for a particular group would appear as

$$C_i = c_{i1}V_1 + c_{i2}V_2 + \dots + c_{ip}V_p + c_{i0} \quad (27)$$

where C_i is the classification score for group i , the c 's are the classification coefficients, and the V 's are the variable values of the discriminating variables (Klecka et al., 1975: 436,445).

Under the assumption of a multivariate normal distribution, classification scores can be used to determine probabilities of group membership. In other words, by assigning a case to the group with the highest value of C_i , we are saying that this case has the greatest probability of being in group i (Klecka et al., 1975:445).

The value of the classification functions are to tell us how effective the discriminating variables are. If there is a great number of misclassifications, then more reliable discriminating variables need to be found. The routine used in this research allows for a display for each case of the discriminating score and the predicted group membership. The

largest probability is given, followed by the next highest probability if larger than 0.0005. Another probability given is the probability that a member of the predicted group would be as far from the group centroid (the mean value of a discriminating variable averaged over all groups) as the case under consideration; this probability is represented as $P(X/G)$ (Klecka et al., 1975:446).

Two methods were used to determine the desired discrimination. The first method is direct, i.e., all discriminating variables are used. In the second method, a stepwise selection procedure is used. Based on a user-defined criterion, the procedure starts with the single best discriminating variable. A second discriminating variable is selected if when combined with the first variable greater discrimination results. Third and subsequent variables are selected at each remaining step, along with simultaneous variable elimination if greater discrimination results. After all variables have been considered (or if the remaining variables do not render increased discrimination), the procedure stops (Klecka, 1975:436).

In this case, the user-defined criterion was to maximize the smallest Mahalanobis distance (McNichols, 1980:(7-44)-(7-48)) between two groups. The Mahalanobis distance can best be defined by starting with the definition of Euclidean distance in p -dimensional space. Two points x_1 and x_2 are a squared distance D^2 apart; in vector terms this can be expressed as (Fig. 18)

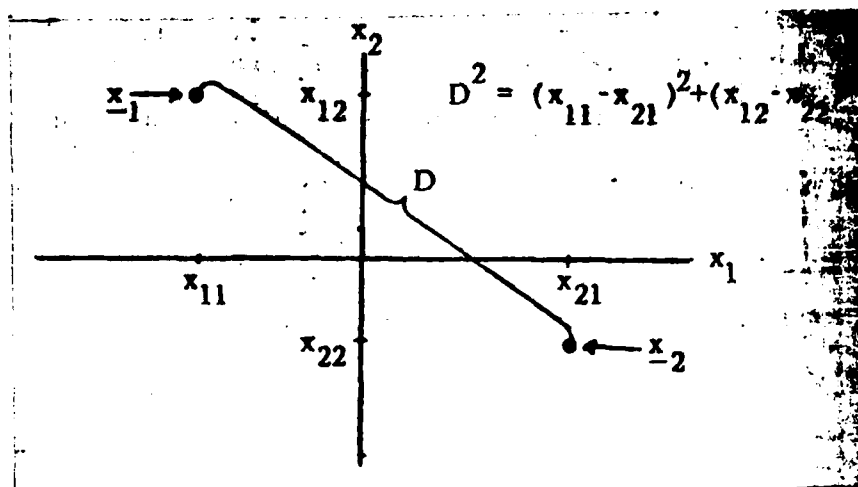


FIGURE 18. Euclidean Distance (McNichols, 1980:(7-44))

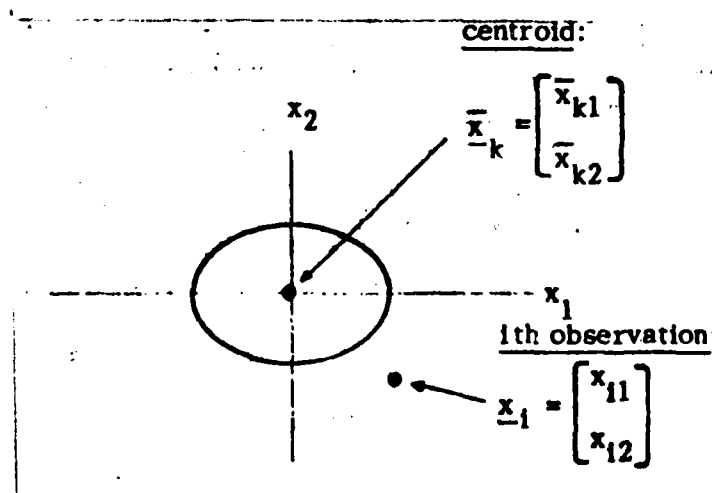


FIGURE 19. Euclidean Distance of an Observation From the Centroid (McNichols, 1980:(7-45))

$$D^2 = (x_1 - x_2) \cdot (x_1 - x_2) = \sum_{j=1}^p (x_{1j} - x_{2j})^2 \quad (28)$$

Intuitively, one would expect a case that is closest to a particular group centroid (smallest D) would be assigned to that group. The problem with this approach can be seen by examining Fig. 19 that represents a multivariate population distribution, looking down on an x_1 - x_2 plane in the case with two variables (McNichols, 1980:(7-45)).

The reason why Euclidean distance is not used has to do with the fact that the distance along the x_2 dimension is more meaningful statistically than in the x_1 dimension; this is because the x_1 standard deviation is larger than the x_2 standard deviation. Therefore, an observation has a greater possibility of being one unit away from the centroid in the x_1 direction than in the x_2 direction (McNichols, 1980:(7-45)-(7-46)).

In order to compensate for this, both the x_1 and x_2 coordinates are divided by their respective standard deviations. With this correction, the squared distance between any observation x_i and a centroid x_k will be

$$D^2 = \sum_{j=1}^2 [(x_{ij} - \bar{x}_{kj}) / \sigma_j]^2 \quad (29)$$

Rewritten in matrix notation

$$D_2 = [x_{i1} - \bar{x}_{k1}, x_{i2} - \bar{x}_{k2}] \underbrace{\begin{bmatrix} 1/\sigma_1 & 0 \\ 0 & 1/\sigma_2 \end{bmatrix}} \begin{bmatrix} 1/\sigma_1 & 0 \\ 0 & 1/\sigma_2 \end{bmatrix} \begin{bmatrix} x_{i1} - \bar{x}_{k1} \\ x_{i2} - \bar{x}_{k2} \end{bmatrix} \quad (30)$$

Following McNichol's example, if we denote the bracketed

expression as Σ^{-1} , we finally have

$$D^2 = (x_i - \bar{x}_k)' \Sigma^{-1} (x_i - \bar{x}_k) \quad (31)$$

This final expression for D^2 is then the square of the Mahalanobis distance (McNichols, 1980:(7-46)-(7-48)).

How, then, does one evaluate the printed output generated by the discriminant analysis subprogram? The subprogram used (DISCRIMINANT) outputs analytic features that allow one to evaluate the importance of the computed discriminant functions, as well as how to interpret the computed discriminant function coefficients. Discussion of these features appear in the ensuing paragraphs.

Space does not allow a full mathematical development of discriminant analysis, but the two main assumptions that must be presented are that the discriminating variables have a multivariate normal distribution, and that they have equal variance-covariance matrices within each group. Fortunately, the technique is sufficiently robust to allow some departure from the stated assumptions (Klecka, 1975:435). At any rate, in order to determine the coefficients, an eigenvector problem of the type

$$WA = \lambda Ba \quad (32)$$

must be solved. Here B and W are the "between-groups" and "within-groups" sums of squares and crossproducts, respectively.

For each discriminant function, there is a corresponding eigenvalue λ . Since there may be several functions, it would be desirable to assess the importance of one over the others. The eigenvalue is such a measure; it is the relative importance of each function, where the sum of the eigenvalues is a measure of the total variance existing in the discriminating variables (Klecka, 1975:442).

Another aid in judging the importance of a discriminating function is its canonical correlation. The canonical correlation, when squared, is the proportion of variance in the discrimination function as explained by the groups (Klecka, 1975:442).

A second method used to determine importance is to test for the statistical significance of discriminating information not already incorporated in earlier functions. Starting with no functions, and for each function thereafter, Wilk's lambda is computed. Wilk's lambda is an inverse measure of the discriminating power left in the original variables not yet removed by the discriminating functions. It can also be converted into a chi-square statistic in order to test for statistical significance (Klecka, 1975:442-443).

As was mentioned previously, the coefficients are a measure of each discriminating variable's contribution to the resulting discriminating function. DISCRIMINANT yields both standardized and unstandardized coefficients; standardized coefficients are derived so that the resulting discriminant

score, D_i , is in standard form. This means that for all cases used in the analysis, the score from one function will have a mean of zero and a standard deviation of one (Klecka, 1975: 443).

For computational purposes, standardized coefficients would be of little use as the discriminating variables are rarely in standard form; therefore, unstandardized coefficients are given if they are desired. However, unstandardized coefficients cannot be used to assess relative importance because they lack adjustment for both measurement scales and the variability found in the original variables (Klecka, 1975: 443-444).

After performing some initial runs, it became evident that some consistent method was needed to classify the rise in scintillation values (DS1, DS2, DP1, DP2) in order to yield reliable results. Here DS1 is the rise in S4 at 137 MHz, and DS2 is the rise in S4 at 413 MHz. Similarly, DP1 is the rise in PRMS at 137 MHz and DP2 is the rise in PRMS at 413 MHz. By running FREQUENCIES, which prints out a histogram, it was easier to get an idea of how the low, medium, and high values of the rise in scintillation were distributed. A histogram for DS1 appears in Fig. 20; DS1, DS2, DP1, and DP2 were broken out in terms of low, medium, and high values. Here the primary criteria for division was to ensure as near an equal size as possible of the three groups. Also, graphs of DS1 versus DS2 (Fig. 21) and DP1 versus DP2 (Fig. 22) are shown.

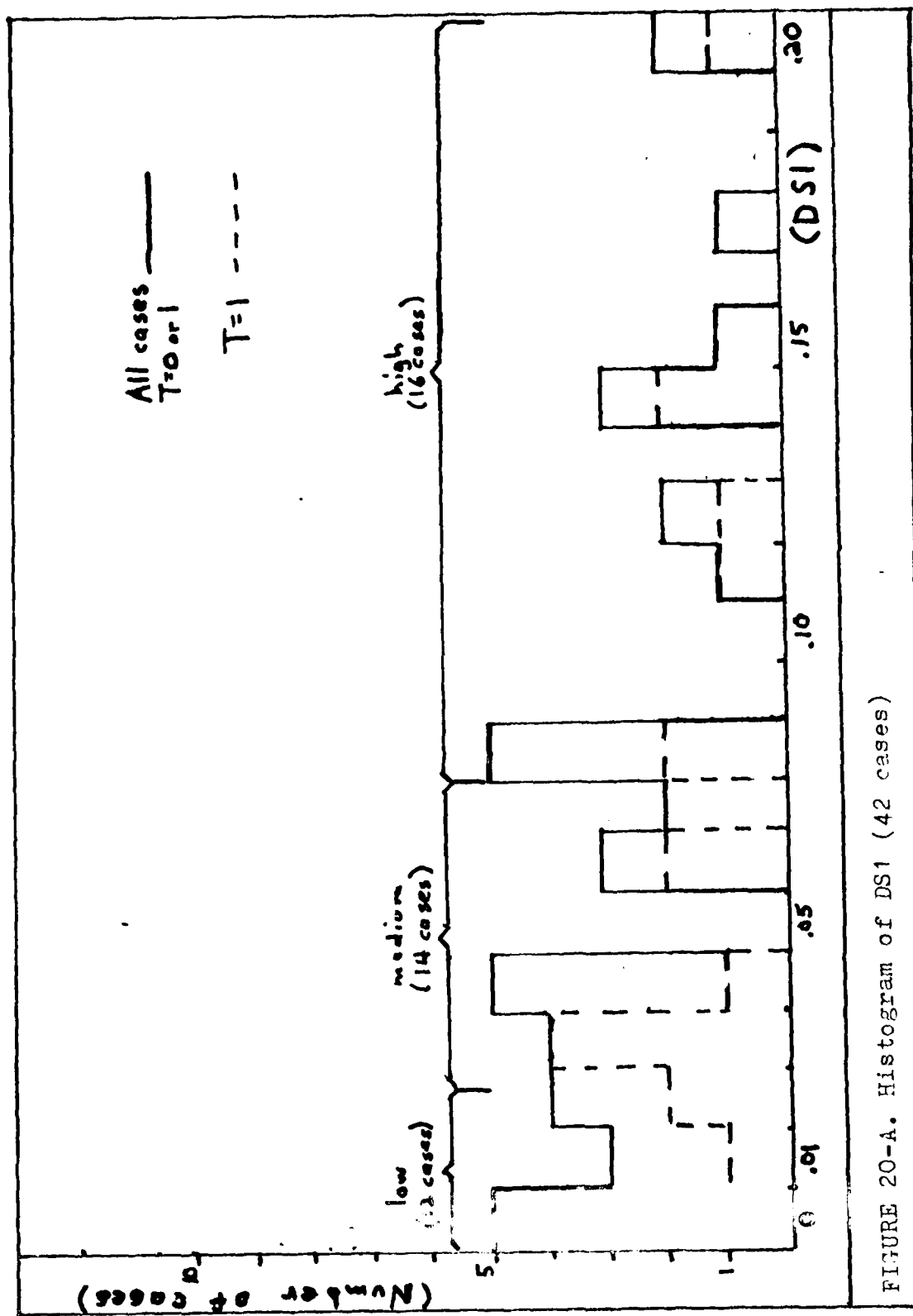


FIGURE 20-A. Histogram of DS1 (42 cases)

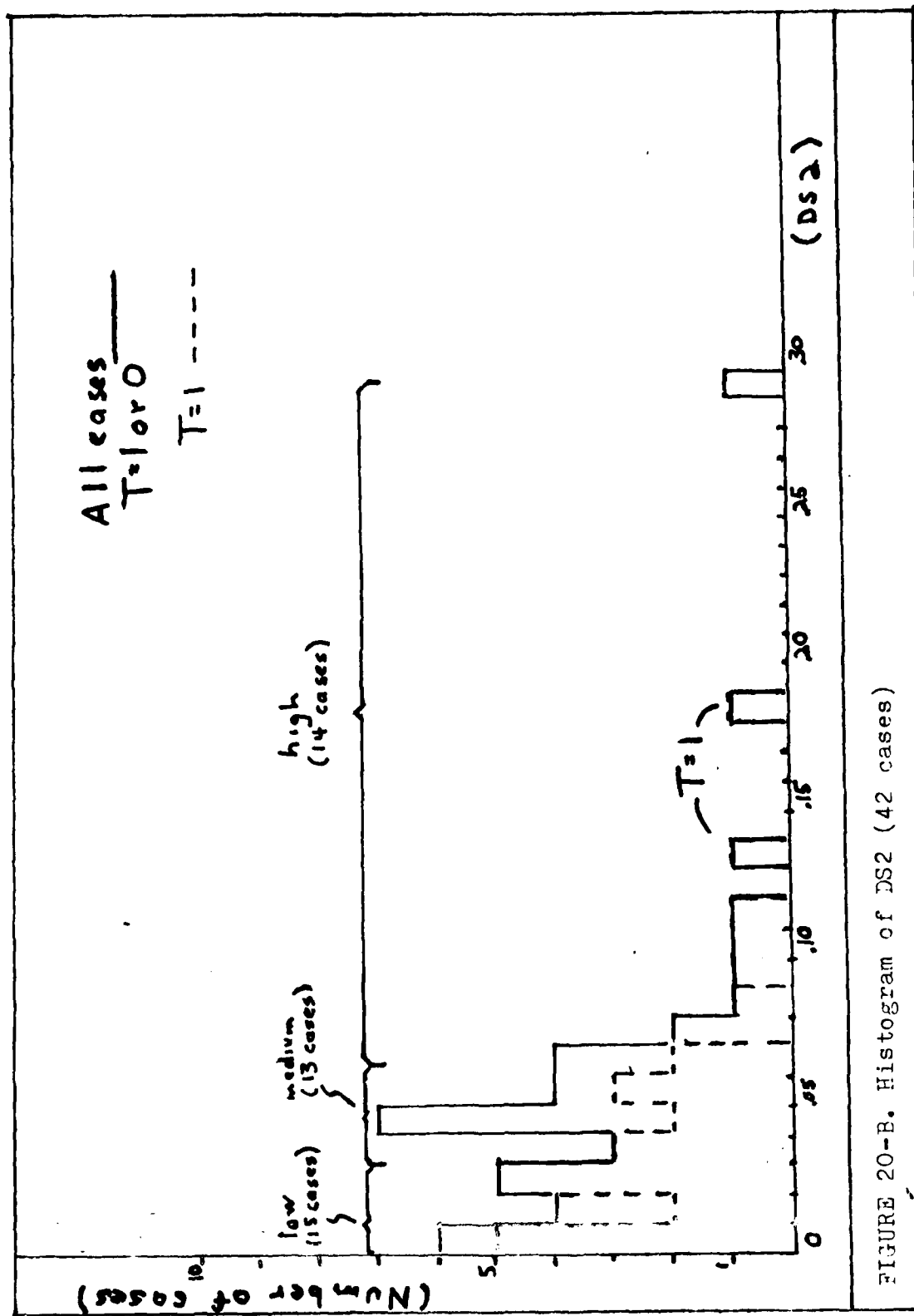


FIGURE 20-B. Histogram of DS2 (42 cases)

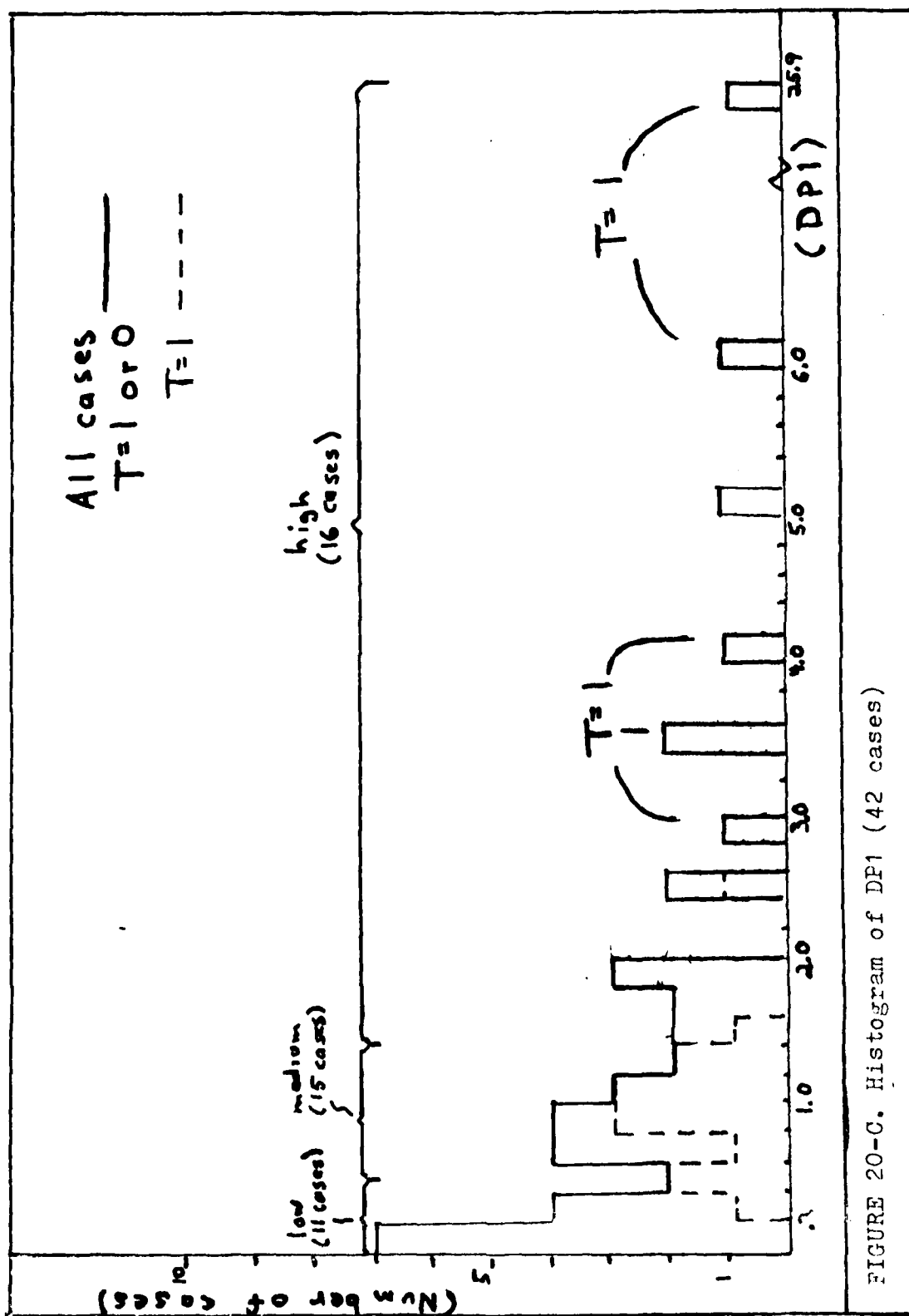


FIGURE 20-C. Histogram of DP1 (42 cases)

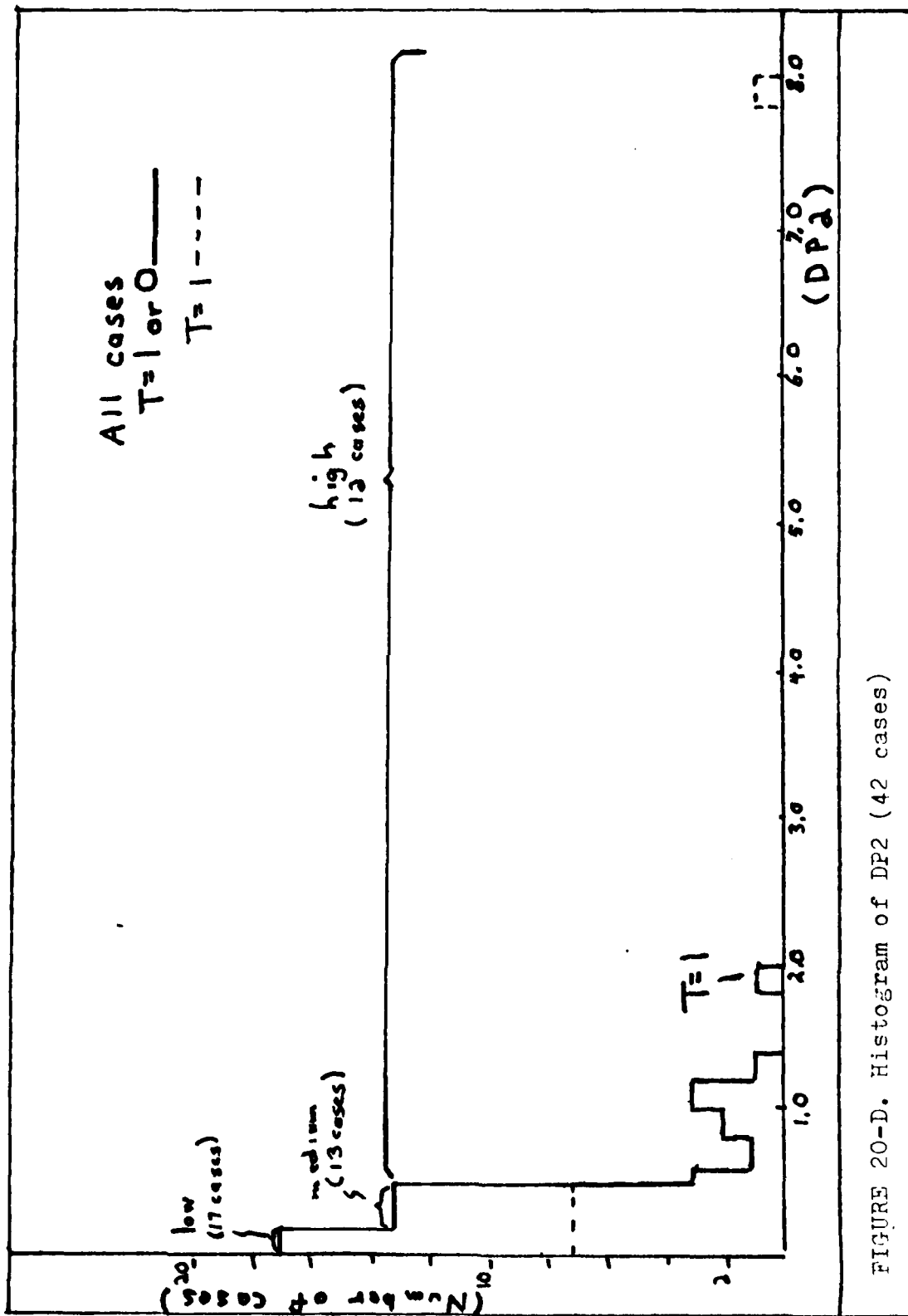


FIGURE 20-D. Histogram of DP2 (42 cases)

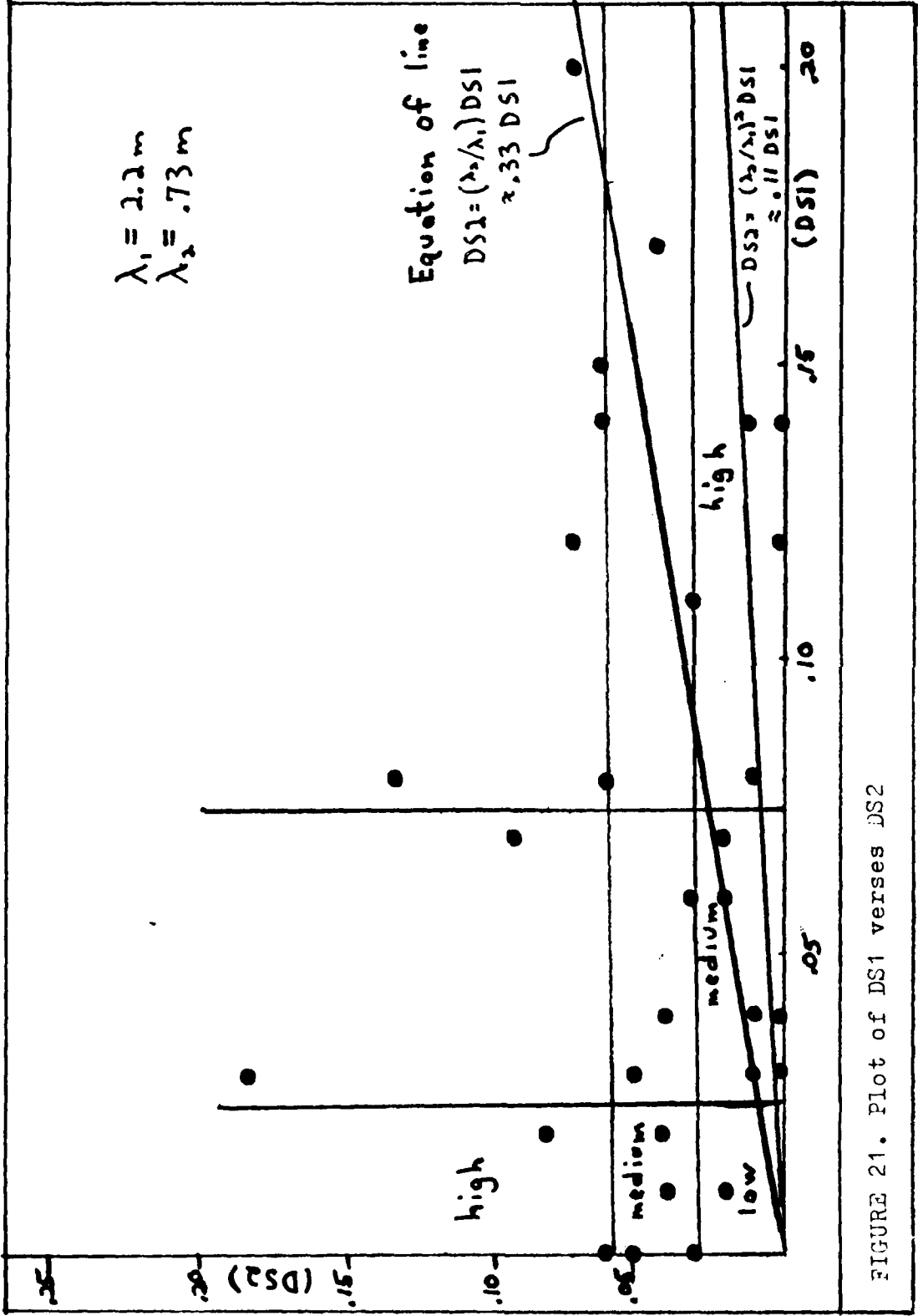


FIGURE 21. Plot of DS1 verses DS2

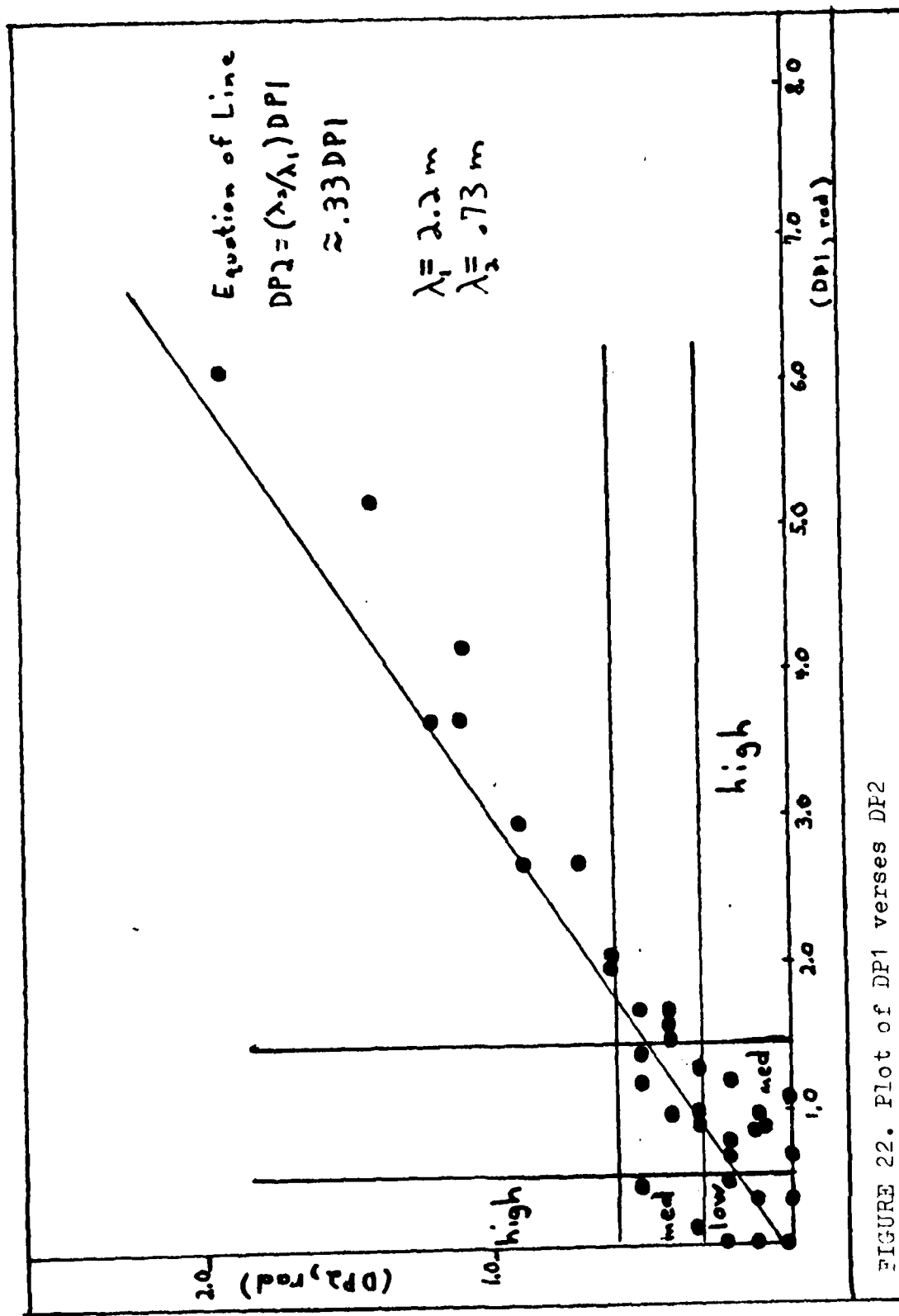


FIGURE 22. Plot of DP1 verses DP2

It was quite difficult to classify the DS1 and DS2 values because they often did not increase or decrease in concert with each other; the DP1 versus DP2 graph on the other hand gives a more consistent pattern, i.e., for a rise in DP1 there is a commensurate rise in DP2.

This fact is significant as it validates the expression (Eq (1)) for PRMS as put forth by Briggs and Parkin. Using this equation, we can establish the following ratio for DP1 and DP2

$$DP1/DP2 = \lambda_1 / \lambda_2 \quad (33)$$

as the other variables in Eq (1) are the same for the two radio frequencies. In this analysis, $\lambda_1 = 2.2$ m (since $f_1 = 137$ MHz) and $\lambda_2 = .73$ m (since $f_2 = 413$ MHz), making λ_1 / λ_2 approximately 3. In Fig. 23, DP2 is on the vertical axis and DP1 is on the horizontal axis, so that the slope of the line is about .33, or λ_2 / λ_1 as shown. Notice that the data agrees fairly well with the theory.

Briggs and Parkin presented expressions for S4 that did not show such a linear dependence on λ as in the case of PRMS; this may be the reason for the more scattered appearance of the distribution for DS1 versus DS2 as exhibited in Fig. 21. We might expect that the data would fall between the two curves that appear in Fig. 21; these curves represent the limiting cases of Eq (10). The upper line is Eq (11),

$$S(\lambda_1)/S(\lambda_2) = \lambda_1/\lambda_2 \quad (11)$$

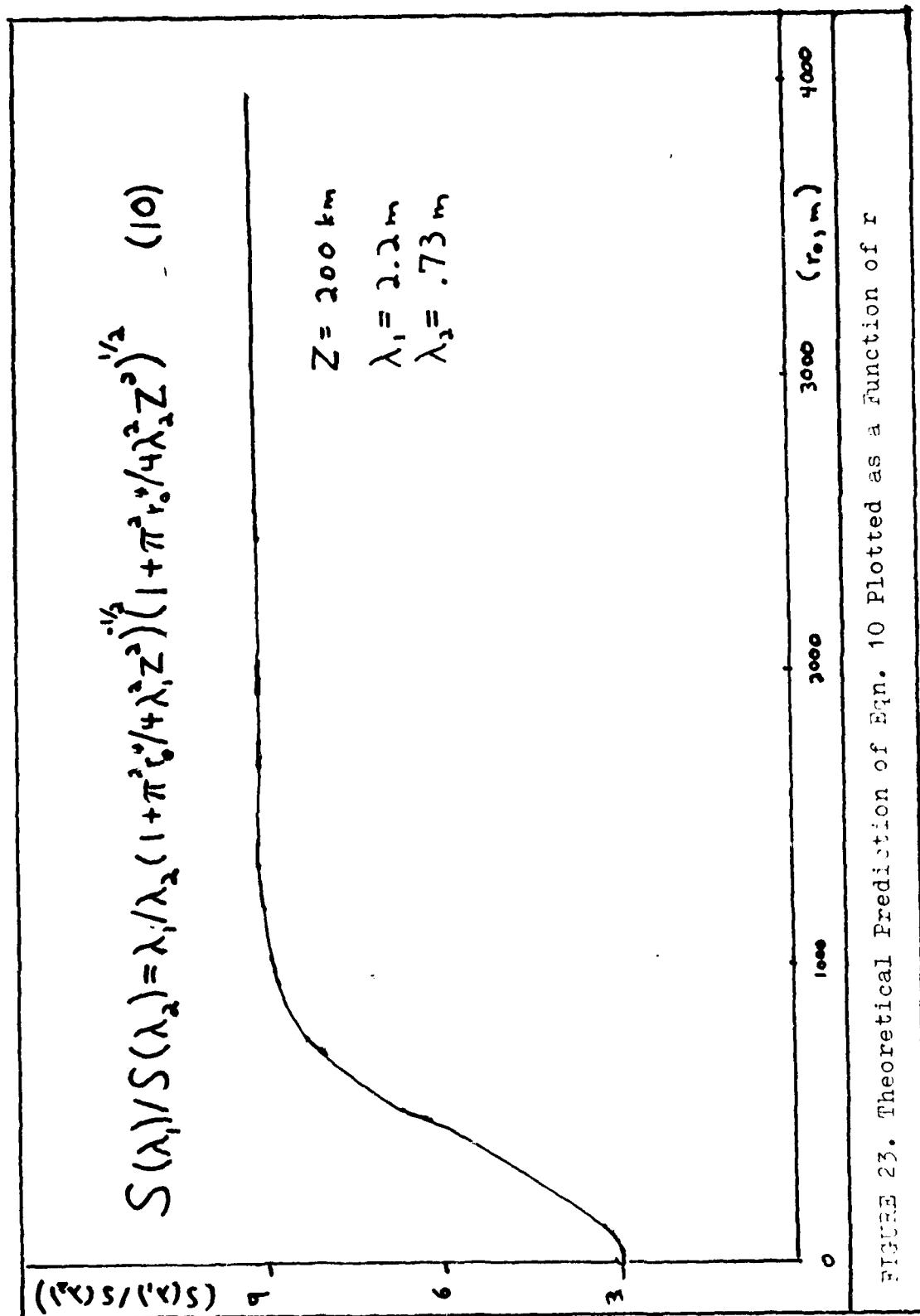


FIGURE 23. Theoretical Prediction of Eqn. 10 Plotted as a Function of r

AD-A163 835

STATISTICAL ANALYSIS OF LOW ENERGY ELECTRONS AND THEIR

2/2

RELATIONSHIP TO RA. (U) AIR FORCE INST OF TECH

WRIGHT-PATTERSON AFB OH SCHOOL OF ENGI. W E OBER

UNCLASSIFIED

DEC 84 AFIT/GSO/ENP-ENS/84D-3

F/G 4/1

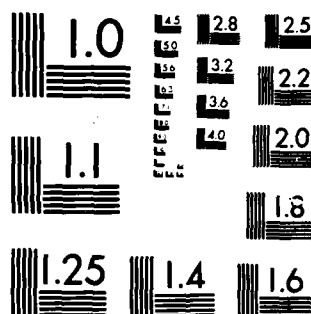
NL

END

FILED

14

DTL



as applied to this particular set of data (small value of r_0 , the traverse radius of the irregularity), and the lower line represents the case where r_0 is large (Eq (12)).

$$S(\lambda_1)/S(\lambda_2) = (\lambda_1/\lambda_2)^2 \quad (12)$$

We must also analyze Eq (10) in order to determine whether or not it is a monotonically increasing or decreasing function of r_0 . This is a necessary condition if all S4 data points are to be bounded by the curves denoting large and small values of r_0 . This can be done by differentiating Eq (10) with respect to r_0 , and then set the derivative to equal zero. If there is a value of r_0 that makes Eq (10) a minimum or maximum, then we can say that it is not a monotonic function. Eq (10) is repeated here for easier reference,

$$S(\lambda_1)/S(\lambda_2) = \lambda_1/\lambda_2 (1 + \pi^2 r_0^4 / 4 \lambda_1^2 Z^2)^{-1/2} (1 + \pi^2 r_0^4 / 4 \lambda_2^2 Z^2)^{1/2} \quad (10)$$

Differentiating and setting equal to zero using the product rule yields

$$\lambda_1/\lambda_2 \left[-\frac{1}{2} (1 + \pi^2 r_0^4 / 4 \lambda_1^2 Z^2)^{-3/2} (\pi^2 r_0^3 / \lambda_1^2 Z^2) (1 + \pi^2 r_0^4 / 4 \lambda_2^2 Z^2)^{1/2} + (1 + \pi^2 r_0^4 / 4 \lambda_1^2 Z^2)^{-1/2} (\pi^2 r_0^3 / \lambda_2^2 Z^2) (1 + \pi^2 r_0^4 / 4 \lambda_1^2 Z^2)^{-1/2} \right] = 0 \quad (34)$$

Simplification leave

$$(\lambda_2/\lambda_1)^2 (1 + \pi^2 r_0^4 / 4 \lambda_2^2 Z^2) = (1 + \pi^2 r_0^4 / 4 \lambda_1^2 Z^2)^{-3/2} \quad (35)$$

The only way that Eq (35) can be true is if r_0 is zero and $\lambda_1 = \lambda_2$; clearly λ_1 is not equal to λ_2 in this case. As a

further check, Eq (10) is plotted for a range of r_0 values (1-4000 m, Fig. 23). The value Z , which is the "reduced distance" $z_1 z_2 / (z_1 + z_2)$ is computed for the case when the satellite is directly overhead. Taking the height of the irregularity $z_1 = 350$ km, z_2 is then the satellite altitude $h = 800$ km minus z_1 . This gives a Z of approximately 200 km. In Fig. 23 and in Eq (10), the limiting case $S(\lambda_1)/S(\lambda_2) = \lambda_1/\lambda_2$ results when $\pi^2 r_0^4 / 4 \lambda_1^2 Z^2 \ll 1$ and $\pi^2 r_0^4 / 4 \lambda_2^2 Z^2 \ll 1$. The other limiting case $S(\lambda_1)/S(\lambda_2) = (\lambda_1/\lambda_2)^2$ results when $\pi^2 r_0^4 / 4 \lambda_1^2 Z^2 \gg 1$ and $\pi^2 r_0^4 / 4 \lambda_2^2 Z^2 \gg 1$. In the first case, if $\pi^2 r_0^4 / 4 \lambda^2 Z^2 \leq 0.1$, then r_0 is on the order of 10 m. In the second case, if $\pi^2 r_0^4 / 4 \lambda^2 Z^2 \geq 10$, then r_0 is on the order of a kilometer.

A significant amount of the data appearing in Fig. 21 lie in the vicinity of the two curves. There are a few outliers (DS1 less than .10, DS2 less than .05); however, the reason for this is not clear.

One point of concern dealt with the independence of the discriminating variables with respect to each other; in particular, the time integrated number flux PTIME. The reason being that for each case PTIME was computed from PEAK and TIME. For example, in the case where the area under the PEAK curve approximated a square PTIME was just PEAK times TIME. In the case where the area under the PEAK curve was not so clear cut, it was subdivided into simple square and triangular areas so that PTIME was basically the summed area of the smaller subdivisions, still making it a function of PEAK and TIME.

Fortunately, a Pearson correlation coefficient routine is available in SPSS; the Pearson correlation coefficient is a measure of the strength and direction (negative being inversely proportional, positive being directly proportional) of correlation between two variables. Table 5 contains the results of pairwise comparisons of the five discriminating variables; note that both PEAK and TIME are highly correlated with PTIME (.7087 and .7064, respectively). Two series of discriminant analysis runs were subsequently made; one with PTIME and one without PTIME for the sake of comparison.

In Table 6 we have the results of a stepwise selection discriminant analysis run, where the variable CAT is the overall, or average score for a particular case based on all four scintillation variables. This is done by using the classification histograms (Fig. 20); for a given case, the classification for each variable (DS1, DS2, DP1, and DP2) is noted. Letting low=1, medium=2, and high=3, the overall classification is obtained by adding up the four values and then dividing by four. The problem with this approach is that for a given case one might have a low DS1 value, a medium DS2 value, a high DP1 value, and a medium DP2 value; it became evident that this method failed to give meaningful results.

Instead of attempting a discriminant analysis on the 42 cases of interest based on overall classification for each case, eight different types of classifications were devised. They are C137 (DS1 and DP1), C413 (DS2 and DP2), CS4 (DS1

TABLE 5. Pearson Correlation Coefficient Printout

PEARSON CORRELATION COEFFICIENTS

	PEAK	TIME	PTIME	EAVG	DT
PEAK	1.0000 (0) P=*****	.2968 (42) P=.028	.7087 (42) P=.001	-.3070 (42) P=.024	-.2253 (42) P=.076
TIME	.2968 (42) P=.028	1.0000 (0) P=*****	.7064 (42) P=.001	.1148 (42) P=.235	-.2659 (42) P=.044
PTIME	.7087 (42) P=.001	.7064 (42) P=.001	1.0000 (0) P=*****	-.1008 (42) P=.263	-.1925 (42) P=.111
EAVG	-.3070 (42) P=.024	.1148 (42) P=.235	-.1008 (42) P=.236	1.0000 (0) P=*****	-.2313 (42) P=.070
DT	-.2253 (42) P=.076	-.2659 (42) P=.044	-.1925 (42) P=.111	-.2313 (42) P=.070	1.0000 (0) P=*****

(COEFFICIENT / CASES / SIGNIFICANCE) (99.0000 MEANS UNCOMPUTABLE)

Table 6. Classification Based on CAT, w/PTIME

<u>Function</u>	<u>Eigenvalue</u>	<u>After Function</u>	<u>Wilk's λ</u>	<u>Sig</u>
		0	.766	.119
1	.168	1	.895	.121
2	.118			

Standardized Discrimination Coefficients

	<u>Func1</u>	<u>Func2</u>
TIME	.44469	1.35076
PTIME	.24721	-1.25659
DT	-.65380	.27246

Classification Results

Actual Group	# of cases	<u>Predicted Group Membership</u>		
		<u>1</u>	<u>2</u>	<u>3</u>
Group 1	13	8 (61.5)	3 (23.1)	2 (15.4)
Group 2	15	5 (33.3)	7 (46.7)	3 (20.0)
Group 3	14	4 (28.6)	3 (21.4)	7 (50.0)

% of grouped cases correctly classified - 52.38

and DS2), CPRMS (DP1 and DP2), CS1 (DS1), CS2 (DS2), CP1 (DP1), and CP2 (DP2). Again, for each of the eight types of classification, the same three groups based on the histograms appearing in Fig. 20 are used. For C137, C413, CS4, and CPRMS, overall classification is decided by summing the value of each variable (again from Fig. 20) and then dividing by two; in the event that a non-integer result was obtained, the overall classification was determined by rounding down.

Another concern that arose out of the initial discriminant analysis runs was that many of the observed low changes in scintillation occurred before an enhancement was encountered, i.e., $T=1$. When no scintillation occurs, it is conceivable that the observed enhancement may have begun just at the time it is observed by the satellite. Hence, a series of eight runs (one for each type of classification) without the questionable cases ($T=1$ and low scintillation value) was performed. The total number of cases then were as high as 38, with a low of 30. For eight runs, the average number of cases was approximately 33. Low scintillation values for CS1 and CS2 were DS1 and DS2 values less than or equal to .02. Low values for CP1 were DP1 values less than or equal to .4, and low CP2 values were less than or equal to .2 for DP2. The low values for C137 ($DS1 \leq .02$ and $DP1 \leq .4$), C413 ($DS2 \leq .02$ and $DP2 \leq .2$), CS4 (both $DS1$ and $DS2 \leq .02$), and CPRMS ($DP1 \leq .4$ and $DP2 \leq .2$) are based on the same criterion for low scintillation values as CS1, CS2, CP1, and CP2.

In Table 7 we have the results of the discriminant analysis based on CPRMS without the use of PTIME. Two functions were computed, with the first being more important than the second based on its larger eigenvalue (.361 compared to .091). In the upper right hand corner, notice that a good deal of discriminating power exists in the first function as evidenced by the Wilk's lambda value of .674. In this research effort, a Wilk's lambda with a corresponding significance value less than .10 is considered to be statistically meaningful. In this example, the computed significance is .020, so that the first discriminant function will yield separation between the groups that will not be solely due to chance. The second function has a corresponding Wilk's lambda of .916 and a significance of .191, indicating that it will not aid much in providing discrimination between the groups.

Upon inspection of the computed discriminant function coefficients for both functions, we see that in Function 1 TIME and DT make the largest contribution (sign indicating positive or negative contribution), with EAVG being of less importance. In Function 2, which is not significant, EAVG makes the largest contribution followed by DT, with TIME being the lesser contributor of the three.

Based on the computed discrimination functions, the classification results appear at the bottom of the table. For example, there were 19 Group 1 members (low scintillation) to start with; the computed classification functions placed

Table 7. Classification Based on CPRMS w/o PTIME

<u>Function</u>	<u>Eigenvalue</u>	<u>After Function</u>	<u>Wilk's λ</u>	<u>Sig</u>
		0	.674	.020
1	.361	1	.916	.191
2	.091			

Standardized Discrimination Coefficients

	<u>Func1</u>	<u>Func2</u>
TIME	.82785	.19298
EAVG	-.02290	.95978
DT	-.46279	.55163

Classification Results

<u>Actual Group</u>	<u># of cases</u>	<u>Predicted 1</u>	<u>Group 2</u>	<u>Membership 3</u>
Group 1	19	13 (68.4)	5 (26.3)	1 (8.3)
Group 2	12	3 (25.0)	8 (66.7)	1 (8.3)
Group 3	11	4 (36.4)	4 (36.4)	3 (27.3)

% of grouped cases correctly classified - 57.14

13 of the Group 1 members in Group 1, five in Group 2, and one in Group 3. The Group 2 members were not classified quite as well, and the Group 3 members were for the most part incorrectly classified. The overall percentage of cases correctly classified is 57.14, or about 24 of the 42 cases. Another similar discriminant analysis based on PRMS was made that included PTIME as a discriminating variable; however, the final results were identical to those presented above.

The other three classifications that rendered significant results were based on C413, CS1, and CP2 (see Appendix C and Table 8). Note that in the CS1 run there was a difference in final results when PTIME was included; however, PTIME's inclusion does little to increase separation between the groups. A similar situation exists with C413; without PTIME the results are significant, but with PTIME's inclusion both of the eigenvalues and, therefore, the discriminant functions are not significant. Table 8 contains a summary of the results of all eight runs where all 42 cases are used.

In the other 16 runs where the questionable low valued observations were discarded, the classifications that rendered significant results were C413 and CPRMS (see Appendix D). The overall results for this series of runs appears in Table 9.

In Table 10 we have a comparison of the two series of runs. For each classification, the significance for each series (all 42 cases versus the situation where the questionable cases are eliminated, designated T=1) and the

Table 8. Discriminant Analysis Results For All Cases
(both T=0 and T=1)

Number of Cases	Classification	After Function	Wilk's λ	Sig
42	C137	0 1	.929 -----	.240 -----
42	*C413(w/oPTIME)	0 1	.858 -----	.051 -----
42	C413(w/PTIME)	0 1	.830 .996	.127 .678
42	CS4	0 1	.910 -----	.159 -----
42	*CPRMS	0 1	.674 .916	.020 .191
42	*CS1(w/oPTIME)	0 1	.798 .916	.069 .067
42	*CS1(w/PTIME)	0 1	.749 .872	.089 .074
42	CS2	0 1	(no results)	
42	CP1(w/oPTIME)	0 1	.945 -----	.329 -----
42	CP1(w/PTIME)	0 1	.843 .966	.161 .251
42	*CP2	0 1	.700 .921	.035 .208

* Significant

Table 9. Discriminant Analysis Results For
Only T=1 Cases

Number of Cases	Classification	After Function	Wilk's λ	Sig
34	C137	0 1	.921 -----	.277 -----
32	*C413	0 1	.679 .883	.026 .059
30	CS4	0 1	.901 -----	.244 -----
33	*CPRMS	0 1	.775 .902	.110 .082
34	CS1	0 1	.764 .903	.234 .217
31	CS2	0 1	(no results)	
38	CP1(w/oPTIME)	0 1	.824 1.000	.154 .997
38	CP1(w/PTIME)	0 1	.750 .945	.135 .383
34	CP2	0 1	.871 -----	.118 -----

* Significant

Table 10. Comparison of Discriminant Analysis Results

Classification	Significance		Discriminating Variables	
	(T=0 and 1, 42)	(T=1 cases, 30-38)	(T=0 and 1, 42)	(T=1 cases, 30-38)
C137	.240	.277	EAVG(1.0)	TIME(1.0)
C413	.051, *.127	.026	TIME(1.0) *PTIME(.76) *DT(-.57)	PEAK(-.08) DT(.99)
CS4	.159	.244	TIME(1.0)	TIME(1.0)
CPRMS	.020	.110	TIME(.83) EAVG(-.02) DT(-.46)	TIME(-.67) DT(.74)
CS1	.067, *.089	.234	PEAK(1.0) EAVG(.64) *PEAK(-.06) *PTIME(.87) *EAVG(-.51)	PEAK(.84) TIME(-.27) EAVG(1.0)
CS2	(no results)		-----	-----
CPI	.329, *.161	.154, *.135	TIME(1.0) *TIME(1.4) *PTIME(-1.3)	PEAK(.72) DT(.98) *TIME(-.89) *PTIME(1.2) *DT(.70)
CP2	.035	.118	TIME(-.65) EAVG(1.4) DT(.70)	DT(1.0)

* With PTIME

discriminating variables that appear in the discriminant function are shown. Next to the discriminating variables appears the corresponding discrimination coefficients rounded off to two significant digits for comparison purposes.

The results can be interpreted in light of the results presented by Briggs and Parkin. The classification based on CS1 (rise in S4 at 137 MHz) shows that PEAK (electron number flux peak value) and EAVG (average energy) are important discriminators. Consider the situation where the significance level is .067 (PTIME not included). Upon inspection of Eq (5), we see that S4 is proportional to PRMS which is in turn proportional to electron number density N (Eq (1)). This is consistent with the fact that PEAK is a good discriminating variable. EAVG has a large positive contribution as well (.64), indicating that the higher the energy of the electron, the greater the collisional ionization in the ionosphere. This is again a condition one would expect necessary to sustain irregularity production, which in turn would increase S4 scintillation. Since amplitude scintillations at 137 MHz are larger than S4 values at 413 MHz, such a dependence on PEAK and EAVG would be more evident for the CS1 case; this may explain why a similar result did not appear in the CS2 runs.

One would expect similar results in the case of CP1 and CP2 (category based on the rise in PRMS at 137 MHz and 413 MHz, respectively), yet only for the CP2 classification do we get significant results. Since PRMS is linear in number

density N, we might expect the same discriminant variables as in the case of CS1. However, the discriminant variables that gave the best discrimination for classification based on CP2 were TIME (-.65), DT (.70), and EAVG (.14).

In the case where classification is based on both DP1 and DP2 together (CPRMS), we get similar results: TIME (.83), DT (-.46), and EAVG (-.02). In both cases (CP2 and CPRMS), the physical size of the enhancement and the time between enhancement encounter and scintillation occurrence are important indicators. In each instance, the average energy EAVG plays a minor role in discrimination.

The only other case that gave statistically meaningful results was C413; since its discriminating variables are both TIME and, in the case where questionable low scintillations were discarded, DT (.99). This result is similar to that found with the CPRMS and CP2 classifications. Since the CS2 classification failed to produce any results whatsoever, we conclude that the significant discrimination in the case of C413 is most likely due to the significant discrimination of DP2. With this information, the discriminant analysis based on C137 and C413 are probably redundant.

VIII. Conclusions and Recommendations

Conclusions

The 198 low energy electron enhancements were found to exist primarily in the nighttime sectors, with a large number occurring in both the 0300 sector and in the 2300 sector. There was a sharp dropoff in enhancements shortly after 0700 MLT, with none (except for one instance at 0800 MLT) appearing until approximately 1500 MLT.

Of the 73 enhancements that were used to study the possibility of associated Birkeland currents, only nine enhancements had such corresponding currents. It appeared that there may be a correlation between the number flux (PEAK) and the computed current density J_{\parallel} ; more statistics are needed for such a study.

The average value of PEAK was found to be 9.7×10^8 electrons/cm²-sec-ster, with a wide standard deviation of 9.6×10^8 electrons/cm²-sec-ster. Enhancements with PEAK values greater than 2×10^9 electrons/cm²-sec-ster were the same ones that had corresponding geomagnetic field disturbances as mentioned above.

The plot of the PRMS data (DP1 versus DP2) agreed well with the theory as presented by Briggs and Parkin, i.e., PRMS is linear in λ . The plot of the S4 data (DS1 versus DS2) was not nearly as linear; after plotting curves for the limiting cases of the equation for the ratio of DS1 to DS2, many data

points did fall in the vicinity of the two curves; however, many did not. Why this is so is not clear.

After performing several discriminant analysis runs, the results that were statistically meaningful (for 42 cases) appeared in the runs where classification was based on C413, CPRMS, CS1, and CP2. When we eliminated low scintillation cases where the scintillation occurred before the enhancement encounter ($T=1$), the classifications that gave significant results were based on C413 and CPRMS.

In the situation where the discriminant analysis was based on CS1 (classified by rise in S4 at 137 MHz), the discriminating variables were PEAK and EAVG. Since S4 is proportional to PRMS, which is in turn proportional to number density N , then the fact that PEAK is a discriminating variable is consistent with theory. We also expect EAVG to be an indicator of amplitude scintillation as well; higher electron energies will result in increased collisional ionization. This, in turn, will contribute to irregularity development, which is responsible for amplitude scintillation. Since DS1 (rise in S4 at 137 MHz) is larger than DS2 (rise in S4 at 413 MHz), this may explain why discrimination analysis was successful in the former case and not the latter.

In the discriminant analysis results where the size of PRMS was the criteria of classification, CP2 (classification based on the rise in PRMS at 413 MHz) and CPRMS (classification based on the rise in both PRMS values) both had TIME

(time necessary for the satellite to traverse the enhancement, i.e., its physical size) and DT (time difference between scintillation occurrence and enhancement encounter; this is indicative of the length of the radio beam propagation path) as the major discriminating variables. In both situations, EAVG played only a minor role in discrimination.

The fact that classification by C413 (S4 and PRMS at 413 MHz) produced significant results is probably due to DP2's ability to be grouped significantly. Since the discriminating variables are the same for this situation as for the CP2 case, the discriminant analysis based on C413 (and C137) is probably redundant.

Recommendations

As was mentioned in Chapter VII, the scintillation data points used in this thesis effort were averaged over 15 seconds, thereby making it far more difficult to establish a relationship between the enhancements and observed scintillations, especially if the latter are small. A way to alleviate this situation would be to increase the time resolution of the scintillation data to something on the order of one second as opposed to fifteen seconds. Whether this can easily be accomplished with the HILAT satellite is unknown; any future spaceborne radio scintillation experiment attempting to investigate the enhancement/scintillation relationship might consider this recommendation.

A second recommendation is that at least an order of magnitude more enhancements need to be analyzed in order to improve statistical results. Time did not allow all three months worth of data to be analyzed in any detail; all passes during the three month period that contain enhancements should be studied. In fact, a study done with six months worth or more of HILAT data might give more conclusive results.

This would allow one to gather more data on magnetic field disturbances, and by performing a linear regression analysis, more could be learned about the relationship between enhancements and magnetic disturbances. It would also be interesting to see if enhancements correlate with both magnetic field disturbances and scintillations; this was an early consideration in this thesis, but a lack of data prevented such an analysis. More enhancement data would also allow for more accurate descriptors such as the average peak number flux.

The discriminant variables describing the enhancements in this analysis may not be the best ones available to explain how scintillations change. There may indeed be some characteristic inherent in enhancements that render better separation than those used here.

A final recommendation is a long time-period study to track the effect of solar activity on scintillation occurrence. Although traditionally K_p has been used as an indicator of solar activity, a better indicator is solar wind.

MODE = 3 1984 DAY 21 KP = 0
ZENITH

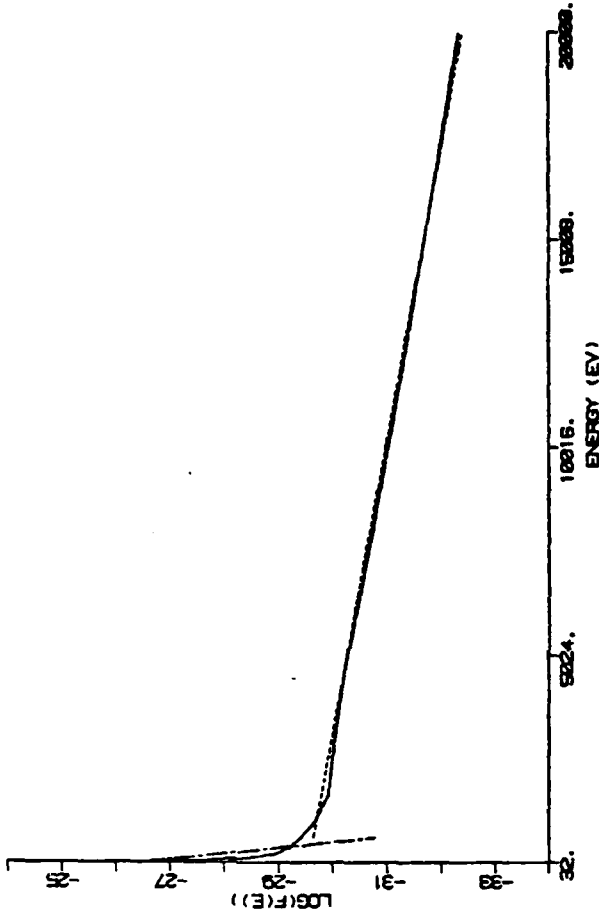
UT MLAT MLON OGMT
24730 70.0 58.5 0622

N = .56 T = .3544E+08
N = 3.10 T = .7038E+06

NUMBER 2 OF 60

CHANNEL	RAW COUNTS	DSPC	FSPC
1	183.0	7.58	-24.51
2	415.0	5.02	-25.38
3	37.0	5.64	-26.88
4	11.0	4.00	-27.83
5	7.0	4.10	-28.45
6	6.0	4.21	-28.05
7	0.0	4.18	-28.20
8	10.0	4.10	-28.40
9	35.0	4.13	-28.68
10	51.0	4.10	-28.02
11	99.0	4.23	-30.01
12	147.0	4.24	-30.21
13	110.0	4.01	-30.66
14	57.0	3.55	-31.32
15	12.0	2.76	-32.33
16			

AEGY 1.23
LOG EFLX 8.00
LOG IFLX 8.80
E1= 20
E2= 632
E3= 20000



APPENDIX A-1. Distribution Spectrum: 24730 sec U.T.
21. January 1984

COPY THIS ONE FIRST [Y] OR SKIP IT [N] ?
CURRENT END POINTS ARE E1= 1 E2= 0 E3= 15
DO YOU WANT TO CHANGE THEM [Y] OR NOT [N] ?
CONTINUE [Y] OR RETURN TO MAIN MENU [N] ?

MODE = 3 1984 DAY 21 KP = 0
ZENITH

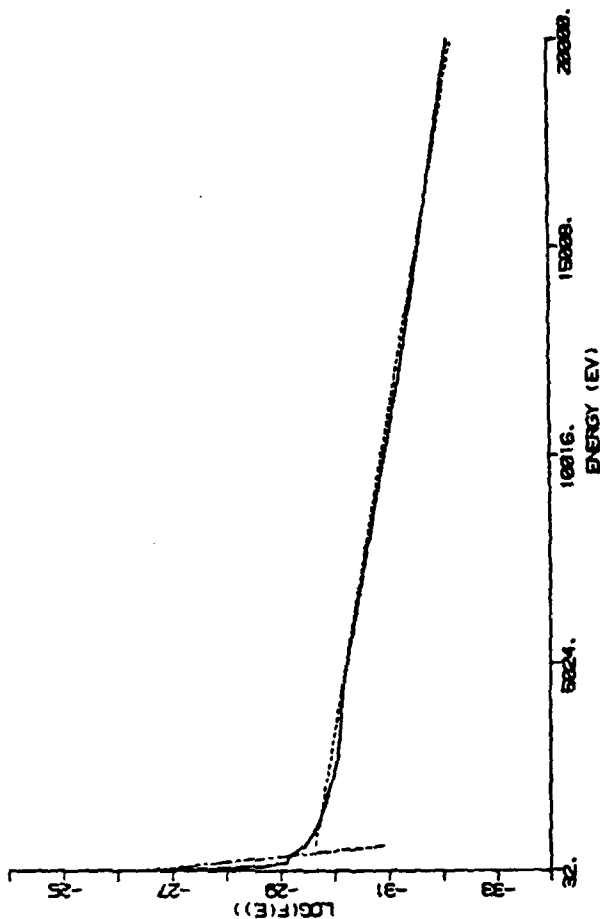
UT PLAT MLON ORALT
24730 70.0 58.5 0622

N = .60 T = .3900E+08
N = 3.02 T = .6338E+06

NUMBER 3 OF 60

CHANNEL	RAW COUNTS	DSPC	FSPC
1	110.0	7.56	-24.50
2	630.0	6.71	-25.10
3	43.0	4.94	-26.02
4	12.0	4.25	-26.70
5	4.0	4.04	-26.70
6	10.0	4.22	-26.12
7	15.0	4.14	-26.15
8	21.0	4.15	-26.45
9	30.0	4.17	-26.66
10	61.0	4.18	-26.84
11	97.0	4.28	-26.07
12	150.0	4.00	-30.17
13	143.0	3.62	-30.58
14	67.0	2.06	-31.25
15	10.0		-32.13

AEDY 1.33
LOG EFLX 9.05
LOG IFLX 8.93
E1= 20
E2= 632
E3= 20000



APPENDIX A-2. Distribution Spectrum: 24739 sec U.T.
21 January 1984

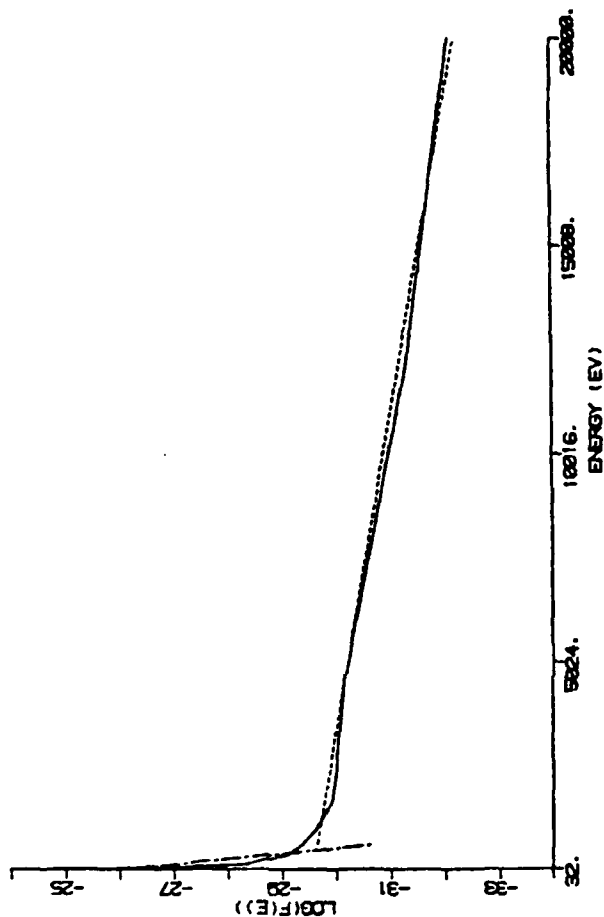
MODE = 3 1984 DAY 21 KP = 0
ZENITH

UT PLAT MLON CGLT
24730 70.0 53.5 0622

N = .62 T = .3705E+08
N = 6.17 T = .6687E+06

CHANNEL	RAW COUNTS	NUMBER 4 OF 60	DSPC	FSPC
1	831.0	7.43	24.67	24.67
2	1567.0	7.50	24.80	24.80
3	135.0	6.21	26.32	26.32
4	24.0	5.24	27.40	27.40
5	9.0	4.60	28.35	28.35
6	13.0	4.55	28.61	28.61
7	11.0	4.26	28.11	28.11
8	17.0	4.23	28.36	28.36
9	28.0	4.17	28.64	28.64
10	51.0	4.23	29.02	29.02
11	90.0	4.31	30.01	30.01
12	171.0	4.07	30.14	30.14
13	130.0	3.58	30.60	30.60
14	61.0	3.01	31.20	31.20
15	21.0		32.00	32.00

AEGY 1.84
 LOG EFLX 9.85
 LOG IFLX 9.84
 E1 = 20
 E2 = 632
 E3 = 20000



APPENDIX A-3. Distribution Spectrum: 24739 sec U.T.
21 January 1984

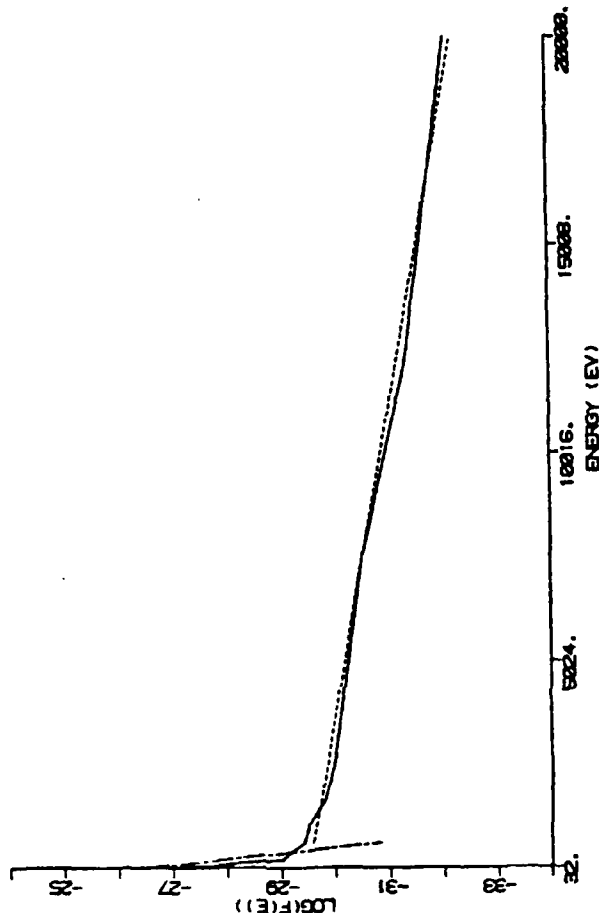
MODE = 3 1984 DAY 21 KP = 0
ZENITH

N = .66 T = .3690E+08
N = 2.02 T = .6081E+06

UT MJA1 MJA1 COMLT
24740 70.0 58.4 0622

CHANNEL	RAW COUNTS	DSPC	FSPC
1	847.0	7.43	-24.66
2	470.0	6.08	-25.32
3	23.0	5.44	-27.00
4	11.0	4.98	-27.83
5	12.0	4.73	-28.22
6	5.0	4.14	-28.03
7	10.0	4.22	-20.15
8	16.0	4.18	-20.42
9	23.0	4.31	-20.40
10	57.0	4.21	-20.82
11	65.0	4.23	-30.01
12	90.0	4.25	-30.20
13	151.0	4.15	-30.51
14	167.0	3.55	-31.32
15	57.0	2.08	-32.11
16	20.0		

AEQY 1.65
LOG EFLX 0.06
LOG IFLX 8.94
E1= 20
E2= 632
E3= 20000



APPENDIX A-4. Distribution Spectrum: 24740 sec U.T.
21 January 1984

DO YOU WANT TO CHANGE THEM (Y) OR NOT (N) ?N
CONTINUE (Y) OR RETURN TO MAIN MENU (N) ?N

MODE = 3 1984 DAY 21 KP = 0
ZENITH

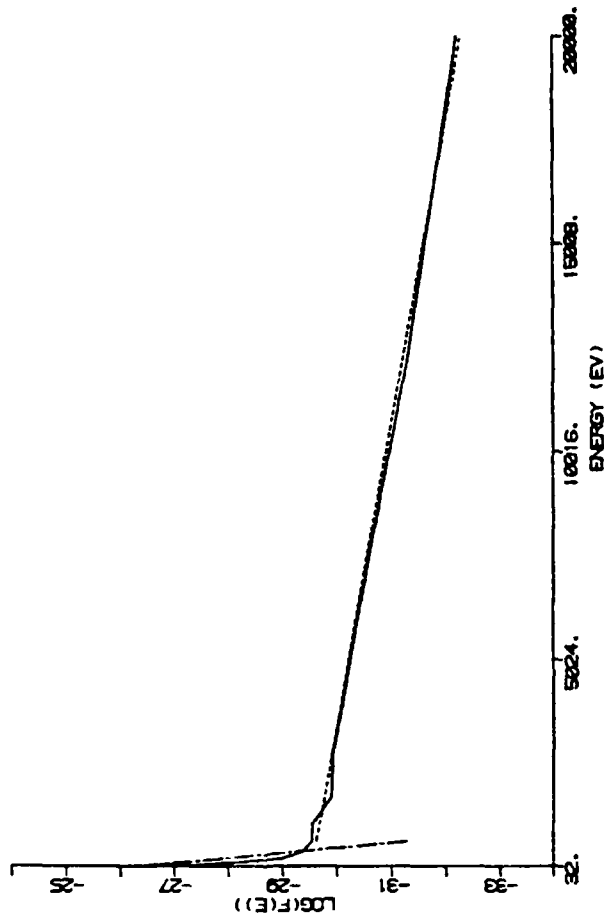
UT MLAT MLON CQMLT
24740 70.0 58.4 0622

N = .61 T = .3658E+08
N = 3.41 T = .6122E+06

NUMBER 5 OF 60

CHANNEL	RAW COUNTS	DSPC	FSPC
1	975.0	7.50	-24.60
2	383.0	6.80	-25.41
3	61.0	5.86	-26.66
4	16.0	5.07	-27.67
5	9.0	4.60	-28.35
6	5.0	4.14	-28.83
7	6.0	4.00	-29.38
8	7.0	4.05	-29.54
9	26.0	4.27	-29.54
10	51.0	4.13	-29.60
11	110.0	4.31	-29.03
12	155.0	4.27	-28.18
13	130.0	4.07	-28.50
14	61.0	3.58	-31.50
15	16.0	2.80	-32.21

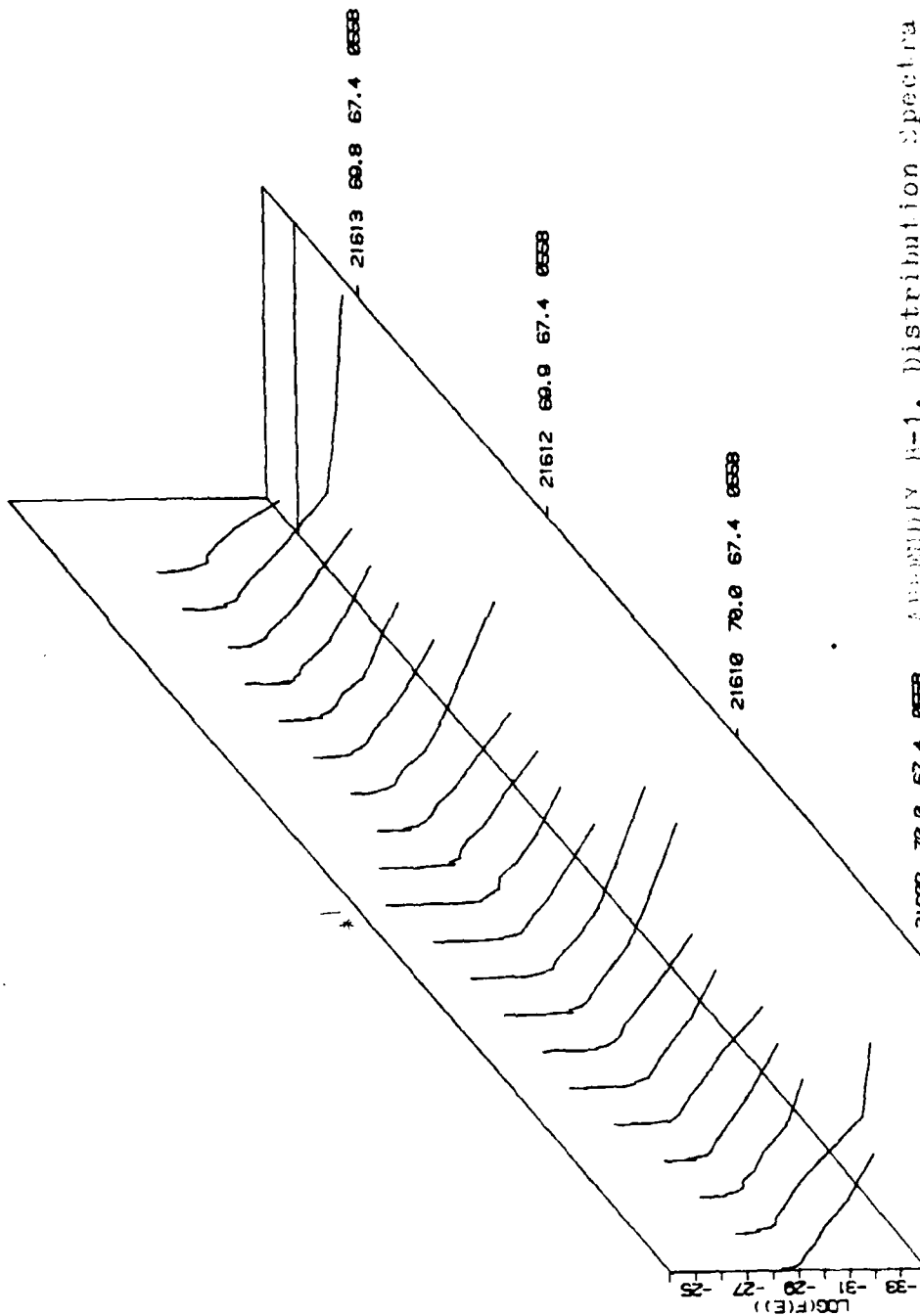
AEQY 1.51
LOG EFLX 9.03
LOG IFLX 8.85
E1= 20
E2= 632
E3= 28000



APPENDIX A-5. Distribution Spectrum: 24740 sec U.T.
21 January 1984

MODE = 3 1984 DAY 23 KP = 0

ZENITH



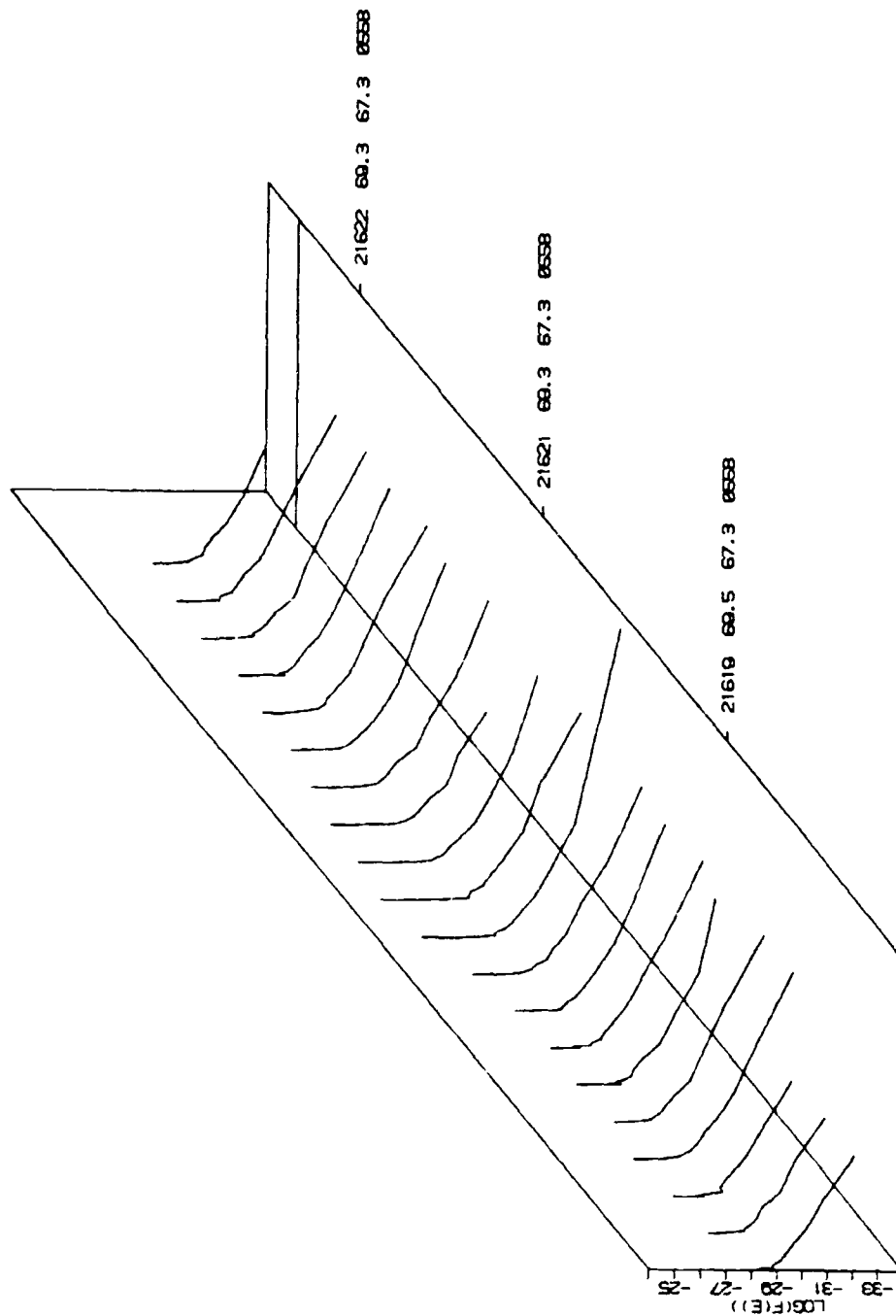
APPENDIX B-1. Distribution Spectra
21609 sec-21613 sec U.T.
23 January 1984

ENERGY (EV)

UT MAT MON GMT

MODE = 3 1984 DAY 23 KP = 0

ZENITH



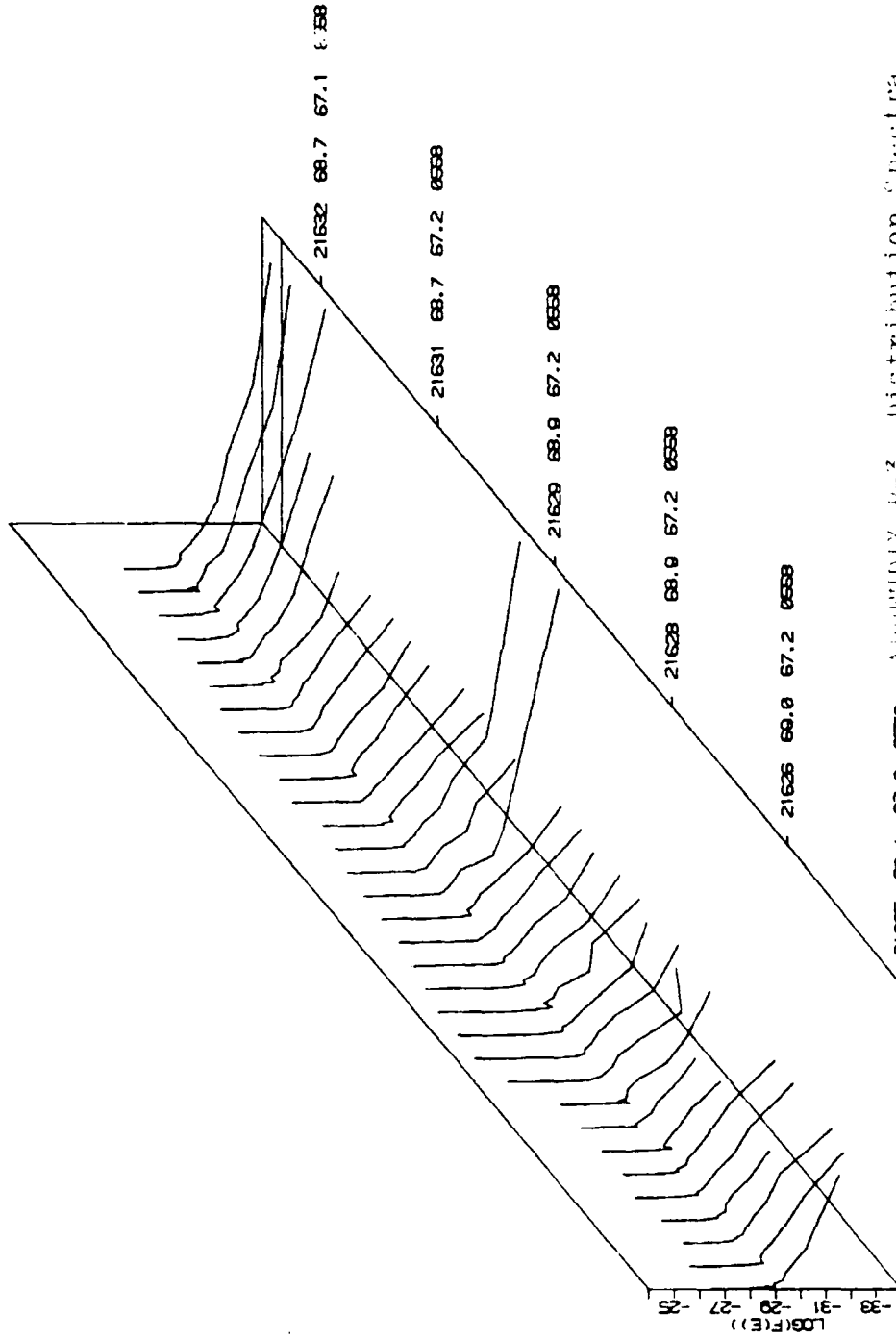
APPENDIX B-2. Distribution Spectra
21618 sec-21622 sec U.T.
23 January 1984

21618 69.5 67.3 0558
UT PLAT MLON CQFLT

ENERGY (EV)

MODE = 3 1984 DAY 23 KP = 0

ZENITH



APPENDIX B-3. Distribution Spectra
21625 sec-21632 sec U.T.
UT PLAT MLN OGLT 23 January 1984

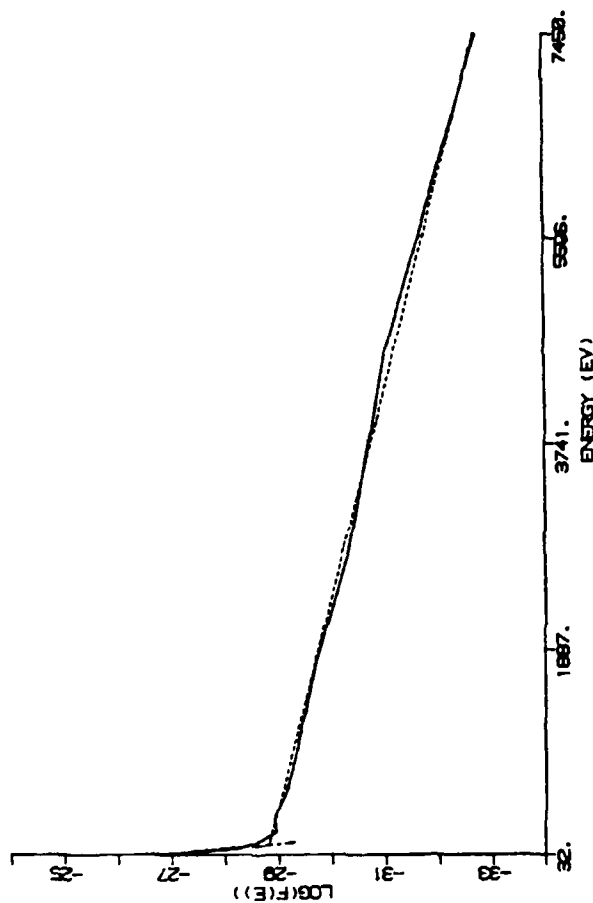
MODE = 3 1984 DAY 23 KP = 0
ZENITH

UT MLAT MLON COMPT
21626 60.0 67.2 0538

N = .40 T = .0500E+07
N = 1.10 T = .2152E+06

CHANNEL	RAW COUNTS	NUMBER	1 OF 60	DSPC	FSPC
1	26.0	5.92			26.17
2	31.0	5.70			26.50
3	11.0	5.12			27.41
4	4.0	4.45			28.27
5	5.0	4.35			28.60
6	5.0	4.21			28.95
7	17.0	4.45			29.02
8	24.0	4.44			29.16
9	51.0	4.44			29.36
10	77.0	4.44			29.67
11	91.0	4.35			30.33
12	47.0	3.90			30.90
13	24.0	3.40			32.73
14	1.0	1.03			34.00
15	.0	.00			34.00
16	.0	.00			34.00

AEQY 1.27
LOG EFLX 8.00
LOG IFLX 7.00
E1= 20
E2= 144
E3= 7450



APPENDIX B-4. Distribution Spectrum: 21626 sec U.T.
23 January 1984

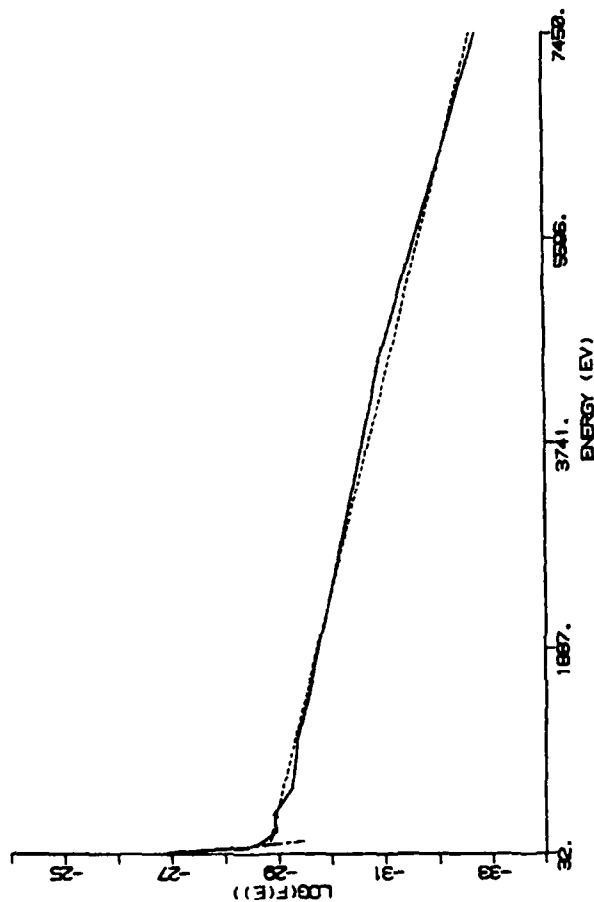
MODE = 3 1984 DAY 23 KP = 0
ZENITH

N = .49 T = .9705E+07
N = .71 T = .2104E+06

UT M/LAT M/LON OBLT
21626 60.0 67.2 8558

NUMBER 2 OF 60			
CHANNEL	RAW COUNTS	DSPC	FSPC
1	0.0	5.46	-26.63
2	16.0	5.51	-26.70
3	23.0	5.44	-27.00
4	3.0	4.34	-28.40
5	4.0	4.25	-28.70
6	16.0	4.21	-28.95
7	18.0	4.40	-28.90
8	20.0	4.34	-29.26
9	30.0	4.34	-29.26
10	81.0	4.47	-29.34
11	81.0	4.35	-29.67
12	60.0	4.07	-30.17
13	28.0	3.52	-30.93
14	1.0	1.03	-32.73
15	1.0	.00	-34.00
16	.0	.00	-34.00

REGY 1.51
LOG EFLX 9.15
LOG IFLX 7.07
E1= 28
E2= 144
E3= 7450



APPENDIX B-5. Distribution Spectrum:21626 sec U.T.
23 January 1984

MODE = 3 1984 DAY 23 KP = 0
ZENITH

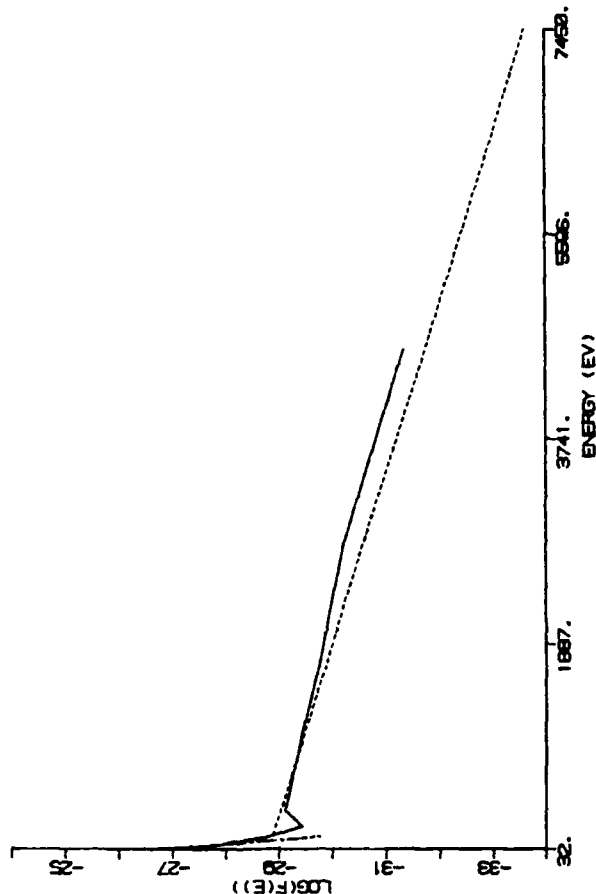
UT MLAT MLON CGALT
21626 60.0 67.2 0538

N = .33 T = .7780E+07
N = .76 T = .1937E+06

NUMBER 3 OF 60

CHANNEL	RAW COUNTS	DSPC	FSPC
1	14.0	5.65	-26.41
2	10.0	5.57	-26.72
3	15.0	4.64	-27.15
4	5.0	4.13	-28.10
5	2.0	3.74	-28.82
6	11.0	4.56	-28.11
7	12.0	4.36	-28.23
8	57.0	4.40	-28.41
9	60.0	4.27	-28.75
10	75.0	4.02	-30.22
11	61.0	3.12	-31.33
12	11.0	.00	-34.00
13	.0	.00	-34.00
14	.0	.00	-34.00
15	.0	.00	-34.00
16	.0	.00	-34.00

AEGY 1.36
LOG EFLX 8.02
LOG IFLX 7.88
E1= 20
E2= 144
E3= 7450



APPENDIX B-6. Distribution Spectrum: 21626 sec U.T.
23 January 1984

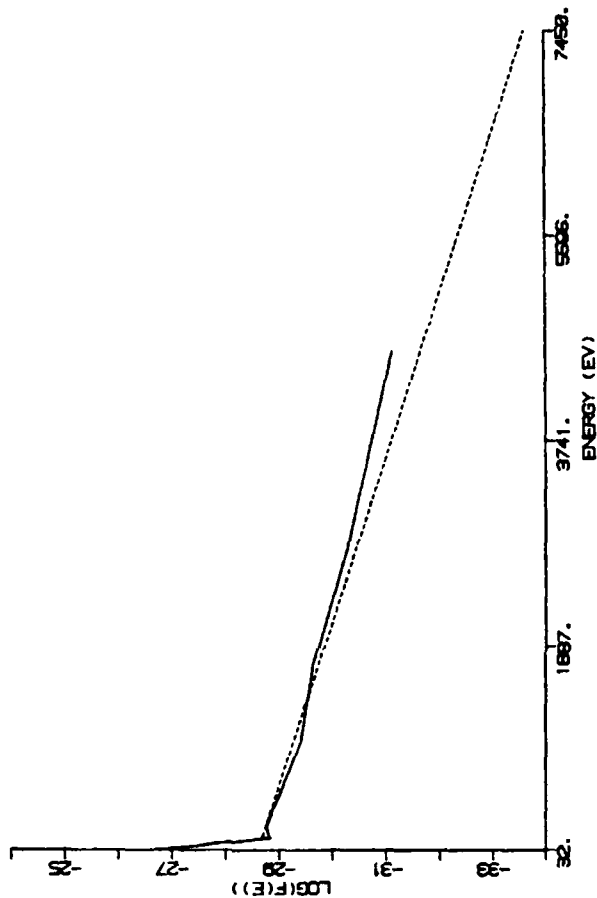
MODE = 3 1984 DAY 23 KP = 0
ZENITH

UT MLAT MLON CGMLT
21626 60.0 67.2 0658

N = .40 T = .7461E+07
N = .85 T = .2740E+06

CHANNEL	RAW COUNTS	NUMBER 4 OF 60	DSPC	FSPC
1	0.0	5.46	5.46	-28.63
2	21.0	5.62	5.62	-28.67
3	18.0	5.33	5.33	-27.19
4	13.0	4.98	4.98	-27.76
5	3.0	4.13	4.13	-28.82
6	0.0	4.39	4.39	-28.77
7	10.0	4.50	4.50	-28.88
8	24.0	4.50	4.50	-28.80
9	65.0	4.50	4.50	-28.00
10	67.0	4.38	4.38	-28.42
11	90.0	4.30	4.30	-28.63
12	51.0	3.94	3.94	-30.30
13	18.0	3.33	3.33	-31.12
14	0.0	.00	.00	-34.00
15	0.0	.00	.00	-34.00
16	0.0	.00	.00	-34.00

AEGY 1.26
LOG EFLX 8.07
LOG IFLX 7.07
E1= 20
E2= 144
E3= 7450



APPENDIX B-7. Distribution Spectrum: 21626 sec U.T.
23 January 1984

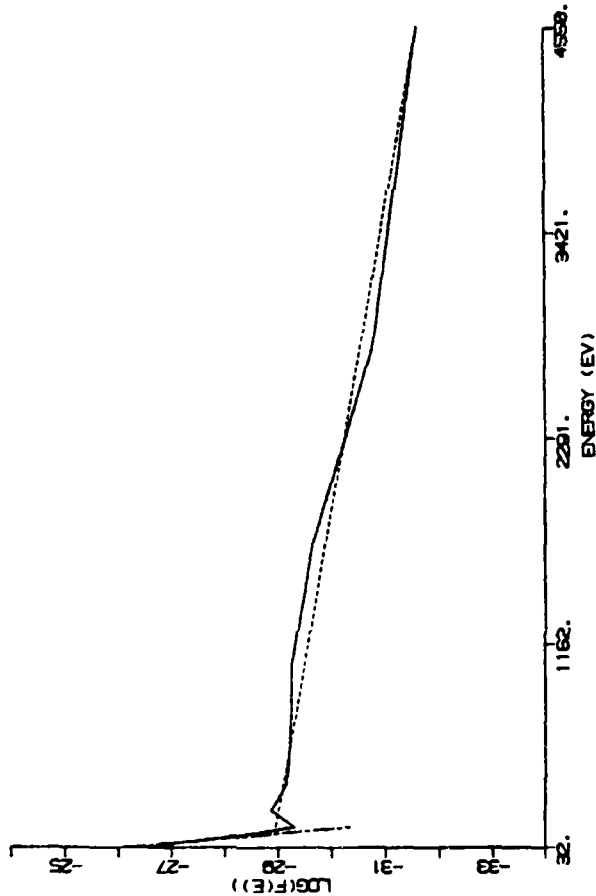
MODE = 3 1984 DAY 23 KP = 0
ZENITH

UT PLAT MUN O3PLT
21627 60.0 67.2 0550

N = .31 T = .8420E+07
N = 5.60 T = .1335E+06

CHANNEL	RAW COUNTS	NUMBER 5 OF 60	DSPC	FSPC
1	255.0	6.01	25.18	-25.63
2	27.0	5.56	-27.02	-27.02
3	27.0	4.71	-20.83	-20.83
4	1.0	3.65	-20.30	-20.30
5	7.0	4.22	-20.15	-20.15
6	18.0	4.36	-20.23	-20.23
7	18.0	4.55	-20.25	-20.25
8	47.0	4.37	-20.75	-20.75
9	90.0	3.40	-31.60	-31.60
10	95.0	2.85	-32.43	-32.43
11	18.0	2.23	-34.00	-34.00
12	6.0	.00		
13	2.0	.00		
14	.0	.00		
15	.0	.00		
16	.0	.00		

AEGY 50
LOG EFLX 7.95
LOG IFLX 8.25
E1= 20
E2= 144
E3= 4550



APPENDIX B-8. Distribution Spectrum: 21627 sec U.T.
23 January 1984

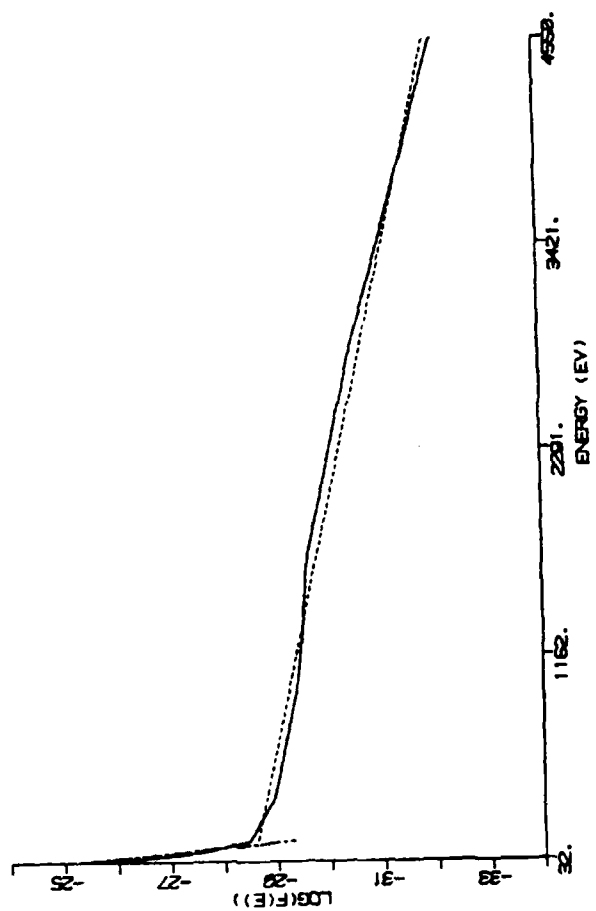
MODE = 3 1984 DAY 23 KP = 0
ZENITH

UT PLAT MLON COALT
21627 60.0 67.2 8658

N = .50 T = .6662E+07
N = 35.40 Y = .1407E+06

CHANNEL	RAW COUNTS	NUMBER	6 OF 60	DSPC	FSPC
1	1727.8	7.74			-24.35
2	470.8	6.98			-25.52
3	60.8	6.02			-26.59
4	18.8	5.12			-27.62
5	7.8	4.49			-28.65
6	12.8	4.52			-28.65
7	16.8	4.43			-28.65
8	24.8	4.46			-28.65
9	57.8	4.38			-28.62
10	67.8	4.41			-28.62
11	193.8	3.82			-30.41
12	30.8	2.38			-32.07
13	2.8	2.78			-31.88
14	7.8	.00			-34.88
15	.8	.00			-34.88
16	.8	.00			-34.88

AEGY .14
LOG EFLX 8.18
LOG IFIX 8.07
E1= 20
E2= 144
E3= 4558



APPENDIX B-9. Distribution Spectrum: 21627 sec U.T.
23 January 1984

MODE = 3 1984 DAY 23 KP = 0
ZENITH

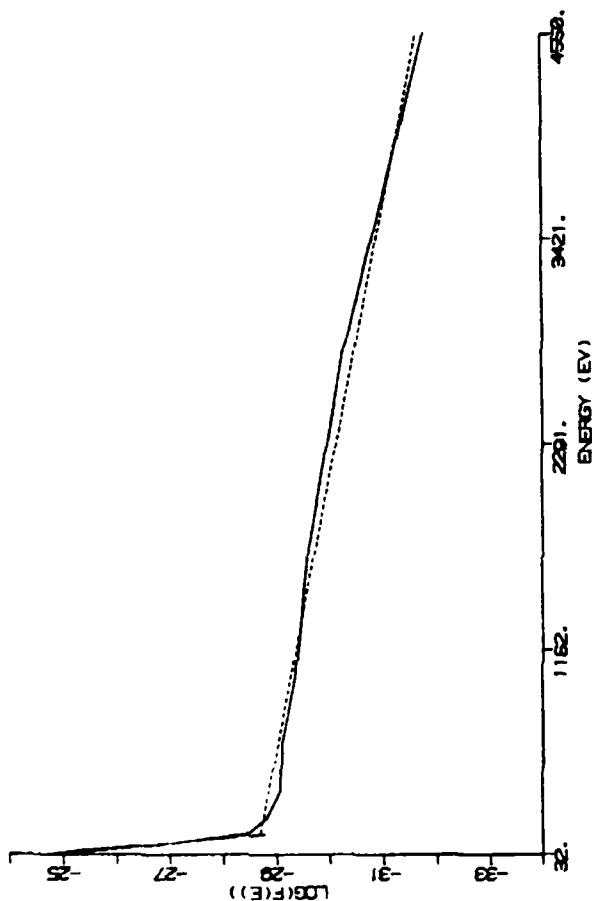
UT MLAT MLON ORALT
21627 60.0 67.2 6558

N = .40 T = .7536E+07
N = 184.68 T = .1427E+06

NUMBER 7 OF 68

CHANNEL	RAW COUNTS	DSPC	FSPC
1	927.0	7.47	-24.62
2	1685.0	7.53	-24.57
3	1467.0	7.22	-25.30
4	115.0	5.02	-26.01
5	7.0	4.40	-26.46
6	8.0	4.34	-26.82
7	12.0	4.30	-26.88
8	18.0	4.50	-26.10
9	75.0	4.50	-26.10
10	77.0	4.44	-26.36
11	187.0	4.42	-26.60
12	57.0	3.00	-30.25
13	4.0	2.68	-31.77
14	1.0	1.03	-32.73
15	.0	.00	-34.00
16	.0	.00	-34.00

AEGY .11
LOG EFLX 8.22
LOG IFLX 0.18
E1= 20
E2= 144
E3= 4550



APPENDIX B-10. Distribution Spectrum:21627 sec U.T.
23 January 1984

MODE = 3 1984 DAY 23 KP = 0
ZENITH

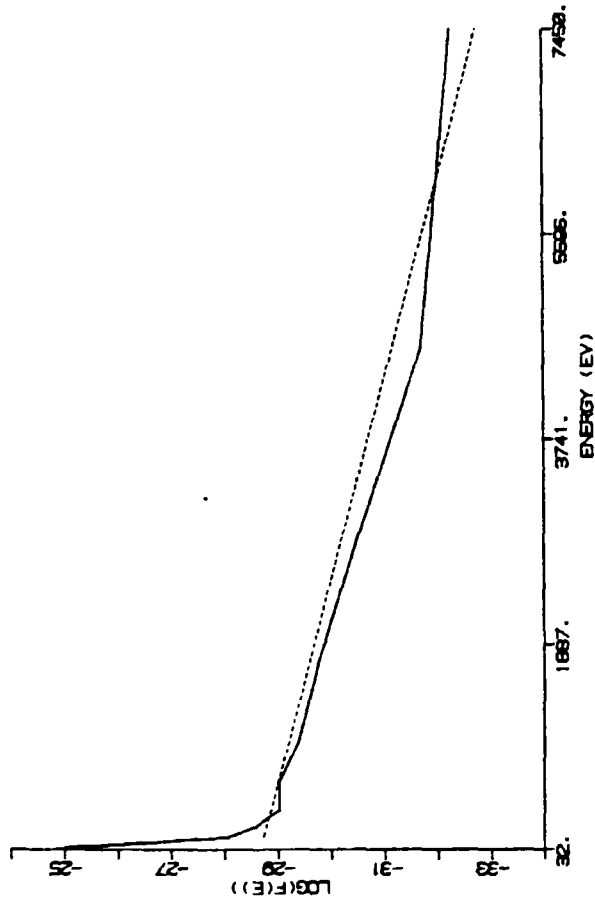
UT MLAT MLON CGALT
21627 60.0 67.2 06538

N = -58 T = .0173E+07 -----
N = 75.20 T = .1702E+06 -----

NUMBER 8 OF 60

CHANNEL	RAW COUNTS	DSPC	FSPC
1	53.0	7.24	-24.85
2	131.0	7.42	-24.88
3	2307.0	7.42	-25.10
4	355.0	6.30	-25.35
5	117.0	4.88	-28.97
6	14.0	4.59	-28.50
7	14.0	4.57	-28.01
8	28.0	4.58	-28.02
9	70.0	4.58	-28.02
10	71.0	4.41	-28.40
11	77.0	4.28	-28.74
12	35.0	3.77	-30.45
13	5.0	2.77	-31.68
14	3.0	2.41	-32.26
15	.0	.00	-34.00
16	.0	.00	-34.00

AEQY .10
LOG EFLX 8.20
LOG IFLX 0.20
E1= 20
E2= 144
E3= 7450



APPENDIX B-11. Distribution Spectrum:21627 sec U.T.
23 January 1984

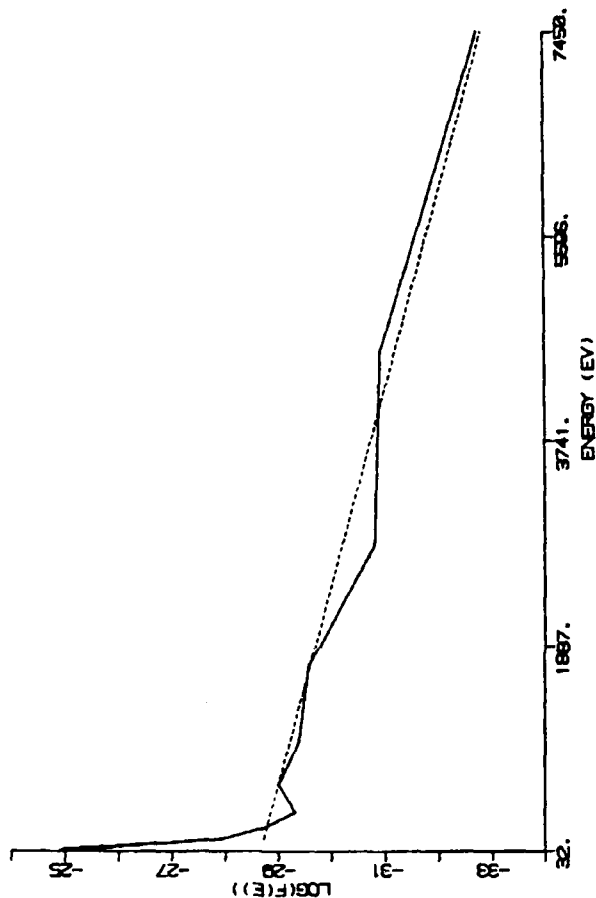
MODE = 3 1984 DAY 23 KP = 0
ZENITH

N = .58 T = .8986E+07 -----
N = 63.30 T = .1070E+06 -----

UT PLAT MLON CGMT
21628 68.9 67.2 0658

NUMBER 0 OF 60			
CHANNEL	RAW COUNTS	DSPC	FSPC
1	311.0	7.06	-25.80
2	1279.0	7.41	-24.80
3	2847.0	7.53	-24.00
4	511.0	6.57	-26.17
5	23.0	5.01	-27.04
6	11.0	4.49	-28.60
7	7.0	4.07	-28.31
8	30.0	4.59	-28.01
9	70.0	4.42	-28.01
10	73.0	4.45	-28.30
11	115.0	3.43	-28.57
12	16.0	3.43	-30.80
13	20.0	3.54	-30.01
14	1.0	1.03	-32.73
15	.0	.00	-34.00
16	.0	.00	-34.00

AEGY 11
LOG EFLX 8.30
LOG IFLX 0.24
E1= 20
E2= 144
E3= 7450



APPENDIX B-12. Distribution Spectrum:21628 sec U.T.
23 January 1984

MODE = 3 1984 DAY 23 KP = 0
ZENITH

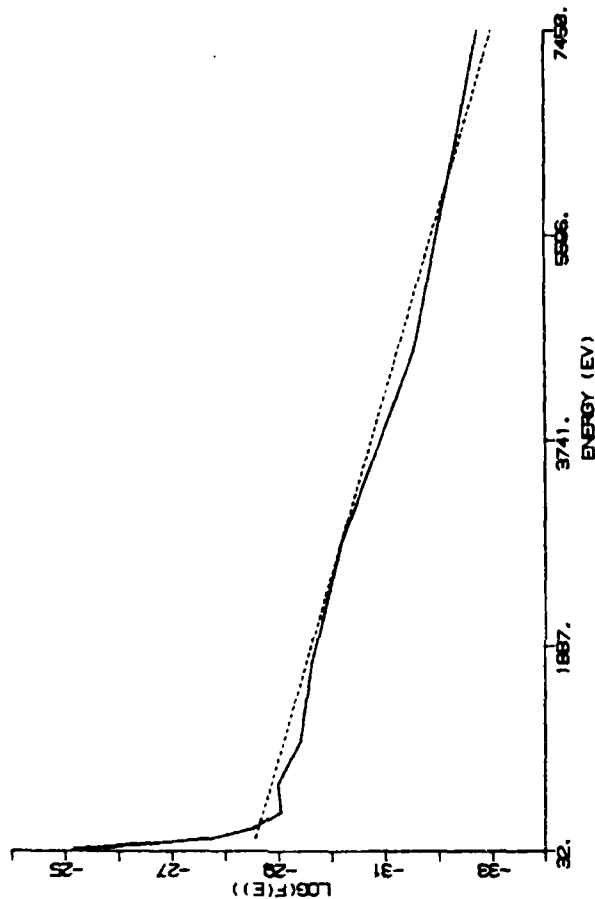
UT MLAT MLON DBLT
21628 88.9 67.2 0558

N = .75 T = .8307E+07
N = 30.22 T = .2308E+06

NUMBER 18 OF 60

CHANNEL	RAW COUNTS	DSPC	FSPC
1	247.0	6.00	-25.10
2	623.0	7.10	-25.20
3	1010.0	7.36	-25.17
4	550.0	6.61	-26.13
5	37.0	5.22	-27.73
6	16.0	4.64	-28.52
7	13.0	4.34	-28.84
8	35.0	4.61	-28.08
9	77.0	4.61	-28.08
10	60.0	4.40	-20.41
11	103.0	4.41	-20.62
12	60.0	4.07	-30.17
13	7.0	2.02	-31.53
14	1.0	1.03	-32.73
15	.0	.00	-34.00
16	.0	.00	-34.00

AEQY .15
LOG EFLX 8.26
LOG IFIX 8.60
E1 = 20
E2 = 144
E3 = 7450



APPENDIX B-13. Distribution Spectrum:21628 sec U.T.
23 January 1984

MODE = 3 1984 DAY 23 KP = 0
ZENITH

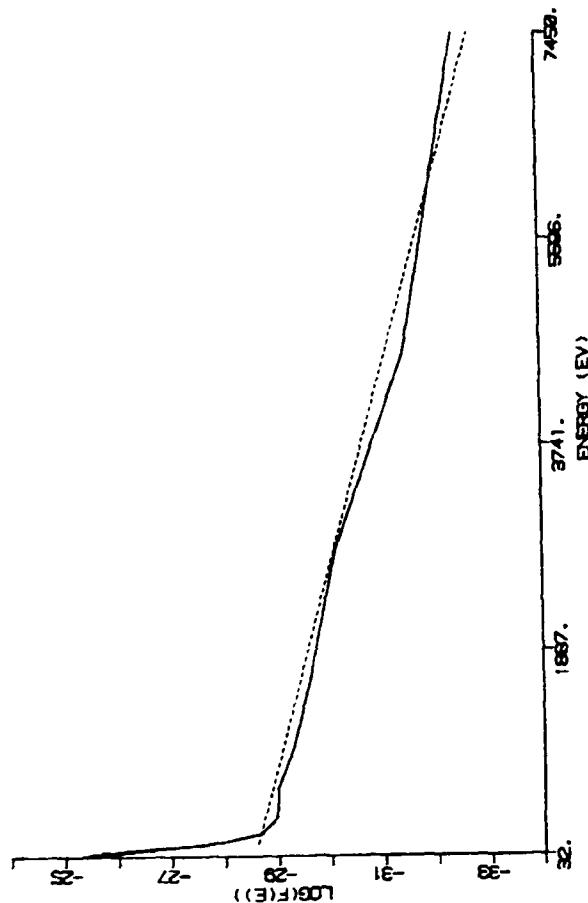
N = .75 T = .8025E+07
N = 26.85 T = .2380E+06

UT MLAT MLON ORMLT
21628 88.0 67.2 08538

NUMBER 11 OF 50

CHANNEL	RAW COUNTS	DSPC	FSPC
1	210.0	6.85	-25.25
2	455.0	6.06	-25.34
3	863.0	7.01	-25.51
4	431.0	6.50	-26.24
5	35.0	5.10	-27.76
6	11.0	4.48	-28.60
7	15.0	4.40	-28.08
8	35.0	4.61	-28.08
9	77.0	4.61	-28.08
10	60.0	4.51	-28.30
11	95.0	4.37	-28.65
12	77.0	4.12	-30.12
13	9.0	3.03	-31.42
14	2.0	2.23	-32.43
15	.0	.00	-34.00
16	.0	.00	-34.00

AEQY .22
LOG EFLX 8.23
LOG IFLX 8.68
E1 = 20
E2 = 144
E3 = 7450



APPENDIX B-14. Distribution Spectrum: 21628 sec U.T.
23 January 1984

MODE = 3 1984 DAY 23 KP = 0
ZENITH

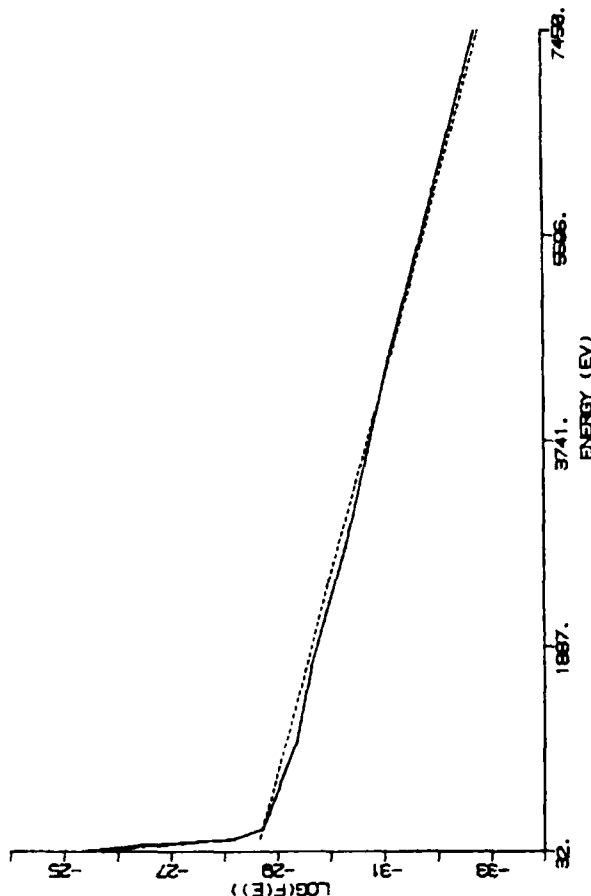
UT MLAT MLON CQPLT
21628 68.0 67.2 0558

N = .65 T = .8875E+07
N = 28.39 T = .2072E+06

NUMBER 12 OF 60

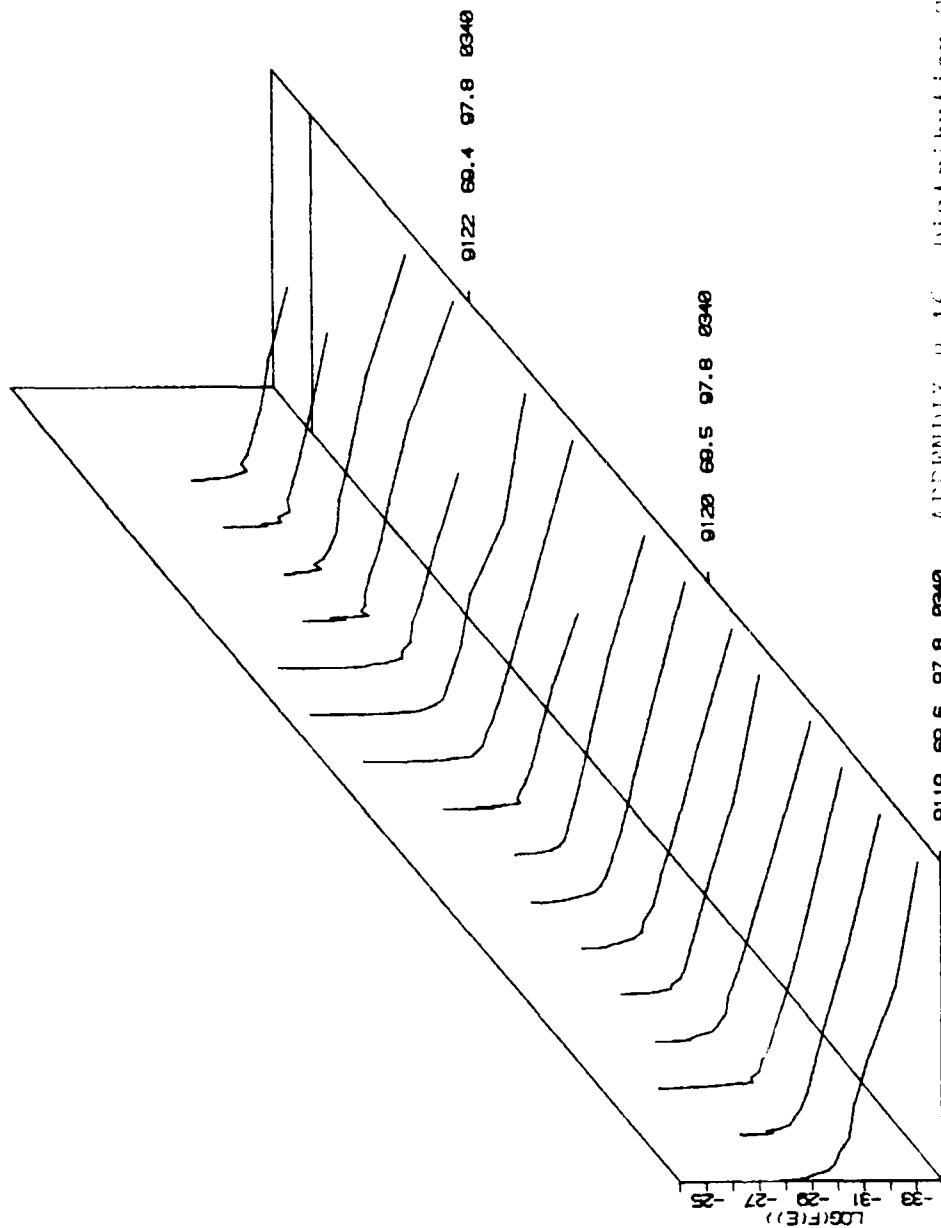
CHANNEL	RAW COUNTS	DSPC	FSPC
1	231.0	6.97	-25.22
2	219.0	6.94	-25.66
3	243.0	6.91	-26.71
4	270.0	6.31	-26.43
5	13.0	4.76	-28.10
6	18.0	4.44	-28.73
7	20.0	4.22	-28.85
8	26.0	4.26	-28.84
9	77.0	4.56	-28.36
10	90.0	4.50	-28.50
11	51.0	3.94	-31.12
12	18.0	1.83	-32.73
13	1.0	1.00	-34.00
14	.0	.00	-34.00
15	.0	.00	-34.00
16	.0	.00	-34.00

AEGY .28
LOG EFLX 8.16
LOG IFLX 8.71
E1= 20
E2= 144
E3= 7450



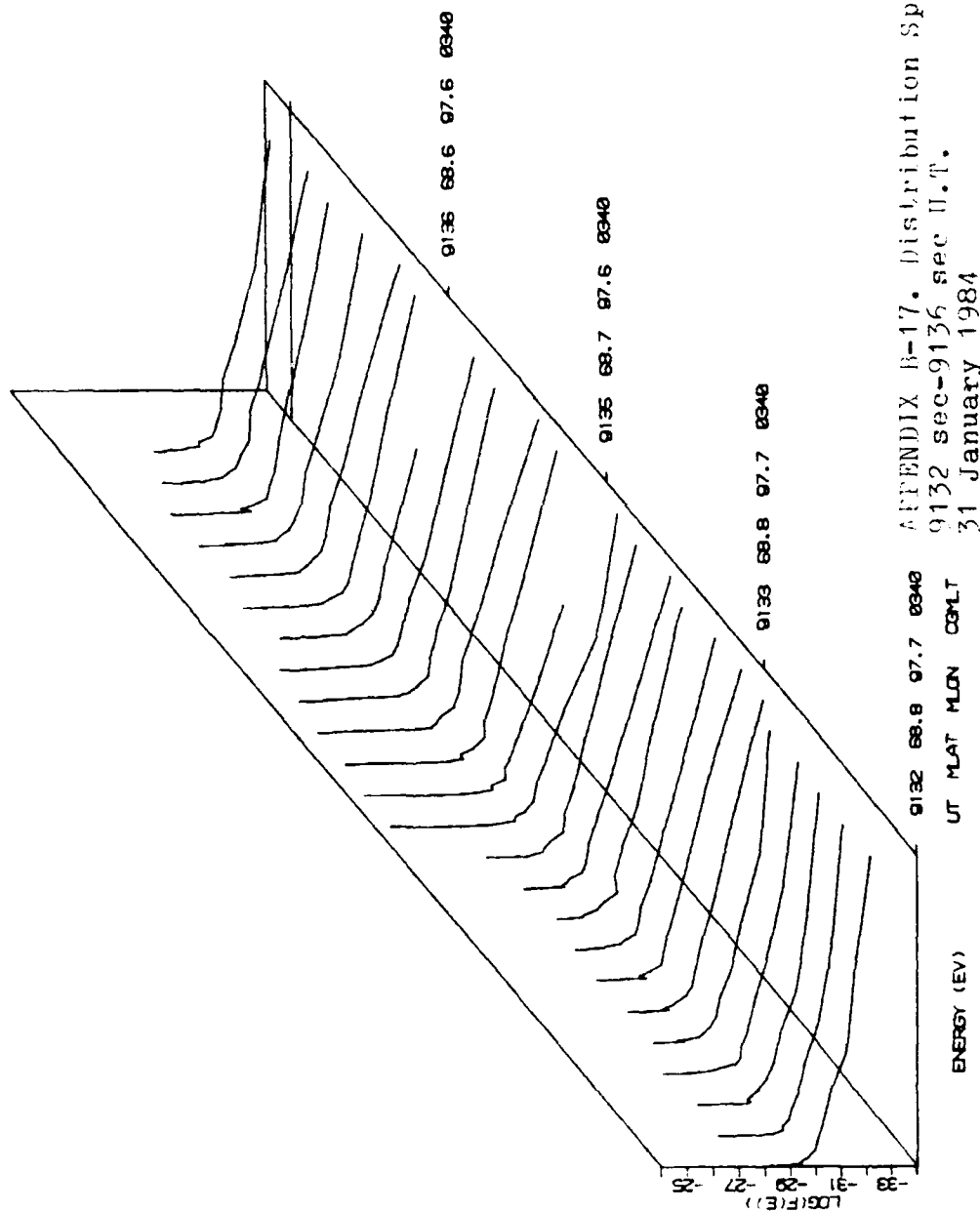
APPENDIX P-15. Distribution Spectrum: 21628 sec U.T.
23 January 1984

MILINER

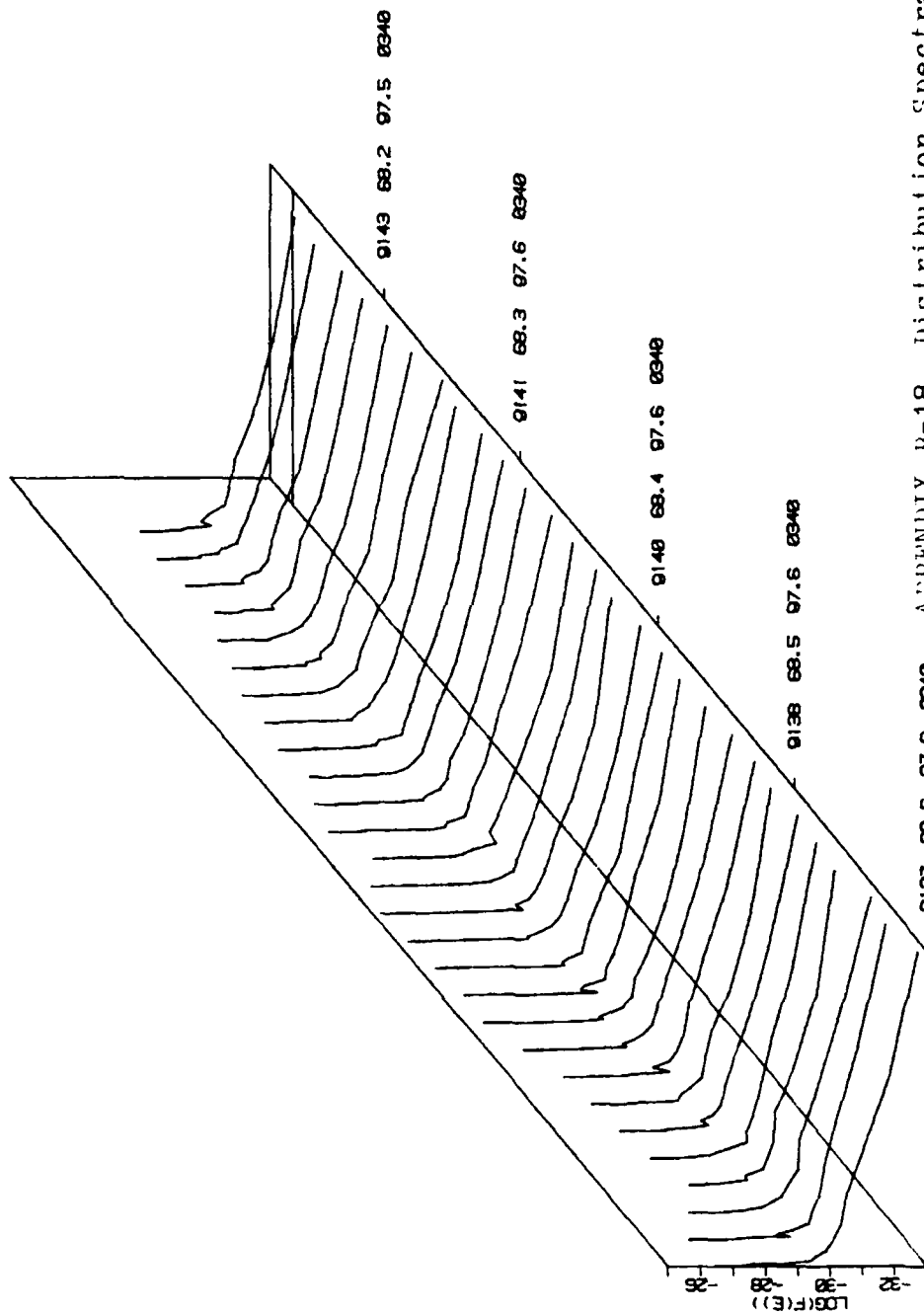


9119 69.6 97.8 8340
UT MLAT MLON CGLT 9119 69.6 97.8 8340
ENERGY (EV) UT MLAT MLON CGLT 9119 69.6 97.8 8340
APPENDIX B-16. Distribution Spectra
9119 69.6 97.8 8340
- 31 January 1984

MODE = 3 1984 DAY 31 KP = 0
ZENITH

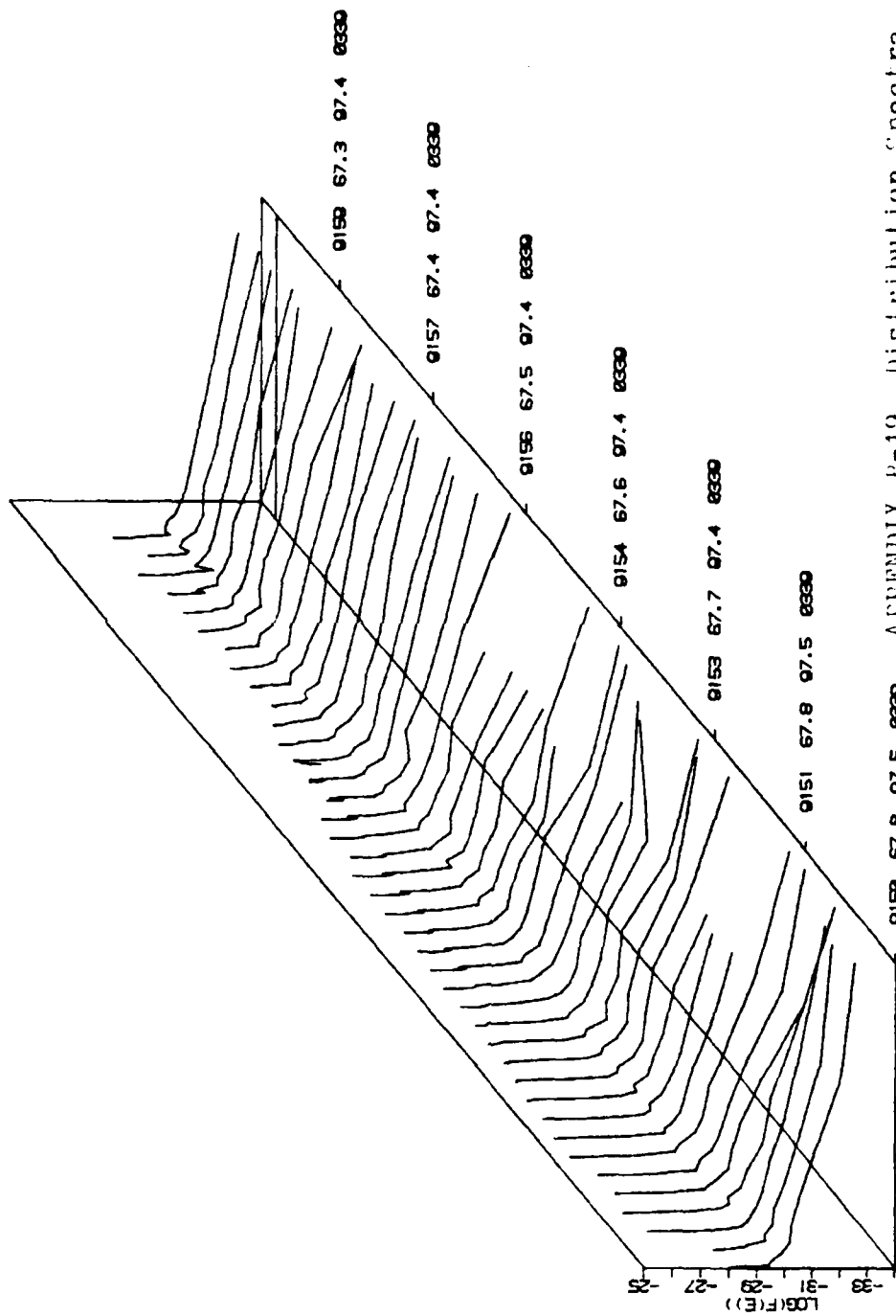


MODE = 3 1984 DAY 31 KP = 0
ZENITH



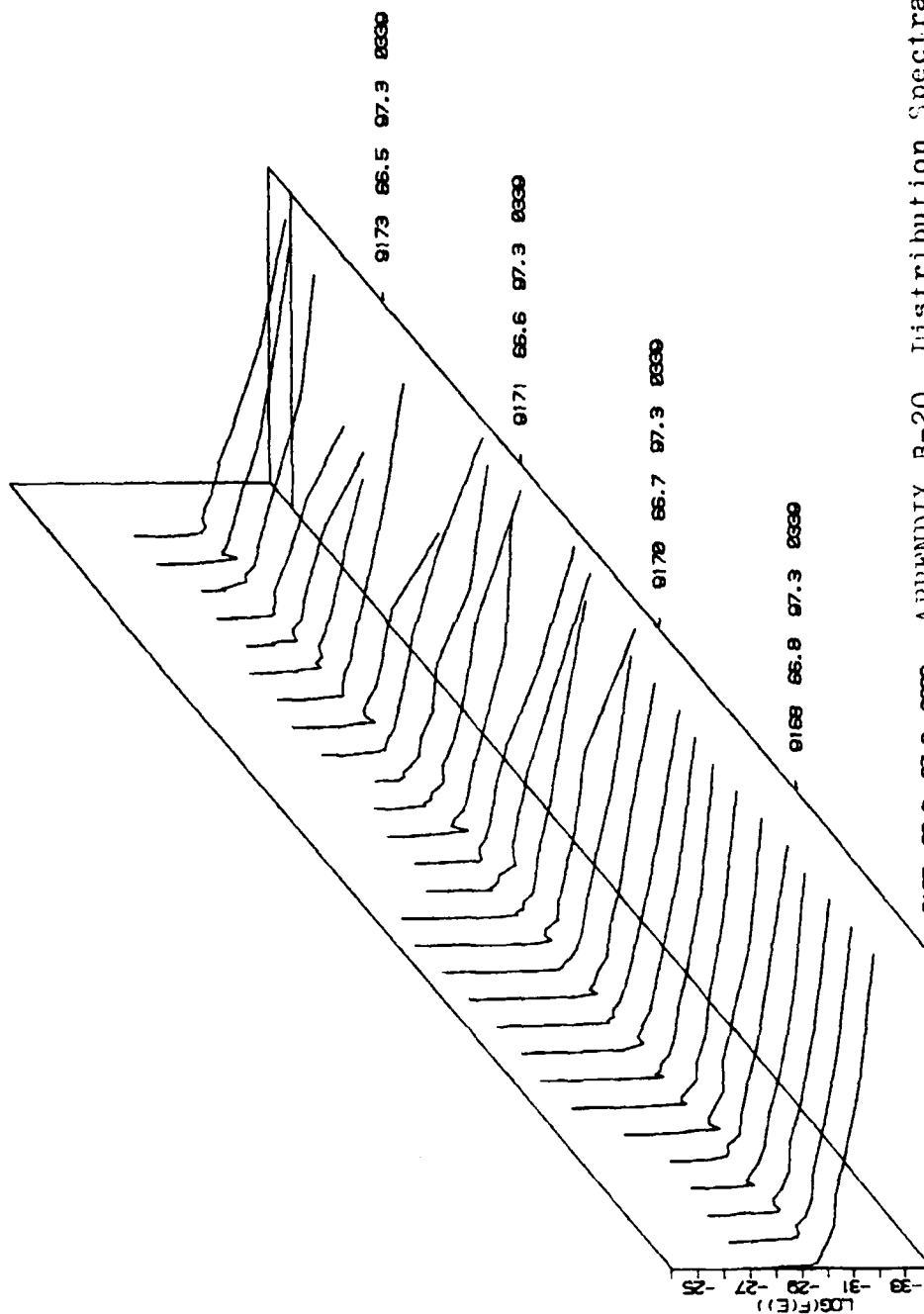
APPENDIX B-18. Distribution Spectra
9137 sec-9143 sec U.T.
31 January 1984

MODE = 3 1984 DAY 31 KP = 0
ZENITH



APPENDIX B-19. Distribution Spectra
9150 sec-9159 sec U.T.
31-January 1984

MODE = 3 1984 DAY 31 KP = 0
ZENITH



APPENDIX B-20. Distribution Spectra
9167 sec=9173 sec U.T.
31 January 1984
UT MLAT MLON DGLT

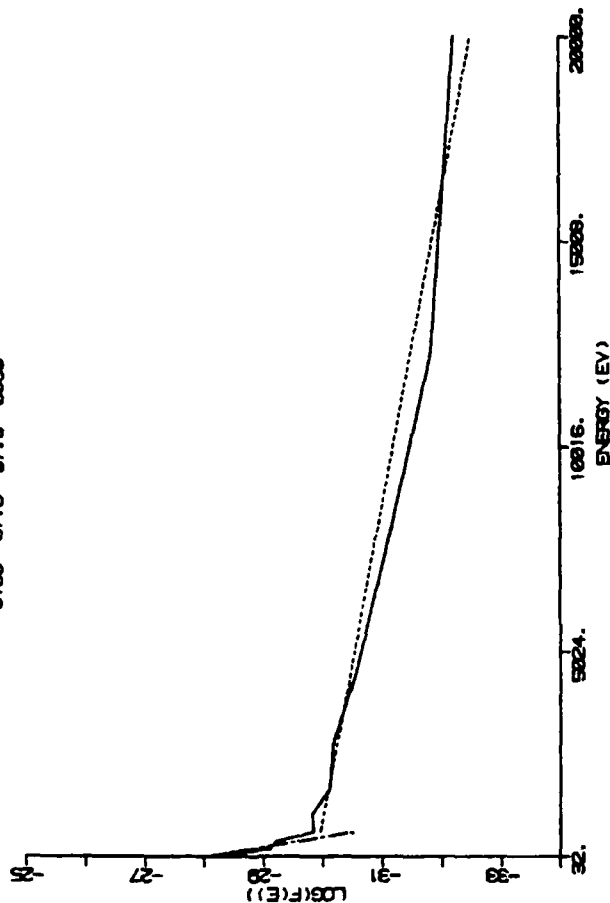
MODE = 3 1984 DAY 31
ZENITH

UT MLAT MLON C3PLT
0150 67.8 97.5 8330

N = .30 T = .3950E+08
N = .16 T = .1227E+07

CHANNEL	RAW COUNTS	DSPC	ESPC
1	1.0	4.51	-27.50
2	1.0	4.30	-28.00
3	9.0	0.90	-34.00
4	3.0	4.34	-28.40
5	4.0	4.25	-28.70
6	4.0	4.04	-28.12
7	9.0	4.18	-20.20
8	2.0	3.76	-20.83
9	16.0	3.76	-20.82
10	27.0	3.00	-30.11
11	33.0	3.01	-30.17
12	69.0	4.07	-30.56
13	65.0	3.80	-31.05
14	47.0	3.68	-31.88
15	10.0	2.80	-32.21
16	16.0	2.80	-32.21

AEQY 5.56
LOG EFLX 8.68
LOG IFLX 7.03
E1= 20
E2= 632
E3= 20000



12

APPENDIX B-21. Distribution Spectrum: 9150 sec U.T.
31 January 1984

MODE = 3 1984 DAY 31
ZENITH

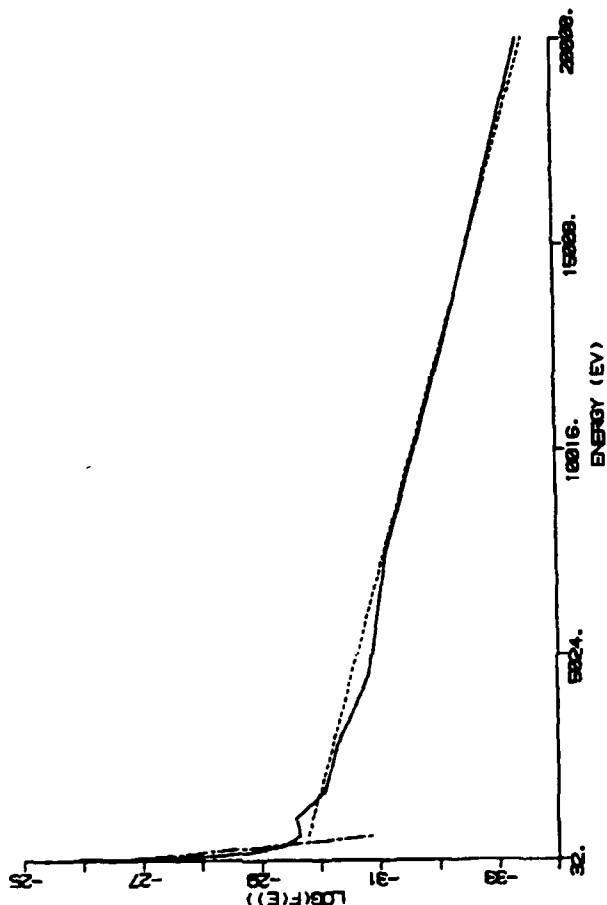
UT MLAT MLON COSLT
9150 57.8 97.5 03600

N = .28 T = .2615E+08
N = 2.26 T = .7815E+06

NUMBER 4 OF 60

CHANNEL	RAW COUNTS	DSPC	FSPC
1	24.8	5.89	26.21
2	193.8	6.31	255.08
3	355.8	6.68	2355.02
4	37.8	5.43	227.31
5	0.8	4.68	226.25
6	0.8	4.34	228.82
7	6.8	4.88	220.36
8	0.8	3.88	220.63
9	17.8	3.86	220.63
10	47.8	4.23	228.82
11	32.8	3.87	228.82
12	25.8	3.87	228.82
13	25.8	3.87	228.82
14	41.8	2.84	22.84
15	1.8	1.88	22.84
16	1.8	1.88	22.84

AEGY 1.17
LOG EFLX 8.44
LOG IFLX 8.37
E1= 20
E2= 832
E3= 20000



APPENDIX B-22. Distribution Spectrum: 9150 sec U.T.
31 January 1984

MODE = 3 1984 DAY 31

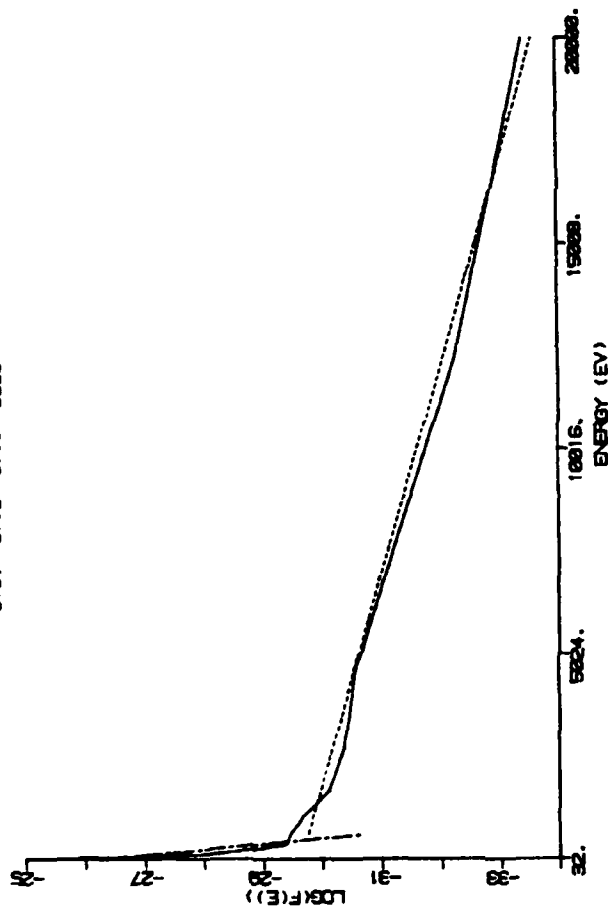
ZENITH

UT 0151 MLAT 67.8 CLON 0830

N = .28 T = .2545E+08
N = 3.06 T = .7821E+06

CHANNEL	RAW COUNTS	DSPC	FSPC
1	70.0	6.40	25.60
2	100.0	6.60	26.70
3	343.0	6.61	25.91
4	71.0	5.71	27.62
5	16.0	4.85	28.18
6	12.0	4.52	28.65
7	16.0	4.00	29.38
8	16.0	4.14	29.45
9	30.0	4.15	29.66
10	33.0	3.91	30.11
11	43.0	3.86	30.37
12	65.0	3.80	31.19
13	35.0	3.47	31.23
14	7.0	2.64	32.23
15	1.0	1.68	33.41

AEQY .80
LOG EFLX 8.44
LOG IFLX 8.40
E1 = 20
E2 = 632
E3 = 20000



APPENDIX B-23. Distribution Spectrum:9151 sec U.T.
31 January 1984

MODE = 3 1984 DAY 31
ZENITH

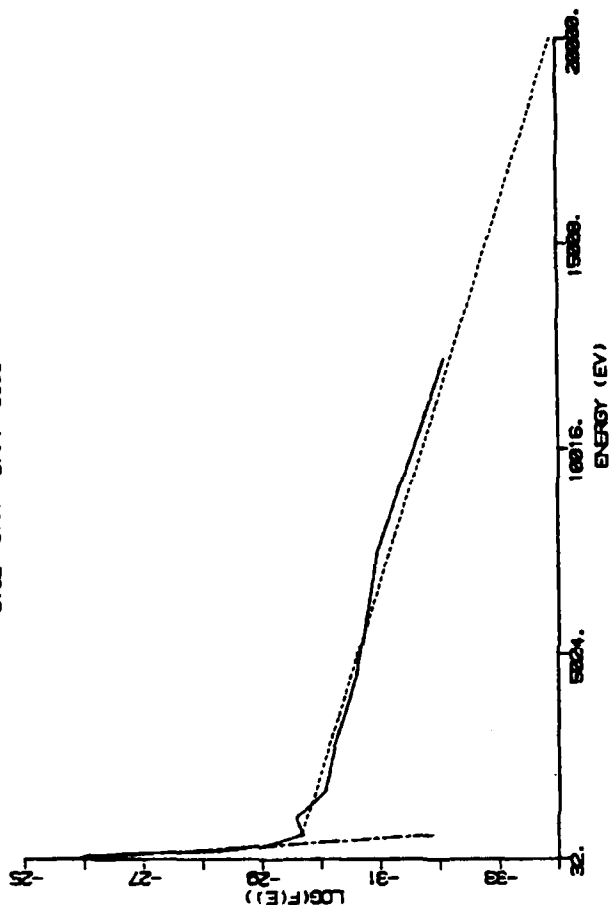
UT MLAT MLON ORBIT
9152 67.7 67.4 0300

N = .31 T = .2302E+08
N = 13.71 T = .4871E+06

NUMBER 10 OF 60

CHANNEL	RAW COUNTS	DSPC	FSPC
1	17.0	6.26	25.83
2	147.0	6.47	22.83
3	310.0	6.50	22.04
4	751.0	6.74	22.00
5	1193.0	6.72	22.23
6	26.0	4.55	20.31
7	11.0	3.06	20.11
8	15.0	3.01	20.50
9	17.0	3.01	20.50
10	47.0	4.73	20.50
11	37.0	3.85	20.22
12	51.0	4.82	20.50
13	50.0	3.95	20.55
14	61.0	3.72	20.55
15	10.0	2.60	20.50
16	9.0	2.60	20.50

MEGY .47
LOG EFLX 8.63
LOG IFLX 8.95
E1= 20
E2= 632
E3= 20000



APPENDIX B-24. Distribution Spectrum:9152 sec U.T.
31 January 1984

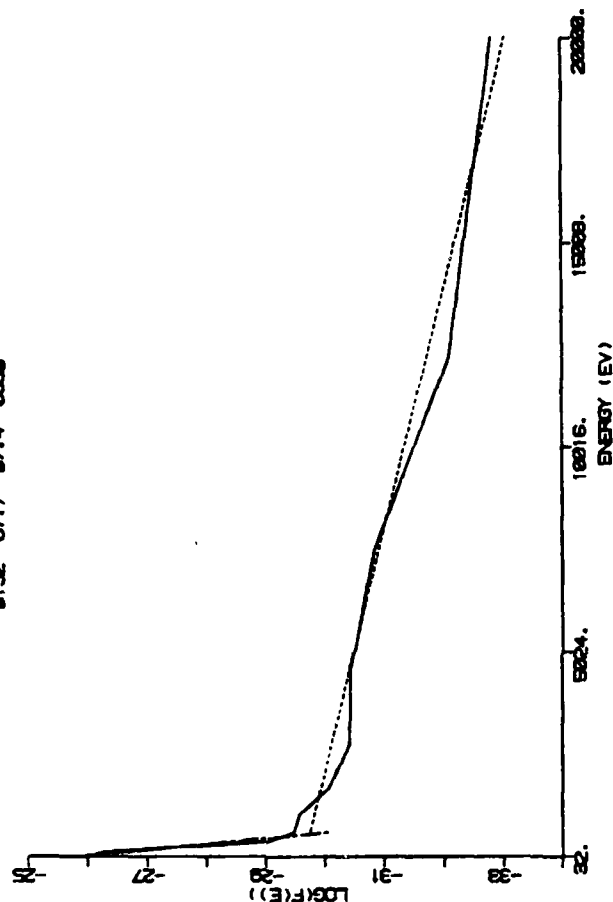
MODE = 3 1984 DAY 31
ZENITH

UT MLAT MLON OBLT
9152 67.7 97.4 0000

N = .34 T = .2062E+08
N = 12.08 T = .7127E+06

NUMBER 12 OF 68			
CHANNEL	RAW COUNTS	DSPC	FSPC
1	95.0	6.48	-26.61
2	57.0	6.06	-26.24
3	239.0	6.45	-26.07
4	543.0	6.68	-26.14
5	1855.0	6.67	-26.28
6	471.0	6.11	-27.05
7	14.0	4.37	-20.01
8	8.0	4.11	-20.48
9	38.0	4.11	-20.48
10	40.0	4.25	-20.56
11	37.0	3.06	-30.06
12	30.0	3.82	-30.41
13	87.0	4.02	-30.43
14	70.0	3.83	-30.84
15	10.0	2.68	-32.08
16	4.0	2.20	-32.81

AGEY .69
LOG EFLX 8.73
LOG IFIX 8.06
E1= 28
E2= 632
E3= 20000



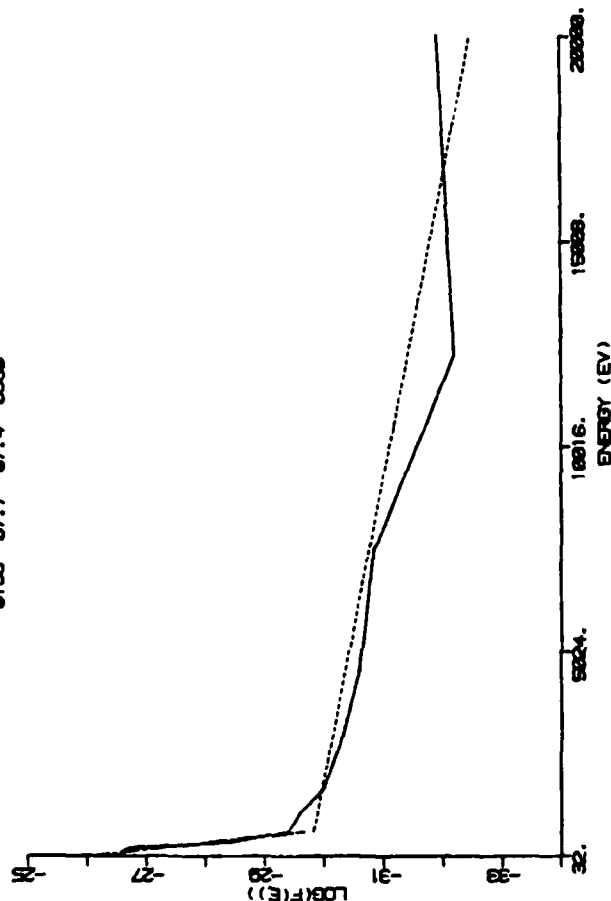
APPENDIX B-25. Distribution Spectrum:9152 sec U.T.
31 January 1984

MODE = 3 1984 DAY 31
ZENITH

UT PLAT MLON OGRLT
9153 67.7 97.4 8330

N = .30 T = .3680E+08
N = 10.37 T = .8306E+06

CHANNEL	RAW COUNTS	NUMBER 14 OF 68	DSPC	FSPC
1	111.0	6.55	25.54	25.54
2	65.0	6.11	26.18	26.18
3	77.0	6.06	26.56	26.56
4	207.0	6.10	26.56	26.56
5	511.0	6.36	26.56	26.56
6	1823.0	6.45	26.56	26.56
7	45.0	4.88	26.56	26.56
8	11.0	4.10	26.56	26.56
9	33.0	4.25	26.56	26.56
10	40.0	4.63	26.56	26.56
11	43.0	3.07	26.56	26.56
12	52.0	3.06	26.56	26.56
13	61.0	3.03	26.56	26.56
14	70.0	3.17	26.56	26.56
15	8.0	3.17	26.56	26.56
16	31.8	3.17	26.56	26.56
MEGY	.04			
LOG IFIX	8.66			
LOG IFLX	8.66			
E1 =	20			
E2 =	832			
E3 =	20000			



APPENDIX B-26. Distribution Spectrum:9153 sec U.T.
31 January 1984

MODE = 3 1984 DAY 31

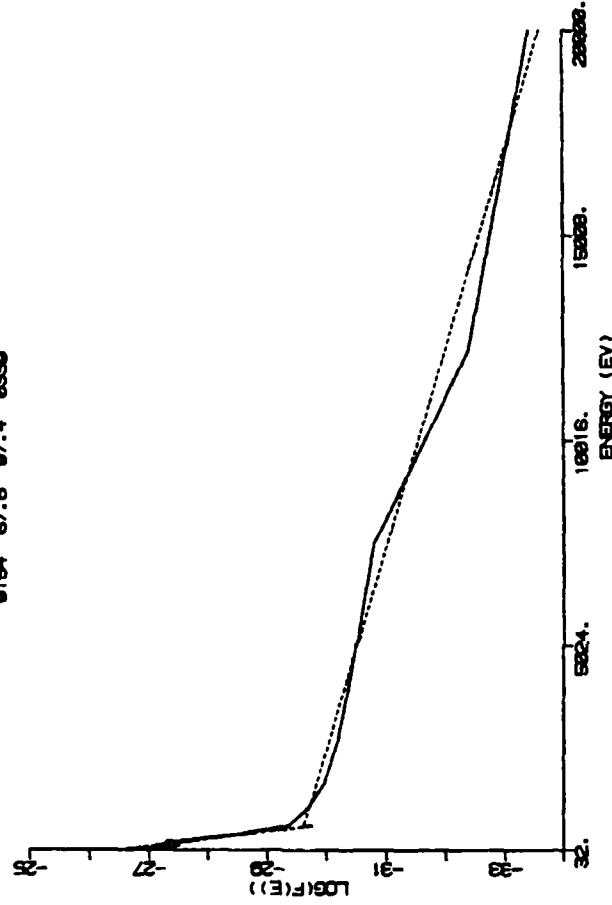
ZENITH

UT PLAT MLON OGRLT
9154 67.6 97.4 8830

N = .36 T = .2461E+08
N = 3.73 T = .9371E+06

CHANNEL	RAW COUNTS	DSPC	FSPC
1	71.0	6.36	-26.74
2	45.0	5.05	-26.34
3	38.0	5.55	-26.07
4	31.0	5.43	-27.38
5	61.0	5.87	-27.52
6	271.0	4.09	-27.20
7	59.0	4.23	-28.38
8	22.0	4.13	-28.37
9	19.0	4.05	-28.68
10	37.0	4.83	-28.21
11	45.0	4.83	-30.08
12	63.0	4.83	-30.44
13	85.0	3.87	-30.70
14	87.0	3.58	-32.38
15	5.0	1.68	-33.41
16	1.0		

MEBY 1.68
LOG EFLX 8.68
LOG IFLX 8.45
E1= 20
E2= 632
E3= 20000



APPENDIX B-27. Distribution Spectrum: 9154 sec U.T.
31 January 1984

MODE = 3 1984 DAY 31
ZENITH

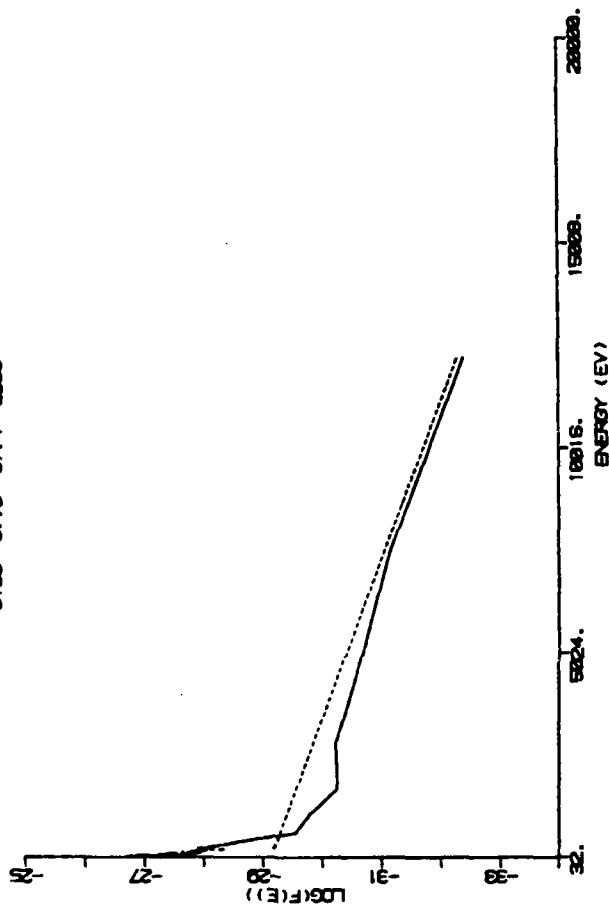
UT MLAT MLON CQRLT
9155 67.5 97.4 8339

N = .61 T = .1940E+08
N = 1.68 T = .6224E+06

NUMBER 23 OF 68

CHANNEL	RAW COUNTS	DSPC	FSPC
1	37.0	6.07	-26.92
2	17.0	5.53	-26.77
3	49.0	5.77	-26.76
4	13.0	4.08	-27.76
5	22.0	4.99	-27.08
6	67.0	5.26	-27.00
7	41.0	4.84	-28.54
8	0.0	4.85	-28.55
9	22.0	4.85	-28.76
10	31.0	4.85	-28.22
11	24.0	3.77	-30.25
12	61.0	4.02	-30.22
13	61.0	3.86	-30.50
14	30.0	3.52	-31.14
15	5.0	2.50	-32.39
16	0.0	0.00	-34.00

AEGY 1.85
LOG EFLX 8.43
LOG IFLX 8.16
E1 = 28
E2 = 235
E3 = 20000



APPENDIX B-28. Distribution Spectrum: 9156 sec U.T.
31 January 1984

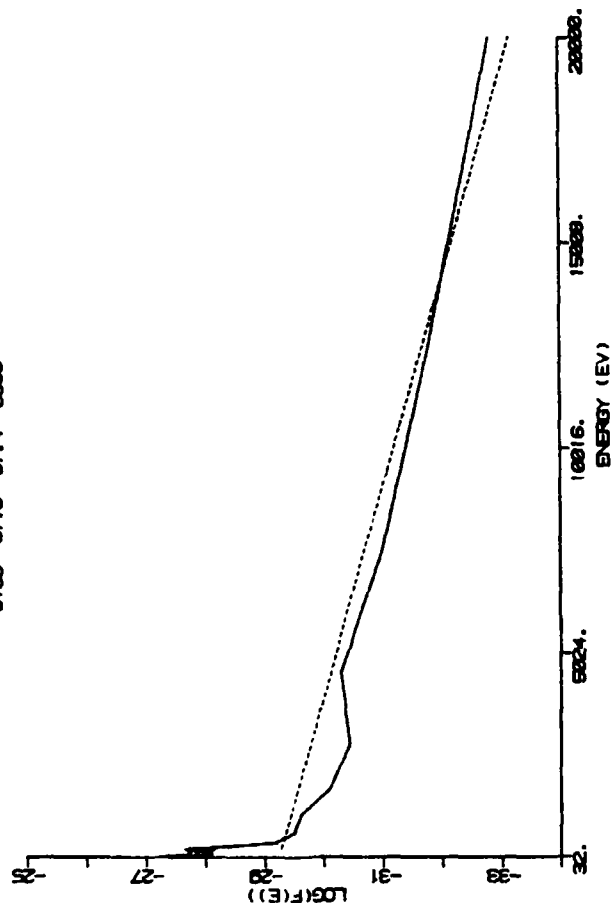
MODE = 3 1984 DAY 31
ZENITH

UT MLAT MLON OBLT
0156 67.5 07.4 0030

N = .71 T = .2570E+08
N = .00 T = .1152E+07

CHANNEL	RAW COUNTS	DSPC	FSPC
1	27.0	5.91	-26.15
2	3.0	4.70	-27.52
3	8.0	4.08	-27.55
4	16.0	4.67	-28.10
5	110.0	4.85	-28.10
6	9.0	5.51	-27.55
7	8.0	4.18	-28.50
8	28.0	4.60	-28.50
9	45.0	4.21	-28.50
10	33.0	3.91	-28.11
11	37.0	3.80	-28.44
12	110.0	4.15	-28.30
13	55.0	3.67	-28.90
14	22.0	3.14	-31.74
15	4.0	2.20	-32.81

AEBY 3.12
LOG EFLX 8.68
LOG IFLX 8.10
E1= 28
E2= 235
E3= 20000



APPENDIX B-29. Distribution Spectrum: 9156 sec U.T.
31 January 1984

MODE = 3 1984 DAY 31
ZENITH

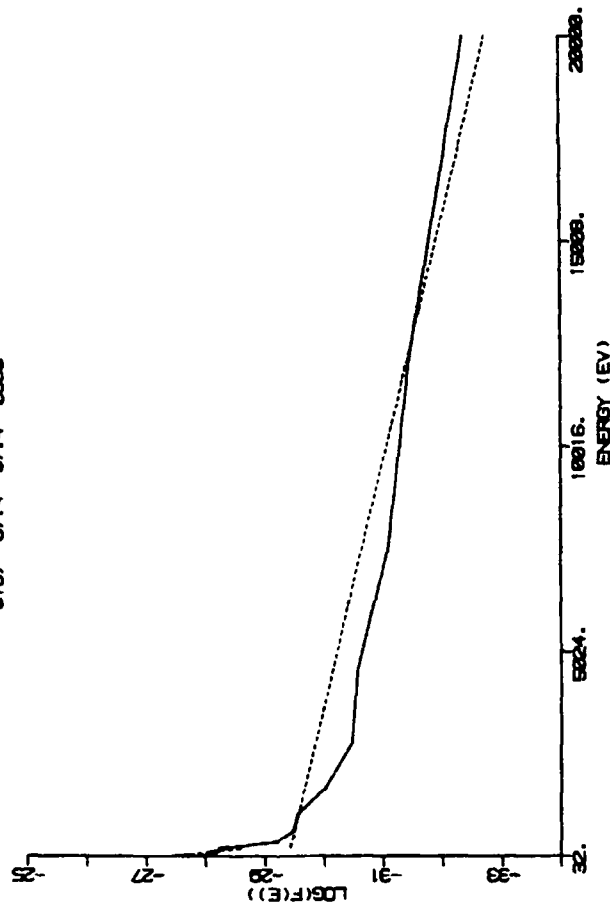
UT PLAT MLON CGALT
9157 67.4 97.4 0000

N = .63 T = .3007E+09
N = .43 T = .0002E+06

NUMBER 20 OF 60

CHANNEL	RAW COUNTS	DSPC	FSPC
1	10.0	5.51	-26.50
2	3.0	4.79	-27.52
3	3.0	4.55	-27.07
4	12.0	4.73	-28.17
5	3.0	4.03	-28.22
6	0.0	4.19	-28.24
7	0.0	4.13	-28.20
8	35.0	4.13	-28.46
9	51.0	4.27	-28.54
10	41.0	4.61	-28.62
11	35.0	3.77	-28.58
12	65.0	3.80	-30.58
13	45.0	3.58	-31.00
14	43.0	3.43	-31.45
15	11.0	2.72	-32.37

AEQY 4.86
LOG EFLX 8.73
LOG IFLX 8.84
E1= 20
E2= 235
E3= 20000



APPENDIX B-30. Distribution Spectrum: 9157 sec U.T.
31 January 1984

MODE = 3 1984 DAY 31
ZENITH

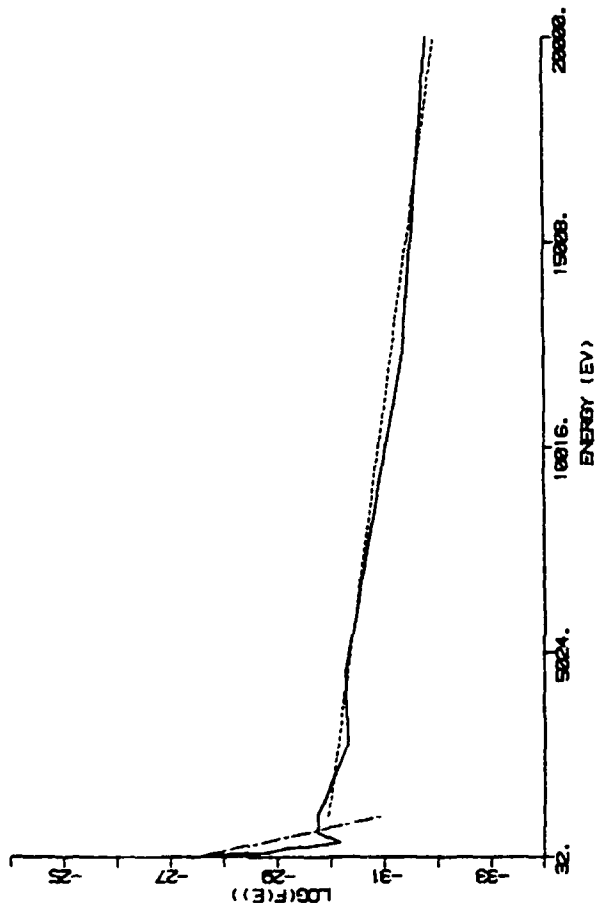
UT MLAT MLON CGALT
9168 66.8 97.3 8839

N = .45 T = .4758E+08
N = .65 T = .1467E+07

NUMBER 2 OF 68

CHANNEL	RAW COUNTS	DSPC	FSPC
1	31.0	8.08	-26.80
2	29.0	8.75	-26.55
3	6.0	4.02	-27.08
4	6.0	4.64	-26.18
5	3.0	4.13	-26.02
6	4.0	4.01	-26.12
7	7.0	3.22	-26.15
8	11.0	3.83	-26.75
9	33.0	4.06	-26.73
10	47.0	4.06	-26.66
11	51.0	3.94	-26.59
12	127.0	4.18	-26.27
13	115.0	3.90	-26.67
14	57.0	3.55	-31.32
15	41.0	3.39	-31.00

AEGY 6.37
LOG EFLX 9.03
LOG IFLX 8.23
E1 = 20
E2 = 1835
E3 = 20000



APPENDIX B-31. Distribution Spectrum:9168 sec U.T.
31 January 1984

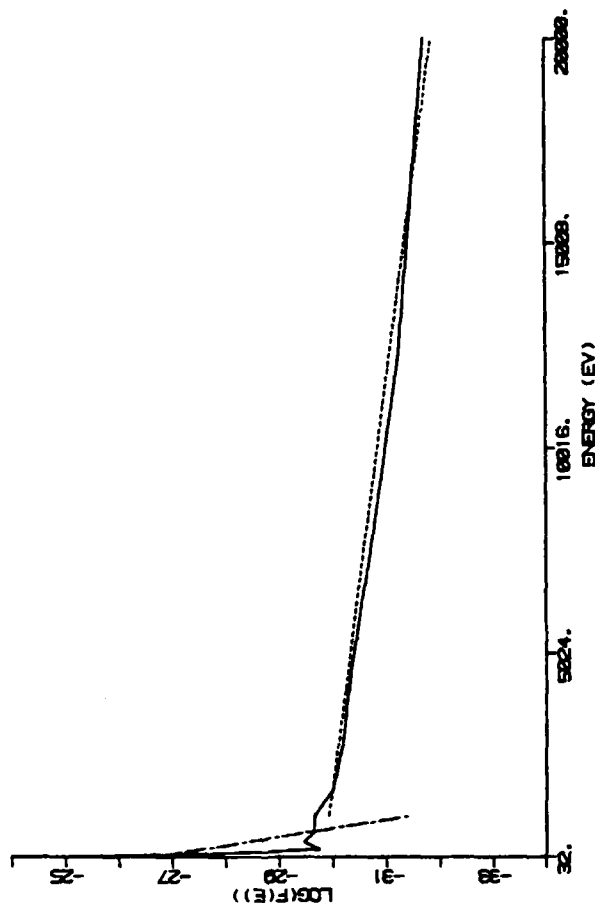
MODE = 3 1984 DAY 31
ZENITH

UT MLAT MLON OZLT
9168 86.8 97.3 8839

N = .49 T = -.4958E+88
N = 3.68 T = .1848E+87

CHANNEL	RAW COUNTS	DSPC	FSPC
1	335.0	7.83	-25.06
2	831.0	7.22	-25.08
3	1623.0	7.80	-25.44
4	167.0	6.80	-26.05
5	8.0	4.55	-26.48
6	1.0	3.44	-26.73
7	5.0	3.02	-26.46
8	6.0	3.97	-26.63
9	21.0	4.15	-26.63
10	30.0	4.83	-26.66
11	43.0	4.66	-26.08
12	67.0	4.12	-26.18
13	111.0	3.66	-26.33
14	187.0	3.06	-26.70
15	73.0	3.68	-31.22
16	51.0	3.30	-31.76

AGEV 1.20
LOG EFFX 0.68
LOG IFLX 8.68
E1= 20
E2= 1835
E3= 28608



APPENDIX B-32. Distribution Spectrum: 9168 sec U.T.
31 January 1984

B-32

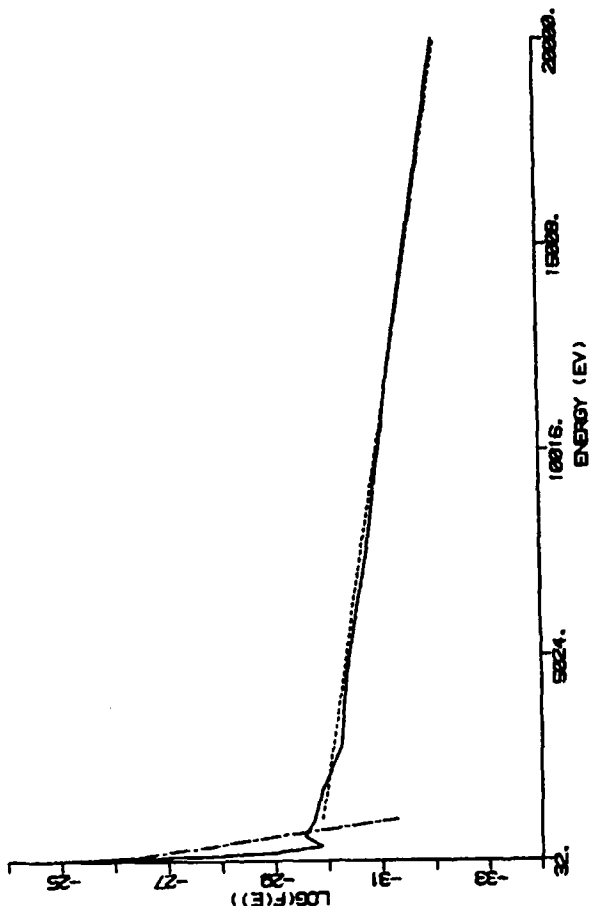
MODE = 3 1984 DAY 31
ZENITH

UT PLAT MLON OGMT
9169 66.8 97.3 8890

N = .45 T = .423E+08
N = 18.27 T = .8267E+06

CHANNEL	RAW COUNTS	DSPC	FSPC
1	755.0	7.37	-24.72
2	1897.0	7.34	-24.06
3	1897.0	7.20	-25.24
4	1420.0	7.62	-25.72
5	520.0	5.42	-27.53
6	2.0	4.74	-28.83
7	2.0	3.52	-28.82
8	11.0	4.84	-28.55
9	18.0	4.68	-28.73
10	33.0	4.68	-28.66
11	58.0	4.08	-28.33
12	58.0	4.08	-28.33
13	187.0	4.08	-28.34
14	90.0	3.85	-28.74
15	77.0	3.85	-31.10
16	21.0	3.81	-32.60

AEGY .58
LOG EFLX 0.63
LOG IFLX 0.26
E1= 20
E2= 1835
E3= 28898



APPENDIX B-33. Distribution Spectrum:9169 sec U.T.
31 January 1984

B-33

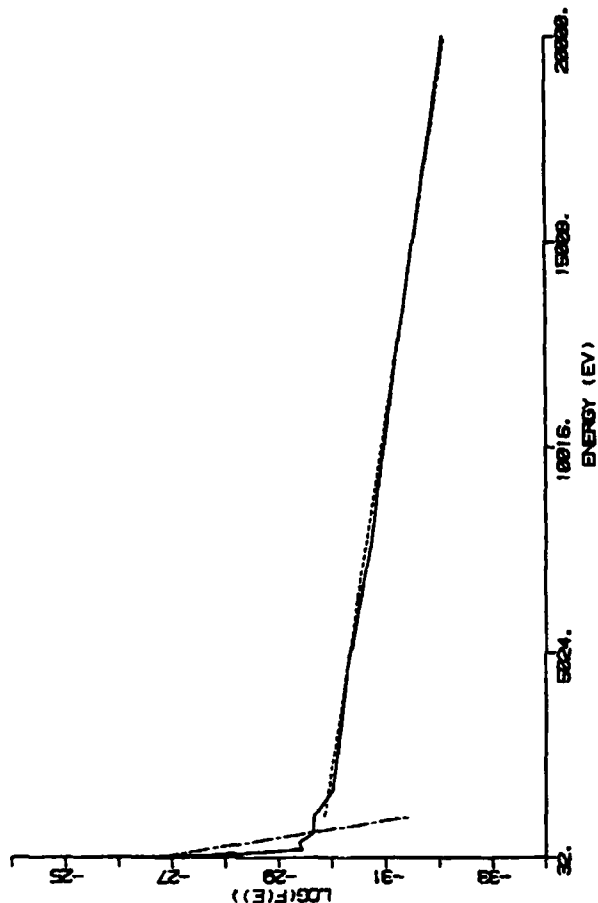
MODE = 3 1984 DAY 31
ZENITH

UT MLAT MLON OGLT
0170 66.7 97.3 0000

N = .48 T = .4245E+08
N = 2.01 T = .1055E+07

NUMBER 10 OF 68			
CHANNEL	RAW COUNTS	DSPC	FSPC
1	193.0	7.50	-24.51
2	91.0	7.26	-25.84
3	231.0	6.44	-26.80
4	12.0	4.04	-27.70
5	2.0	4.55	-28.40
6	2.0	3.74	-28.43
7	7.0	4.00	-28.50
8	18.0	3.95	-28.64
9	30.0	4.15	-28.66
10	41.0	4.01	-28.62
11	77.0	4.12	-28.12
12	123.0	4.17	-30.28
13	107.0	3.06	-30.70
14	70.0	3.70	-31.10
15	22.0	3.03	-32.07

AEGY 1.06
LOG EFLX 0.03
LOG IFLX 0.00
E1 = 20
E2 = 1035
E3 = 20000



APPENDIX B-34. Distribution Spectrum: 9170 sec U.T.
31 January 1984

B-34

MODE = 3 1984 DAY 31
ZENITH

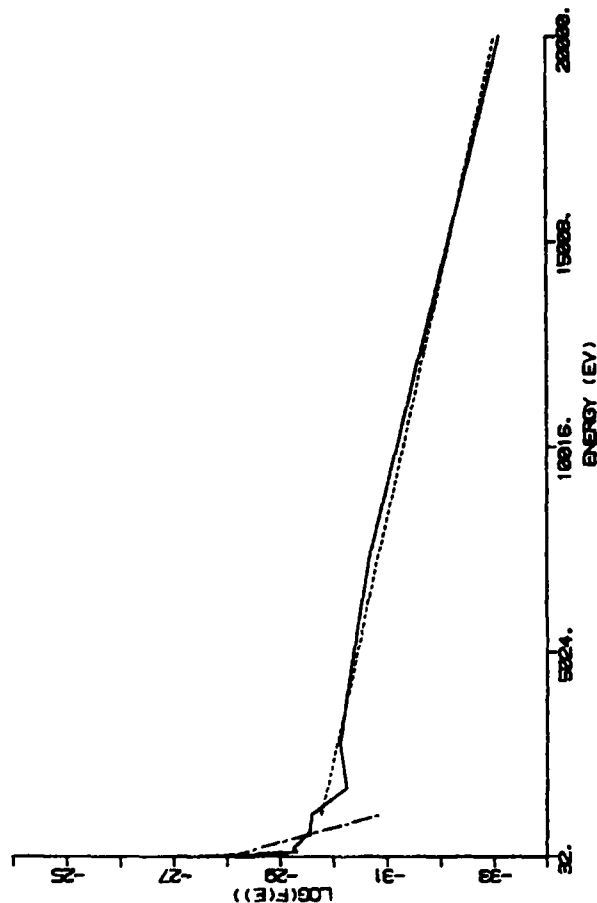
UT MLAT MLON CGLT
0170 66.7 97.3 0830

N = -38 T = .2947E+08
N = .26 T = .1804E+07

NUMBER 11 OF 68

CHANNEL	RAW COUNTS	DSPC	ESPC
1	15.0	5.28	-26.81
2	6.0	4.48	-26.82
3	2.0	4.05	-27.67
4	1.0	4.16	-28.57
5	3.0	3.65	-28.80
6	6.0	3.91	-28.25
7	9.0	4.00	-28.38
8	22.0	4.05	-28.55
9	47.0	4.23	-28.23
10	25.0	3.79	-30.23
11	77.0	4.12	-30.12
12	115.0	4.14	-30.31
13	107.0	3.95	-30.70
14	30.0	3.28	-31.60
15	2.0	1.08	-33.11
16			

AEQY 4.93
LOG EFLX 8.81
LOG IFLX 8.11
E1= 20
E2= 1035
E3= 20000



APPENDIX B-35. Distribution Spectrum: 9170 sec U.T.
31 January 1984

MODE = 3 1984 DAY 31
ZENITH

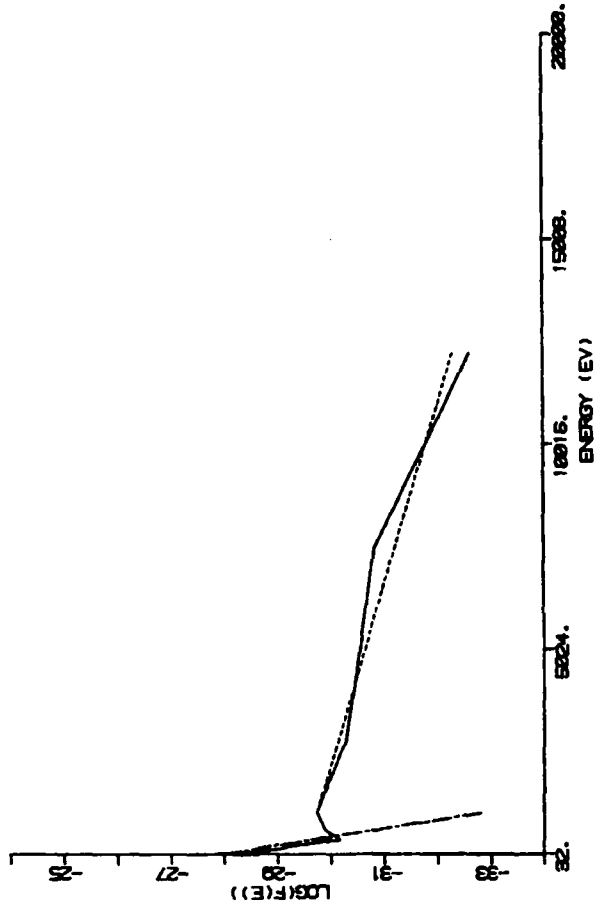
N = .31 T = .2206E+08
N = .17 T = .1020E+07

UT PLAT MLON CMLT
9172 66.6 97.3 0000

NUMBER 17 OF 60

CHANNEL	RAW COUNTS	DSPC	FSPC
1	3.0	4.00	-27.11
2	0.0	5.26	-27.04
3	2.0	4.38	-26.15
4	2.0	4.16	-26.57
5	2.0	3.05	-26.00
6	3.0	3.01	-26.25
7	1.0	3.22	-26.15
8	4.0	3.72	-26.07
9	11.0	4.00	-26.73
10	33.0	4.10	-26.03
11	51.0	3.07	-26.27
12	55.0	3.06	-26.40
13	77.0	3.05	-26.81
14	83.0	2.28	-26.80
15	3.0	0.00	-24.00
16	0.0	0.00	-24.00

AEQY 4.21
LOG EFLX 9.59
LOG IFLX 7.05
E1= 20
E2= 1035
E3= 20000



APPENDIX B-36. Distribution Spectrum:9172 sec U.T.
31 January 1984

52 10

Appendix C. Discriminant Analysis Results (42 cases)

C-1. Classification based on C413 w/o PTIME

<u>Function</u>	<u>Eigenvalue</u>	<u>After Function</u>	<u>Wilk's λ</u>	<u>Sig</u>
		0	.858	.051
1	.165	1	----	----

Standardized Discrimination Coefficients

	<u>Func1</u>
TIME	1.000

Classification Results

<u>Actual Group</u>	<u># of cases</u>	<u>Predicted</u> <u>1</u>	<u>Group</u> <u>2</u>	<u>Membership</u> <u>3</u>
Group 1	18	4 (22.2)	5 (27.8)	9 (50.0)
Group 2	20	1 (5.0)	11 (55.0)	8 (40.0)
Group 3	4	0 (0.0)	1 (25.0)	3 (75.0)

% of grouped cases correctly classified - 42.86

C-2. Classification based on CP2

<u>Function</u>	<u>Eigenvalue</u>	<u>After Function</u>	<u>Wilk's λ</u>	<u>Sig</u>
		0	.700	.035
1	.315	1	.921	.208
2	.086			

Standardized Discrimination Coefficients

	<u>Func1</u>	<u>Func2</u>
TIME	-.64768	.41345
EAVG	.14314	.89772
DT	.70203	.50386

Classification Results

<u>Actual Group</u>	<u># of cases</u>	<u>Predicted 1</u>	<u>Group 2</u>	<u>Membership 3</u>
Group 1	17	10 (58.8)	5 (29.4)	2 (11.8)
Group 2	13	4 (30.8)	8 (61.5)	1 (7.7)
Group 3	12	4 (33.3)	4 (33.3)	4 (33.3)

% of grouped cases correctly classified - 52.38

C-3. Classification based on CS1 w/o PTIME

<u>Function</u>	<u>Eigenvalue</u>	<u>After Function</u>	<u>Wilk's λ</u>	<u>Sig</u>
		0	.798	.069
1	.149	1	.916	.067
2	.091			

Standardized Discrimination Coefficients

	<u>Func1</u>	<u>Func2</u>
PEAK	1.00589	-.32728
EAVG	.63733	.84424

Classification Results

<u>Actual Group</u>	<u># of cases</u>	<u>Predicted</u> <u>1</u>	<u>Group</u> <u>2</u>	<u>Membership</u> <u>3</u>
Group 1	12	6 (50.0)	6 (50.0)	0 (0.0)
Group 2	14	3 (21.4)	9 (64.3)	2 (14.3)
Group 3	16	4 (25.0)	7 (43.8)	5 (31.3)

% of grouped cases correctly classified - 47.62

C-4. Classification based on CS1 w/PTIME

<u>Function</u>	<u>Eigenvalue</u>	<u>After Function</u>	<u>Wilk's λ</u>	<u>Sig</u>
		0	.749	.089
1	.164	1	.872	.074
2	.147			

Standardized Discrimination Coefficients

	<u>Func1</u>	<u>Func2</u>
PEAK	-.05960	1.05125
PTIME	.87464	-.28062
EAVG	-.51292	.88948

Classification Results

<u>Actual Group</u>	<u># of cases</u>	<u>Predicted</u> <u>1</u>	<u>Group</u> <u>2</u>	<u>Membership</u> <u>3</u>
Group 1	12	4 (33.3)	5 (41.7)	3 (25.0)
Group 2	14	1 (7.1)	9 (64.3)	4 (28.6)
Group 3	16	4 (25.0)	7 (43.8)	5 (31.3)

% of grouped cases correctly classified - 42.86

Appendix D. Discriminant Analysis Results
(T=1, 30-38 cases)

D-1. Classification based on C413 (32 cases)

<u>Function</u>	<u>Eigenvalue</u>	<u>After Function</u>	<u>Wilk's λ</u>	<u>Sig</u>
		0	.679	.026
1	.300	1	.883	.059
2	.133			

Standardized Discrimination Coefficients

	<u>Func1</u>	<u>Func2</u>
PEAK	-.07733	1.00745
DT	.98600	.22077

Classification Results

<u>Actual Group</u>	<u># of cases</u>	<u>Predicted Group Membership</u>		
		<u>1</u>	<u>2</u>	<u>3</u>
Group 1	8	5 (62.5)	2 (25.0)	1 (12.5)
Group 2	20	6 (30.0)	10 (50.0)	4 (20.0)
Group 3	4	2 (50.0)	0 (0.0)	2 (50.0)

% of grouped cases correctly classified - 53.13

D-2. Classification based on CPRMS (33 cases)

<u>Function</u>	<u>Eigenvalue</u>	<u>After Function</u>	<u>Wilk's λ</u>	<u>Sig</u>
		0	.775	.110
1	.165	1	.902	.082
2	.108			

Standardized Discrimination Coefficients

	<u>Func1</u>	<u>Func2</u>
TIME	-.67464	.73815
DT	.73929	.67339

Classification Results

Actual Group	# of cases	<u>Predicted Group Membership</u>		
		<u>1</u>	<u>2</u>	<u>3</u>
Group 1	10	5 (50.0)	2 (20.0)	3 (30.0)
Group 2	12	4 (33.3)	7 (58.3)	1 (8.3)
Group 3	11	3 (27.3)	4 (36.4)	4 (36.4)

% of grouped cases correctly classified - 48.48

Bibliography

- Aarons, J. "Low Angle Scintillations of Discrete Sources," Radio Astronomy and Satellite Studies of the Atmosphere, edited by Jules Aarons. 65-90. Amsterdam: North-Holland Publishing Company, 1963.
- Basu, Sunanda. Personal Interview. Air Force Geophysics Laboratory, Hanscom AFB MA, 24 July 1984.
- Basu, S. et al. "Coordinated Measurements of Low-Energy Electron Precipitation and Scintillations/TEC in the Auroral Oval," Radio Science, 18: 1151-1165 (November-December 1983).
- Briggs, B.H. and I.A. Parkin. "On the Variation of Radio Star and Satellite Scintillation with Zenith Angle," Journal of Atmospheric and Terrestrial Physics, 25: 339-366 (1963).
- Clark, R.M. et al. "Interaction of Internal Gravity Waves with the Ionospheric F2-Layer," Journal of Atmospheric and Terrestrial Physics, 33: 1567-1576 (1971).
- Cousins, M.D. et al. "The HILAT Satellite Multifrequency Radio Beacon," Johns Hopkins APL Technical Digest, 5: 109-113 (April-June 1984).
- Davies, K. Ionospheric Radio Waves. Waltham MA: Blaisdell Publishing Company, 1969.
- Elkins, T.J. and F.F. Slack. "Observations of Traveling Ionospheric Disturbances Using Stationary Satellites," Journal of Atmospheric and Terrestrial Physics, 31: 421-439 (1969).
- Farley, D.T. "A Plasma Instability Resulting in Field-Aligned Irregularities in the Ionosphere," Journal of Geophysical Research, 68: 6083-6097 (November 1963).
- Farley, D.T. "A Theory of Electrostatic Fields in the Ionosphere at Nonpolar Geomagnetic Latitudes," Journal of Geophysical Research, 65: 869-877 (March 1960).
- Farley, D.T. and B.B. Balsey. "Instabilities in the Equatorial Electrojet," Journal of Geophysical Research, 78: 227-239 (January 1973).
- Fremouw, E.J. HILAT: A Pre-launch Overview. Contract DNA 001-81-C-0189. Physical Dynamics, Incorporated, Bellevue WA, June 1983 (AD-A137-266).

- Fremouw, E.J. and L.A. Wittwer. "The HILAT Satellite Program: Introduction and Objectives," Johns Hopkins APL Technical Digest, 5: 98-103 (April-June 1984).
- Friedman, J.P. "Propagation of Internal Gravity Waves in a Thermally Stratified Atmosphere," Journal of Geophysical Research, 71: 1033-1054 (February 1966).
- Frihagen, J. "Satellite Scintillation at High Latitudes and Its Possible Relation to Precipitation of Soft Particles," Journal of Atmospheric and Terrestrial Physics, 31: 81-92 (1969).
- Goodman, J.M. "Some Evidence of Es-Layer Effects Upon 137 MHz Radio Waves," Journal of Atmospheric and Terrestrial Physics, 29: 607-612 (1967).
- Hardy, D.A. Personal Interview. Air Force Geophysics Laboratory, Hanscom AFB MA, 26 September 1984.
- Hardy, D.A. et al. "The Electron Flux J Sensor for HILAT," Johns Hopkins APL Technical Digest, 5: 125-130 (April-June 1984).
- Hardy, D.A. "The J-Sensor for the HILAT Satellite." Unpublished report. Air Force Geophysics Laboratory, Hanscom AFB MA. Undated.
- Harrower, G.A. "Theoretical Considerations in the Interpretation of Radio Star Scintillation Observations," Radio Astronomy and Satellite Studies of The Atmosphere, edited by Jules Aarons. 38-64. Amsterdam: North-Holland Publishing Company, 1963.
- Ireland, W. and G.F. Preddey. "Regular Fading of Satellite Transmissions," Journal of Atmospheric and Terrestrial Physics, 29: 137-148 (1967).
- Klecka, W.R. "Discrimination Analysis," Statistical Package for the Social Sciences (Second Edition), edited by N.H. Nie et al. 437-467. New York: McGraw-Hill Book Company, 1975.
- Liu, C.H. and K.C. Yeh. "Gradient Instabilities as Possible Causes of Irregularities in the Ionosphere," Radio Science, 1: 1283-1291 (November 1966).
- Liu, C.H. and K.C. Yeh. "Low Frequency Waves and Gradient Instabilities in the Ionosphere," The Physics of Fluids, 9: 1407-1416 (July 1966).

- Lizka, L. "Auroral Zone Satellite Scintillation Studies," Radio Astronomy and Satellite Studies of The Atmosphere, edited by Jules Aarons. 344-348. Amsterdam: North-Holland Publishing Company, 1963.
- MacKenzie, E. Personal Interview. Air Force Geophysics Laboratory, Hanscom AFB MA, 26 September 1984.
- Mass, J. "Survey of Satellite Techniques for Studying Propagation," Radio Astronomy and Satellite Studies of The Atmosphere, edited by Jules Aarons. 256-287. Amsterdam: North-Holland Publishing Company, 1963.
- McNichols, C.W. Course notes on applied multivariate data analysis. School of Engineering, Air Force Institute of Technology (AU), Wright-Patterson AFB OH, 1980.
- Potemra, T.A. et al. "The HILAT Magnetic Field Experiment," Johns Hopkins APL Technical Digest, 5: 120-124 (April-June 1984).
- Potocki, K.A. "The HILAT Spacecraft," Johns Hopkins APL Technical Digest, 5: 104-108 (April-June 1984).
- Reid, G.C. "The Formation of Small-Scale Irregularities in the Ionosphere," Journal of Geophysical Research, 73: 1627-1640 (March 1968).
- Rino, C.L. et al. "Recent Studies of the Structure and Morphology of Auroral Zone F Region Irregularities," Radio Science, 18: 1167-1180 (November-December 1983).
- Stevens, R.K. A Review of Satellite Signal Scintillations-Observations and Research. Contract DNA 001-73-C-0183. ESL Incorporated, Sunnyvale CA, November 1973 (AD-530416).
- Sudan, R.N. et al. "Generation of Small-Scale Irregularities in the Equatorial Electrojet," Journal of Geophysical Research, 78: 240-248 (January 1973).
- Yeh, K.C. "Traveling Ionospheric Disturbances as a Diagnostic Tool for Thermospheric Dynamics," Journal of Geophysical Research, 77: 709-719 (February 1972).

VITA

William E. Ober was born in Pittsburgh, Pennsylvania, on 1 February 1956. He graduated from Baldwin High School in Pittsburgh in 1974. In April of 1978, he graduated from the University of Pittsburgh with a B.S. in Physics and was commissioned in the U.S. Air Force through the ROTC program. After entering active duty, he completed Space Systems training. Subsequently, he was assigned to the NORAD Space Computational Center at Cheyenne Mountain, Colorado, where he served as a crew orbital analyst and as the Assistant Chief of Deep Space Operations. From 1982 to 1983, he completed a tour of duty at Clear AFS, Alaska, where he served as a BMEWS crew Senior Director. He entered the Air Force Institute of Technology in May 1983, and completed the Master of Science in Space Operations in December 1984. His next assignment will be at the Manned Spaceflight Support Group, Johnson Space Center, Houston, Texas.

Permanent Address: 408 Sabbath Dr
Pittsburgh, Pennsylvania
15236

END

FILMED

3-86

DTIC